Towards precision measurement with trapped hydrogen atoms

Joseph P. Scott

A thesis presented for the degree of

Doctor of Philosophy

Quantum Light and Matter

Department of Physics

The University of Durham

United Kingdom

5th June 2024

Towards precision measurement with trapped hydrogen atoms

Joseph P. Scott

Abstract

The hydrogen atom (H) is the most theoretically well-understood atomic system of all; boasting analytic solutions to both the Schrödinger and Dirac equations, and calculable QED corrections. As such, precision spectroscopy of H promises to be an excellent probe of fundamental physics, particularly for low-energy tests of QED and fifth force searches. Currently, the H spectral data-set is plagued by internal tension, expressed in the proton charge radius puzzle. There is significant evidence to suggest that this tension is at least partly a result of systematic differences between measurements. Optical trapping has led to significant advances in measurements of other atoms, particularly with the development of optical lattice clocks, where systematics related to atomic motion are tightly controlled. This thesis is concerned with the potential application of optical trapping to precision H spectroscopy towards a resolution of the proton charge radius puzzle. In service of this, it considers the effects of an off-resonant field upon a spectroscopic measurement — taking a potential 1S–2S lattice clock as an example — and whether the proven route to BEC can lead to a Mott insulator (MI) of H that is suitable for spectroscopy. This thesis describes new software for calculating atomic polarisability and atom-photon scattering rates of H S-states; reports new limits on the operation of a H lattice clock, dominated by multi-photon ionisation of the 2S state; and, for the first time, derives the conditions for producing a unitary filling MI of H.

Supervisors: Dr. David Carty and Prof. Matthew P. A. Jones

ACKNOWLEDGEMENTS

First and foremost, I want to thank my supervisors, David Carty and Matt Jones. Without them, I would have been lost, stumbling around in the fog. Their patient and insightful guidance was instrumental in all aspects of the work presented here and in my development as a physicist. In this vein, special thanks must go to Robert Potvliege, who took on many of the roles of a supervisor and guided me through the mire of atom-photon scattering. This thesis is substantially better due to their assistance.

I am so grateful to Rodney and Frances Stubbs for their patronage through the Stubbs scholarship and without whom, this work could not have been done. It was an absolute pleasure to meet them in person on their visits to the department. I hope that they are pleased with the results that they made possible.

I was lucky enough to profit from discussions with Thomas Udem, Dylan Yost, Simon Gardiner, Tobias Franzen, and Marin Bauer. All of these shaped my understanding or challenged my thinking in some way or another, and the work is a reflection of their input. I would particularly like to thank Thomas Udem for his careful and enthusiastic review of our paper when it was released in pre-print. Further, I thank my review team: C. Stuart Adams and Simon Cornish, who kept my eyes on the bigger picture and my feet on straight paths.

It takes more than just academic support to get through a PhD. To this end, I was very lucky to have studied within the Quantum Light and Matter group at Durham University. To list them all by name would double the size of this section, so I will content myself with a few special mentions: Jack Briscoe, Luke Fernley, Matthew Hill, Puya Mirkarimi, and Dan Ruttley. I also wish to thank my family: my Mum, Dad, and two sisters, Jess and Floss; who are a greater comfort to me than I would admit out loud. As well as my dear friends: Andrew, Matthew, Tobi, and Maddie; who, despite their best efforts, have upheld my spirit through the toughest times.

It would be deeply wrong of me to conclude without a mention of my wonderful fiancée Megan; who has supported me without condition or reservation since well before I began this work. As a testament to her love, she happily put aside a lifetime's aversion to physics just to know more about what I was working on. Megan, allwn i ddim fod wedi ei wneud hebddoch chi. Dw i'n dy garu di gymaint.

CONTENTS

DECLARATION

The work in this thesis is based on research carried out at the Department of Physics, University of Durham, England. No part of this thesis has been submitted elsewhere for any other degree or qualification, and it is the sole work of the author unless referenced to the contrary in the text. No AI tools have been used to generate any part of the content presented in this thesis.

Some of the work presented in this thesis has been published in journals and conference proceedings - the relevant publications are listed below.

Publications

(a.) J. P. Scott, R. M. Potvliege, D. Carty, and M. P. A. Jones, *Trap induced broadening in a potential hydrogen lattice clock*, Metrologia **61**, 025001, (2024) [1].
(b.) J. P. Scott, D. Carty, and M. P. A. Jones, *Software for calculating trap induced broadening in potential hydrogen lattice clocks*, submitted to Journal of Open Research Software (2024).
The software used in **(a.)** and described in **(b.)** is freely available at [2].

LIST OF FIGURES

LIST OF TABLES

NOMENCLATURE

Mathematical notation

$L_a^b(x)$ — Associated Laguerre polynomial, given in the Rodriguez representation [3]:

$$L_a^b(x) = \sum_{m=0}^{a} (-1)^m \binom{a+c}{a-m} \frac{x^m}{m!}. \tag{1}$$

$Y_{a,b}(\theta, \phi)$ — Spherical harmonics. As is usual in atomic physics, I follow the Condon and Shortley phase convention, specifically:

$$Y_{1,\pm1}(\theta,\phi) = \mp\sqrt{\frac{3}{8\pi}} \sin\theta e^{\pm i\phi}, \text{ and } Y_{1,0}(\theta,\phi) = \sqrt{\frac{3}{4\pi}} \cos\theta. \tag{2}$$

Unit vectors are denoted with a "hat" and quantum mechanical operators in Fraktur script: e.g. $\hat{\boldsymbol{g}}$ is a unit vector, while $\mathfrak{g}$ would be a vector operator.

Units

There are two main system of units which will be relevant for this thesis:

The S.I. system of units. Most reported values in this document are given in S.I. units [4] (with the notable exception of atomic polarisability) and are always reported with the appropriate unit labelled.

Atomic units It is often convenient to work within a system of units which are natural atomic scales. Throughout this thesis, I make significant use of the atomic units system (see [5, 6]): particularly in chapters 2, 3 and the start of chapter 4, where it is used for all mathematical expressions unless otherwise stated. It should be noted that these units result in the suppression of factors of $\hbar$, e, and m_e as well as giving the relations $\alpha_{\mathrm{FS}} \times c = 1$ and $4\pi\epsilon_0 = 1$. The energy scale is given by the Hartree, E_{h}.

Abbreviations

BEC Bose Einstein Condensate

CW continuous wave

D deuterium

EDA electric dipole approximation

FWHM full width half maximum

H hydrogen

$\bar{\mathbf{H}}$ anti-hydrogen

MI Mott insulator

OBEs optical Bloch equations

OLC optical lattice clock

QCD quantum chromodynamics

QED quantum electrodynamics

Rb rubidium

RWA rotating wave approximation

SF super fluid

SM Standard model

SOD second order Doppler

Sr strontium

SSTPE singly stimulated two photon emission

T tritium

Chapter 1

INTRODUCTION

The theoretical structure of hydrogen (H) is the most well understood of any atom [7,8]. As a two-body system, it permits exact treatment in both non-relativistic and relativistic quantum mechanics with analytic solutions of the Schrödinger [9] and Dirac [10] equations, respectively. Furthermore, corrections from quantum electrodynamics (QED) are calculable to arbitrary order. As such, the Standard model (SM) structure of H can be expressed in a single (mostly analytic) function of the quantum numbers, dimensionless fundamental constants (such as the fine structure constant $\alpha_{\rm FS}$ etc.), and two parameters: the proton charge radius $r_{\rm p}$ and the Rydberg constant R_∞ [8, 11–13]:

$$E_{n,l,j,F} = f_{n,l,j,F}(r_{\rm p}, R_\infty, \alpha_{\rm FS}...). \tag{1.1}$$

The advent of high precision laser spectroscopy has allowed this structure to be probed to finer resolutions than ever before [14,15]; enabling spectroscopic tests of bound state QED [16,17] and the possible observation of low energy SM effects such as the Neutrino force [18,19]. The 1S–2S transition has famously been measured with a fractional uncertainty of just 4.2×10^{-15} [20], and the complete H data-set includes a number of gross state frequency intervals that have been measured to experimental uncertainties $< 10\,$kHz [21–34]. This high-precision spectral data-set is an essential component in the the CODATA recommendations of both $r_{\rm p}$ and R_∞ [11–13].

As it stands, the current H spectral data-set is in serious tension, both internally [13, 34] and with the results of muonic H [35] spectroscopy and electron scattering experiments [36]. This is often discussed in terms of the so-called "proton charge radius puzzle" [37], but it equally concerns an inconsistency in the value of the Rydberg constant. There is mounting evidence to suggest that this tension may relate, at least in part, to the effects of physics beyond the SM [38–40]. An important class of new physics theories permit the (effective) exchange of hidden sector Bosons between the electron and the proton: so-called "fifth-force" theories [41]. The resultant energy shifts can be observed in precision spectroscopy, allowing for powerful bounds of the fifth-force parameter space [17,18,38–40,42–44]. Recent global fits of the spectral

data-set demonstrate that internal tension can be eased, but not completely resolved, by the introduction of such fifth forces [33, 39].

New physics theories cannot account for the disagreement between measurements of the same frequency interval. The most prominent example of this is the disagreement between two recent measurements of the 1S–3S transition [30, 32]. These discrepancies must be a result of unidentified and uncontrolled systematic differences between experiments. Modern H spectroscopy experiments use cryogenic atomic beams, where systematic uncertainty is dominated by the effects of atomic motion (e.g. the second order Doppler (SOD) shift) and complex line-shape analysis is always needed to extract the transition frequency (see, e.g. supplementary information of [33]). It is unclear how pervasive such systematic differences are in the data-set and how much they contribute to the proton charge radius puzzle.

In recent years, frequency measurements in heavier atoms have been revolutionised by the use of ultra-cold, optically trapped samples. At the epicentre of this revolution is the optical lattice clock (OLC) [45–49], which can now operate with precision surpassing that inherent in the definition of the SI section [50]. Here, atoms are tightly confined in magic wavelength optical lattices, and motional effects are resolved into independent side-band signals [45]. Mimicking this controlled atomic motion in H is essential for identifying systematic contributions to the proton charge radius puzzle and paving the way to more useful bounds on new physics.

An OLC has already been proposed for improved 1S–2S spectroscopy in anti-hydrogen ($\bar{\mathrm{H}}$) [51], which is currently conducted in a large, flat-bottomed magnetic trap with low anti-atom numbers [52, 53]. Direct comparison between the spectra of H and $\bar{\mathrm{H}}$ offers a powerful test of CPT symmetry [52–55], but would benefit from measurements in the common environment provided by optical trapping[1]. An optical lattice (or optical tweezer array) is particularly advantageous for measuring frequency intervals that involve high-lying Rydberg states, as it provides tight control over dipole-dipole interaction systematics. Such intervals offer a measurement of the Rydberg constant that is effectively free from the proton charge radius [27, 34], and are critical to spectroscopic fifth force searches [38].

In this thesis, I consider the potential use of optical trapping for improved spectroscopy of

[1]The interaction of anti-atoms with light are the same as those of atoms with light. Further, it is mostly isotope independent.

H. In service of this, I follow two distinct (yet connected) strands of investigation. The first concerns the suitability of an optical potential as an environment for precision spectroscopy. I study atomic recoil in a tightly confining optical potential, and combine it with numerical calculations of the 2S trap lifetime to assess the broadening inherent in optical trapping. The results of this strand include three new magic wavelengths for the 1S–2S transition; new bounds on the achievable line-width in a potential $H/\bar{H}$ lattice clock; and a discussion on the control of motional systematics. These results are reported in publication **(a.)**, on which some of chapter 3 and much of chapter 4 are based. This strand also involved the production of new software for calculating polarisability and atom-scattering rates in S-state H. This software is described in **(b.)** and is publicly available [2].

The second strand is concerned with methods of cooling and trapping H to produce a sample for measurement. Optical trapping of H is a major outstanding problem, and, at time of writing, has never been reported. Over the past 20 years, a variety of methods for cooling/trapping H have been proposed. Most are ultimately limited by a lack of laser power, the slow re-pump rate of the 1S–2S transition, or similar effects. However, there are a few that show significant promise, such as the threshold dissociation of laser cool-able H diatomics [56]. I focus my attention on the experimentally proven cryogenic/evaporative cooling that led to a Bose Einstein Condensate (BEC) in the late 90's [57], and consider how it could be applied to filling an ultra-cold lattice. In particular, I look into the possibility of driving the super fluid (SF)–Mott insulator (MI) transition. This strand culminates in chapter 5, which reports the conditions for achieving a unitary filling MI of H for the first time, and discusses the suitability of these systems for precision spectroscopy under these conditions.

Both strands are supported by a detailed overview the spectrum of H in chapter 2, including the complete SM structure of H and discussion of the current spectral data-set. Three appendices (A, B, and C) to this work contain additional analytic detail and tables of data. I conclude this thesis with a discussion of these results and an outlook on the future of optically trapped H in chapter 6.

Chapter 2

THE SPECTRUM OF ATOMIC HYDROGEN

It is an elementary result of quantum mechanics, that electrons occupy discrete energy states within the atom. These energy states E relate to stationary eigenstates Ψ of the atomic Hamiltonian $\mathfrak{H}_0$ and solve the time independent Schrödinger equation, $\mathfrak{H}_0\Psi = E\Psi$. It is equally well known that induced (and spontaneous) transitions between these states produce a spectra with clear absorption/emission lines at frequencies defined by the states' energy interval. Early observations of the Balmer series in H were foundational to the early development of quantum mechanics and atomic theory. Now, the advent of precision laser spectroscopy [15] allows us to probe deeper into the structure of the atom than ever before. The spectrum of H is unique amongst all atomic species due to its well-studied theoretical structure and the availability of analytic solutions.

2.1 Briefly: Spectral lines

The theory of spectral lines is very well established and does not bear unnecessary repetition. However, a general overview of the mechanisms that produce these lines and their shapes will be highly useful in later discussion (particularly chapters 3 and 4). For a full accounting of spectral lines, one should look to authoritative sources on atom-light interactions in the semi-classical [9, 58] and fully quantised [58, 59] regimes.

Consider the interaction of an atom with a monochromatic radiation field of angular frequency ω. Working in the electric dipole approximation (EDA), which assumes that the spatial variation of field strength across the atom is negligible, one obtains the interaction Hamiltonian:

$$\mathfrak{H}_{\text{int}}(t) = \boldsymbol{\mathcal{E}}(t) \cdot \mathfrak{r} = \boldsymbol{\varepsilon} \cdot \mathfrak{r}\mathcal{E}_0 e^{i\omega t} + c.c. \tag{2.1}$$

Where, $\mathfrak{r}$ is the position operator (equivalent to the electric dipole operator in atomic units), $\mathcal{E}_0$ is the electric field amplitude, and $\boldsymbol{\varepsilon}$ is the polarisation vector. Limit consideration to

only two atomic eigenstates: a and b, where $E_b > E_a$ and b spontaneously decays to a with rate Γ. In the near resonance case — when the *detuning* $\Delta = E_b - E_a - \omega$ is small — one can apply the rotating wave approximation (RWA). This approximation neglects the rapidly oscillating counter-rotating terms ($\sim e^{i(E_b - E_a + \omega)t}$) in favour of the slowly varying co-rotating terms ($\sim e^{i\Delta t}$).

The time evolution of this system is well described in the density matrix formulation of quantum mechanics by the optical Bloch equations (OBEs) [9,58]. Consider initial populations in a and b of $\rho_{aa}(0) = 1$ and $\rho_{bb}(0) = 0$. Over short times, one regains the famous *Rabi oscillations*, where population oscillates between a and b at the Rabi frequency [9,58],

$$\Omega = \mathcal{E}_0 \boldsymbol{\varepsilon} \cdot \mathfrak{r}_{ba} = \mathcal{E}_0 \boldsymbol{\varepsilon} \cdot \int d\boldsymbol{r}^3 \Psi_a^* \mathfrak{r} \Psi_b, \tag{2.2}$$

where the dipole matrix element $\mathfrak{r}_{ba}$ is implicitly defined. These oscillations are damped by spontaneous decay and the system settles into steady state solutions over timescales longer than the characteristic lifetime of the decay, $1/\Gamma$. The steady state population of state b is given [9],

$$\rho_{bb} = \frac{\Omega^2/4}{\Delta^2 + \Omega^2/2 + \Gamma^2/4}. \tag{2.3}$$

This population has a Lorentzian profile in angular frequency space, centred on the resonance condition at $\Delta = 0$ and with full width half maximum (FWHM) $\Delta\omega_{\mathrm{FWHM}} = \sqrt{2\Omega^2 + \Gamma^2}$, see figure 2.1. The rate of absorption at a given detuning is related to this steady state population [9] and absorption lines inherit the same Lorentzian profile in a space of angular frequency[1] [9,58].

At its core, this line-shape is fundamental result of how a damped oscillator absorbs from a space of angular frequency (see [9] or [58] for an alternative derivation in terms of the absorption coefficient/linear susceptibility via analogy to a classical oscillator.). The natural lifetime of the transition sets an ultimate limit on the FWHM of the line: $\Delta\nu_{\mathrm{FWHM}} \geq \Gamma/2\pi$ (most spectroscopic measurements are reported for the space of frequency ν rather than angular frequency ω).

[1] Note that the theory for emission lines is more complicated than this, see [58].

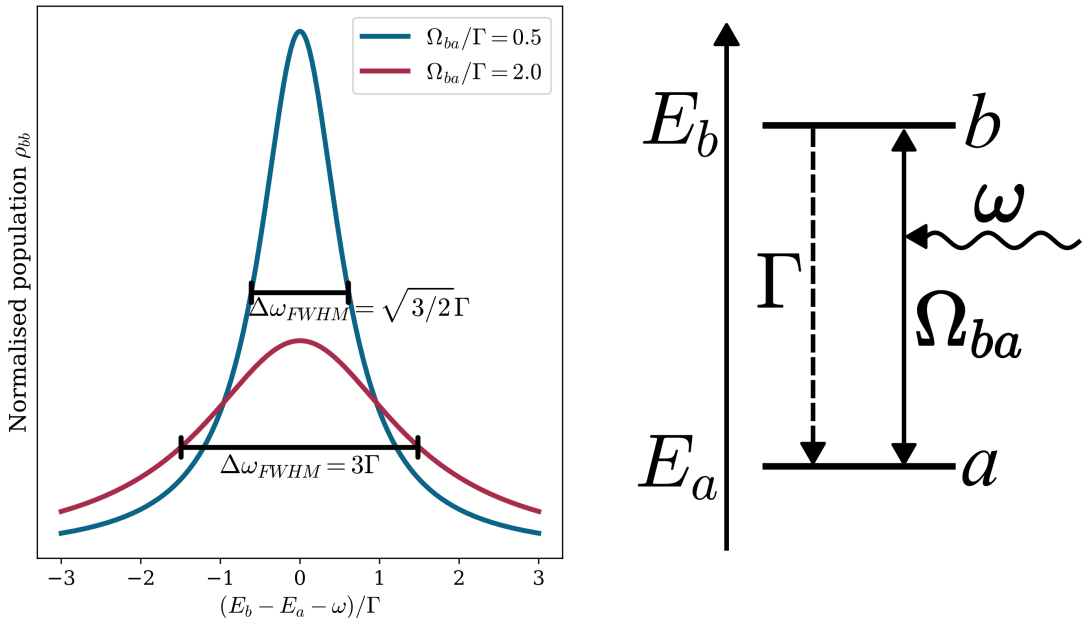

Figure 2.1: Schematic plot showing the Lorentzian profile of ρ_{bb} across the detuning (in units of the spontaneous decay rate Γ). Two lines are shown: the blue line for when $\Omega = \Gamma/2$ and the red line for $\Omega = 2\Gamma$. Each line is labelled with its FWHM. Also shown is a simple energy level diagram for the transition between a and b which shows what the physical origin of each listed variable.

2.2 Structure of atomic hydrogen

The spectrum of H reveals its internal structure, and understanding this internal structure is essential to interpreting the spectrum. Luckily, the electronic structure of the H atom is very well understood theoretically — better than any other element. The key to this theoretical success is the simplicity of the system, which allows for analytic solutions of the Schrödinger and Dirac equations. Whilst the non-relativistic structure is reviewed in any undergraduate text on Quantum Mechanics, the true power of the H lies in a well developed SM theory. The more detailed theory does not displace the old however, and critical context is contained within the Quantum Mechanical models. As such, an essential overview of the H structure follows, a full review of the known H structure can be found in the CODATA reviews (e.g. [11–13]) and in the energy level tabulations [7, 8].

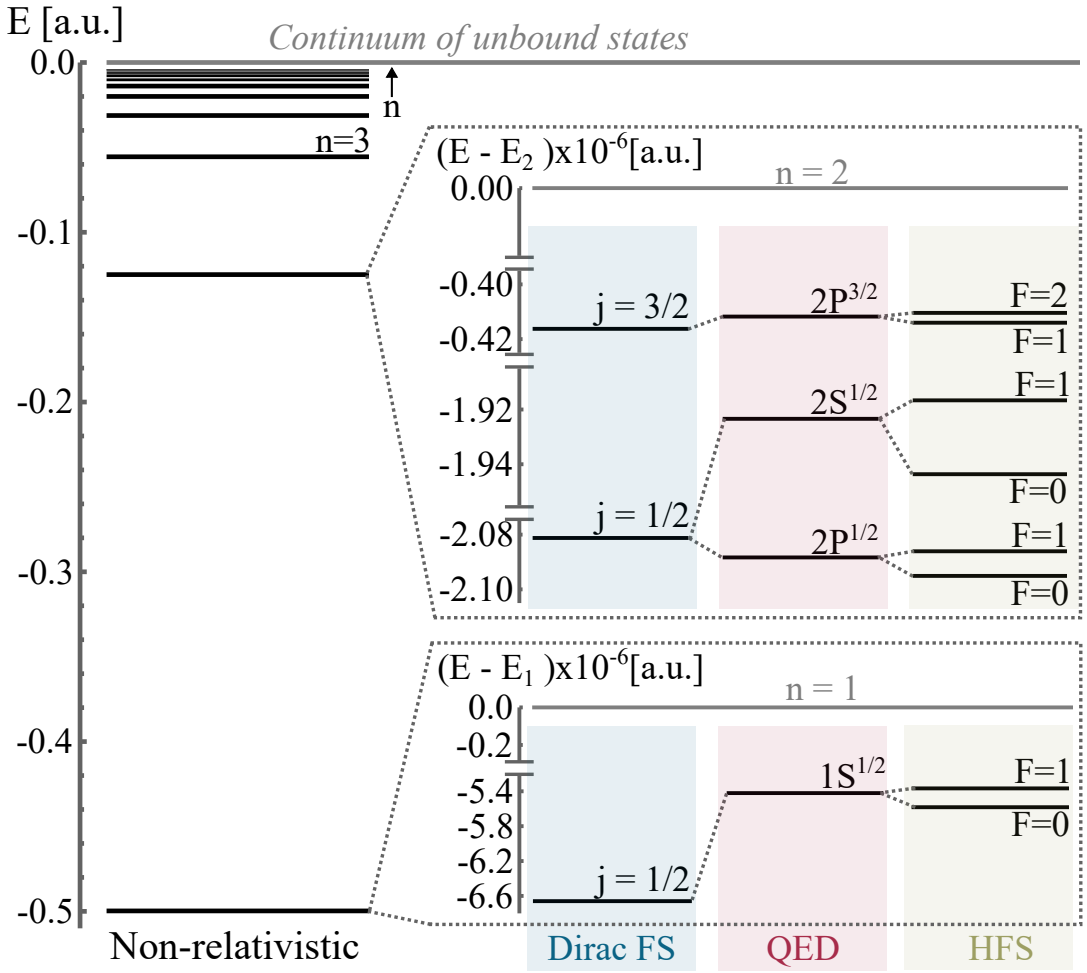

Figure 2.2: Energy level diagram showing the non-relativistic structure of atomic hydrogen (section 2.2.1). Detailed structure is shown for the $n = 1$ and 2 states including the Dirac fine structure (section 2.2.3), leading-order QED corrections (section 2.2.4), and hyperfine structure. Levels in the detailed structure were calculated to leading order in α_{FS} and agree with the tabulations of [8].

2.2.1 Non-relativistic quantum mechanics

The hydrogen atom consists of a single proton and a single electron coupled by the Coulomb interaction. The related Hamiltonian is written in spherical coordinates as [7, 9, 60],

$$\mathfrak{H}_0 = -\frac{1}{2\mu_H}\nabla^2 - \frac{1}{r} = -\frac{1}{\mu_H r^2}\frac{\partial}{\partial r}\left(r^2\frac{\partial}{\partial r}\right) - \frac{\mathfrak{l}(\theta,\phi)^2}{2\mu_H r^2} - \frac{1}{r}, \tag{2.4}$$

where,

$$\mathfrak{l}(\theta,\phi)^2 = -\left(\frac{1}{\sin\theta}\frac{\partial}{\partial\theta}\left(\sin\theta\frac{\partial}{\partial\theta}\right) + \frac{1}{\sin^2\theta}\frac{\partial^2}{\partial\phi^2}\right). \tag{2.5}$$

Stationary states can be found by solving the associated time-independent Schrödigner equation $\mathfrak{H}_0\Psi(\boldsymbol{r}) = E\Psi(\boldsymbol{r})$. It is well-known that this can be done exactly by separation into radial and

angular parts, and the calculation can be found in any good textbook on quantum mechanics or atomic physics (see e.g. [9]).

Solutions are given as the product of a purely radial function and a purely angular one: $\Psi_{nlm}(\boldsymbol{r}) = R_{nl}(r)Y_{lm}(\theta,\phi)$. Angular functions Y_{lm} are exactly the spherical harmonics, whilst radial functions are given [60],

$$R_{nl}(r) = \mathcal{N}_{nl}\frac{2\mu_{\mathrm{H}}}{n}s^l e^{-s/2}L^{2l+1}_{n-l-1}(s), \tag{2.6}$$

in terms of the associated Laguerre polynomials, with $s = 2\mu_{\mathrm{H}}r/n$ and $\mathcal{N}$ a normalising constant such that $\int_0^\infty dr R_{n'l}r^2R_{nl} = \delta_{n'n}$. These wave-functions are indexed by three quantum numbers: the principle quantum number $n \in \mathbb{N}$; the orbital angular momentum number $l \in \mathbb{N} < n$; and the magnetic number $m \in \mathbb{Z}_0$. As a projection of l onto an axis of quantisation, m is further constrained to $|m| \leq l$. Together, these three numbers completely define any unique non-relativistic H bound states.

In the absence of an external field states are degenerate in m. Further, the spherical symmetry of the system ensures a degeneracy in l. What results is a *discrete spectrum of bound states* with energy depending only upon n (see figure 2.2) [7–9]:

$$E_{nlm} = E_n = -\frac{\mu_{\mathrm{H}}}{2n^2}. \tag{2.7}$$

The reduced mass μ_{H} includes information about the nuclear mass of the hydrogen atom. The nucleus of the most common isotope of hydrogen is a single proton, and provides the reduced mass $\mu_{\mathrm{H}} = 0.99946$. The next most common isotope of hydrogen, deuterium (D)[1], has both a proton and a neutron in its nucleus. The resultant change in the reduced mass to $\mu_{\mathrm{D}} = 0.99973$ alters the energy levels compared to H,

$$E_{n,\mathrm{D}} = \frac{\mu_{\mathrm{D}}}{\mu_{\mathrm{H}}}E_n = 1.00027 \times E_n, \tag{2.8}$$

in what is called the *isotope shift*. The large relative differences between the nuclear masses of H and D (a factor of ~ 2) makes this one of the most significant isotope shifts of any atomic species.

[1]The third hydrogen isotope, tritium (T) is radioactive and highly desirable for nuclear fusion research. Therefore, its use is controlled within the United Kingdom, making it unsuited to any lab-scale spectroscopy experiment. As such, I will neglect further discussion of it in favour of more experimentally suitable isotopes.

In addition to these bound states, there is a *continuum of unbound states* which relate to free electrons moving in the Coulomb potential. The energy of these states is not quantised, but given by the kinetic energy of the free election: $E = k^2/2$ (in atomic units). As the symmetry of the system is unchanged, the angular wave-functions are still given by the spherical harmonics $Y_{l,m}(\theta, \phi)$. The free particle wave-function is modified by the central potential in the radial Coulomb functions [61]:

$$R_{k,l} = C_{kl} e^{ikr} r_1^l F_1 \left[-\frac{i}{k} + l + 1; 2l + 2; -2ikr \right], \tag{2.9}$$

where ${}_1F_1$ is a confluent hypergeometeric function and the constant $\mathcal{C}_{kl}$ is chosen such that $\int r^2 dr R_{k'l} R_{kl} = \delta_{k-k'}/k^2$. Whilst spectroscopy is generally limited to the discrete part of the spectrum (since excitation to unbound states — ionisation — is naturally destructive) the existence of the continuum has important implications for later discussion.

2.2.2 Finite nuclear size

Whilst the finite nuclear mass is already considered in section 2.2.1, it still treats the nucleus as a point particle. In reality the nucleus has a finite size, relating to some distribution of charge that shifts the atomic state energies — particularly for S-states ($l = 0$) which significantly overlap the nucleus. In the non-relativistic theory (and assuming a spherically symmetric charge distribution), this shift is given for H as [11],

$$E_{NS} = \frac{2\mu_{\mathrm{H}}^3 \alpha_{\mathrm{FS}}^2}{3n^3 \lambda\!\!\!^{-}_C} r_{\mathrm{p}}^2 \delta_{l0}, \tag{2.10}$$

where $\lambda\!\!\!^{-}_C$ is the reduced Compton wavelength of the electron and r_{p} is the root mean square of the proton charge radius. Of course, for deuterium the proton charge radius r_{p} is replaced with the charge radius of the deuteron r_{D}. Differences between the charge distributions in the proton and the deuteron only appear in higher order corrections, see [11, 62, 63].

2.2.3 Relativistic quantum mechanics

So far, the hydrogen atom has been treated in the context of non-relativistic quantum mechanics. To extend beyond this regime to relativistic quantum mechanics one must solve a Dirac

equation instead of a Schrödinger equation. This solution is also well established (see e.g. [10]) and, in the limit of infinite nuclear mass, returns bound state energies [10, 64, 65],

$$E_{\text{Dirac}} = \alpha_{\text{FS}}^{-2}\left[1+\frac{\alpha_{\text{FS}}^2}{(n-\kappa+(\sqrt{\kappa^2-\alpha_{\text{FS}}^2})^2}\right]^{-1/2} = \alpha_{\text{FS}}^{-2} - \frac{1}{2n^2} - \frac{\alpha_{\text{FS}}^2}{2n^3}\left(\frac{1}{\kappa}-\frac{3}{4n}\right) + O(\alpha_{\text{FS}}^4), \tag{2.11}$$

that are dependent upon the electron angular momentum quantum number j (the electron has spin 1/2, so j takes the values $l \pm 1/2$) as $\kappa = j + 1/2$. This j-dependence splits states with a shared n into distinguishable levels, adding an additional layer of structure to the spectrum — the "fine structure" which can be seen in figure 2.2.

The first term of 2.11 is the rest mass energy and the second term regains the non-relativistic results of equation 2.7 (in the limit of infinite nuclear mass, $\mu_{\text{H}} \to 1$). The third term contains the first order relativistic corrections to the state energies. This result can be amended for a finite nuclear mass as in [64] or [65]. This amendment is not trivial and contains a number of many-body terms that are hard to evaluate. On the simplest level, this corrects the rest mass energy to be that of the entire system $(m_{\text{N}}+1)/\alpha_{\text{FS}}^2$ (where m_{N} is the nuclear mass) and includes the reduced mass in the non-relativistic energy term.

2.2.4 The QED structure

A complete treatment of the Coulomb interaction between the electron and proton must be given in terms of QED. Unlike in the application of quantum mechanics, one does not solve a single governing equation like the Schrodinger or Dirac equations and produce the bound state energies. Instead, the picture must be built up from individual n photon processes and their contributing diagrams, building up complexity as we go. For example, the leading order QED corrections come from 2^{nd} order (one photon) processes and include both self-energy [66] and vacuum polarisability terms. Expanding these terms up to the zeroth power of α_{FS} leaves a correction to a given n, l state [11–13],

$$E^{(2)} = \frac{4\alpha_{\text{FS}}^3}{3\pi n^3}\left(\delta_{l0}\left(\ln(\alpha_{\text{FS}}^{-2}) + 10/9\right) - \frac{4}{3}\ln(k_0(n,l))\right). \tag{2.12}$$

The first term only applies to S-states and is the dominant source of the Lamb shift which breaks the l degeneracy of the $j = 1/2$ states predicted by the fine structure (as shown in figure 2.2).

The second term is much smaller and depends on the Bethe logarithms $k_0(n,l)$ [67]. QED corrections are well studied, and the full set of known corrections extends well beyond one photon processes: e.g. relativistic recoil [68] and nuclear polarisation terms [12] to name a few. There is no fundamental barrier to calculating these corrections to arbitrary order in QED; however, they rapidly become smaller whilst the complexity of calculation increases. Currently, corrections are well known up to 6^{th} order (three photon processes) [8, 13].

The energy of a given n, l, j state of H is then given by the expression [8, 29, 32],

$$E_{nlj} = -\frac{1}{2}\left(\frac{\mu_H}{n^2} + f\left(\alpha_{\text{FS}}, \frac{1}{m_{\text{p}}}, \dots\right) + E_{NS}\right). \tag{2.13}$$

Where f is a mostly analytic function that includes all of the relativistic and QED corrections to the non-relativistic structure of the first term at a desired order. f depends only on dimensionless fundamental constants (e.g. the fine structure constant and the electron-proton mass ratio) which can be measured very accurately in other experiments (see e.g. [13, 69]).

In theory, H energy levels can be calculated to any desired order from first principles, using only measured values of the dimensionless fundamental constants. This is a highly desirable trait for a frequency standard, which could be exactly related to fundamental principles rather than defined by an artefact[1] [70]. In reality, there are two parameters in equation 2.13 which cannot be set with sufficient precision by other experiments: the proton charge radius r_{p}, which cannot yet be calculated from quantum chromodynamics (QCD) [71], and the Rydberg constant[2] R_∞. Any spectroscopic measurement of H must fix a value of one of these parameters to act as a measurement of the other.

The n, l, j states are further shifted by the interaction between the total electron angular momentum j with the nuclear spin I (see e.g. [9]). States with total angular momentum $\boldsymbol{F} = \boldsymbol{j} + \boldsymbol{I}$ and are split according to the associated quantum number F into the hyperfine structure (see figure 2.2). This structure is generally inconsequential to the optical/UV spectroscopy discussed in this thesis, as these are measurements of the hyperfine centroid — which can be extracted from comparative measurements between different pairs of F states (see supplementary information of [29]).

[1] Whilst the energy levels of caesium will be ultimately dependent upon these fundamental principles, the complexity of the atom prohibits their ab-initio calculation. As such, the transition that defines the SI section is ultimately a measured quantity and the definition is necessarily defined relative to this physical artefact.

[2] This is a conversion term which connects the internal scales of the atom with the SI system of units, here it has been subsumed into the definition of atomic units.

2.2.5 Effects of new physics

While the SM theory of H is well established, its simple nature makes it possible to compute the effects of theorised extensions to the SM. A particularly interesting category of theories that go beyond the SM with clear implications for H are so-called "fifth force" theories. The connection to the four fundamental forces is clear in the name, but, while it does include theories of new gauge Bosons (such as the B-L gauge boson [72,73]), it covers any force arising from the exchange of any hidden-sector Boson(s) [74] (such as in the well motivated Higgs-portal [75] and dark photon [76] models).

Many of these theories include non-trivial coupling to both the electron and the proton. The resultant force perturbs the established QED structure of the H atom, resulting in an energy shift,

$$E_{nlj} \rightarrow E_{nlj} + \delta E_{\mathrm{NP}}, \tag{2.14}$$

that is heavily model dependent. Of particular interest is the Yukawa-type interaction which arises from a long-range treatment of various short-range interactions. This is an "effective" theory which describes the exchange of the new Boson as a single force between the nucleus and the electron and applies to a wide range of different models (see [38] for a discussion of this). Under this interaction, the shift is bounded [38],

$$|\delta E_{\mathrm{NP}}| < \frac{-2|g_e g_N| E_n}{\alpha_{\mathrm{FS}} 4\pi}, \tag{2.15}$$

where E_n is the non-relativistic energy[1] and g_e and g_N are the electron and nuclear couplings. These shifts can, in principle, be observed in high-precision spectroscopy experiments.

In H, a direct comparison between the measured frequency interval and that predicted by the QED structure (equation 2.13) is possible; resulting in a measured value of δE_{NP} which can be used to bound the new physics parameter space in the low energy regime [17,18,38–40,42–44]. For light force mediators (mass $< 1\,\mathrm{MeV}$), spectroscopic bounds are expected to be stronger than any other lab-based search, even out performing high-energy particle colliders [17,42,77]. While this part of parameter space is well constrained by astrophysical observations (e.g. see [78]), they are insensitive to so-called Chameleon fields — whose mass depends upon the local

[1] It is a bound state energy, hence the negative sign above.

energy density [79,80]. The variation of energy density across an atom is not sufficient to shield a Chameleon from detection in lab-based spectroscopy [81]. Further discussion of these shifts in the context of the current H spectral data-set is reserved for section 2.3.2

2.3 Modern hydrogen spectroscopy

2.3.1 The 1S–2S transition

The greatest success of modern H spectroscopy is the measurement of the 1S–2S transition frequency to a relative uncertainty of 4.2×10^{-15} [20]. This transition involves the simultaneous absorption or stimulated emission of two photons and can be described by a second-order perturbative expansion of $\mathfrak{H}_{\rm int}$. It can be treated as an effective first order (1-photon as in section 2.1) with Rabi frequency [58]:

$$\Omega_{ba}^{(2)} = \mathcal{E}_0 \sum_k \frac{\boldsymbol{\varepsilon}\cdot\mathfrak{r}_{bk}\boldsymbol{\varepsilon}\cdot\mathfrak{r}_{ka}}{E_k - E_a - \omega}, \tag{2.16}$$

and two-photon detuning $\Delta^{(2)} = \omega_0 - 2\omega$, which dictates the new resonance condition $\omega_0 = 2\omega$. The expression sums over all atomic states k that are dipole coupled to both a and b. The related absorption/emission lines can be shown to have the same Lorentzian shape as is seen for the first-order processes (figure 2.1) [58]. Spectroscopy of two-photon transitions is particularly powerful as it can be performed in a Doppler-free manner [9, 20].

This frequency interval was measured by two-photon spectroscopy in a cryogenic (5.8 K) atomic beam of H, where the atoms are necessarily moving. Even with the elimination of the Doppler effect, the atoms are still subject to the SOD effect[1], which shifts the incident frequency[2] according to the velocity $\boldsymbol{v}$ [20],

$$\frac{\delta\omega}{\omega} = -\frac{1}{2}|\boldsymbol{v}|^2\alpha_{\rm FS}^2. \tag{2.17}$$

This is a relativistic effect, arising from time-dilation between the stationary lab frame and the moving atom frame. Despite the slow (in comparison to the speed of light) atoms, this effect becomes a dominating source of systematic uncertainty in the 1S–2S measurement. The SOD

[1] As well as a number of residual higher-order Doppler effects that arise from wavefront curvature etc.
[2] Recalling that $c = 1/\alpha_{\rm FS}$ in atomic units.

effect introduces a velocity-dependent shift to the transition frequency that asymmetrically distorts the line-shape according to the velocity distribution. It can be mitigated somewhat by addressing only a narrow velocity class at the tail end of the velocity distribution, reducing both the total shift and the variation over all atoms. This comes at the expense of statistical power as there are fewer atoms in this slow velocity class and the uncertainty budget must balance this with the systematics related to the SOD.

In the end, the 1S–2S transition was measured with an experimental error of 10.4 Hz and an observed line-width of $\Delta\nu_{\mathrm{FWHM}} = 2\,\mathrm{kHz}$. The uncertainty budget was dominated by statistics (6.3 Hz), SOD effect (5.1 Hz) and the line-shape model (5.0 Hz). This measurement was repeated two years later by with a similar set up, but with a fibre-link directly to the Cs fountain clock at Physikalisch-Technische Bundesanstalt [28]. The experiment benefited from improved statistics (3.3 Hz) but suffered from larger SOD systematics (8.0 Hz). Ultimately, it confirmed the previous measurement, but with a slightly higher experimental error of 10.8 Hz

2.3.2 The hydrogen spectral data-set

The 1S–2S transition is central to the CODATA recommended value of the Rydberg constant [11–13]. In previous recommendations, it was combined with only a handful of frequency intervals known to experimental errors of $\leq 10\,\mathrm{kHz}$ from thermal beam measurements in the late 90's [21–26]. In the past 6 years, the H dataset has been expanded with a series of measurements at the sub 10 kHz level from cryogenic beam experiments, including: the 2S-2P [31]; 2S-4P [29]; 2S–8D [33]; and 1S–3S [30, 32] intervals. Many of which were included in the most recent CODATA recommendation [13]. It is worth noting that in the 11 years since the last measurement of the 1S–2S transition [28], no H frequency interval has been measured to a comparable precision. The only H frequency intervals known to the same 10 Hz level as the 1S–2S (apart from the 1S and 2S hyperfine intervals [82–86] which are not directly relevant to the Rydberg constant) are the intervals between circular Rydberg states of n from 27 to 30 (unpublished, [27]) which do not contribute to the CODATA recommendations. Very recently, the sub-10 kHz data set has been supplemented by new measurements of the interval from 2S to the circular Rydberg states with n=20 and n=24 [34]. The full spectral dataset often includes a number of measurements with experimental errors greater than 10 kHz [87–90].

All of these high-precision measurements come from atomic beam experiments similar to the 1S–2S setup. As such, line-shifts and broadening due to atomic motion are significant sources of experimental uncertainty [20,31,33]. As in the 1S–2S measurement, this impact can be reduced with careful velocity filtering at the expense of statistical power, and the drive towards cryogenic beams in recent years is partly fueled by the desire for improved statistics at low velocities. Regardless, these effects always result in complex line-shapes, and detailed analysis is required to extract a precise value of the transition frequency (e.g. see the supplementary information of [33]). Systematic concerns within these line-shape models are also leading contributors to the uncertainty budget. Measurements in Rydberg intervals are further limited by strong dipole-dipole interactions, scaling as n^4 for circular states [91]. These interactions were a dominating source of systematic uncertainty in the early measurements due to the ill-defined inter-atomic spacing in a thermal (80 K) beam [27]. This is accounted for in the modern experiment by a very low probability of Rydberg excitation, only 1 per each 3 runs of the experiment [34]. Of course, this also comes at the cost of statistical power.

As discussed in section 2.2.5, comparison between theory and measurement can be used to bound the fifth force parameter space. Previously, the H dataset has been used in combination with data from other sources (including H-like exotic atoms and measurements of the electron anomolous magnetic moment) to test or constrain fundamental physics [17, 42]. More recently, Jones *et. al.* used such a global fit of only H spectral data to constrain the parameters of a Yukawa type fifth force (equation 2.15), bounding $|g_e g_P| < O(10^{-11})$ for boson masses ranging from 10 eV to 1 keV [38]. These bounds can be vastly improved for theories with non-uniform coupling to the proton and deuteron by fitting over the combined H and D datasets [40]. This idea has recently been extended by Delaunay *et. al.* to simultaneously extract both SM and new physics parameters from a global fit assuming certain new physics models [39]. Their results are in broad agreement with the previous bounds when comparisons are possible.

Counter-intuitively, these global fits turn out to be dependent upon the exact composition of the data-set used [38–40]. In particular, bounds are highly sensitive to the inclusion or exclusion of the Rydberg intervals [38], and a direct comparison of the 1S–2S transition in H and D is more tightly constraining than global comparison [40]. This is a result of serious tension in the H (and D) spectral dataset — known as the *proton charge radius puzzle*.

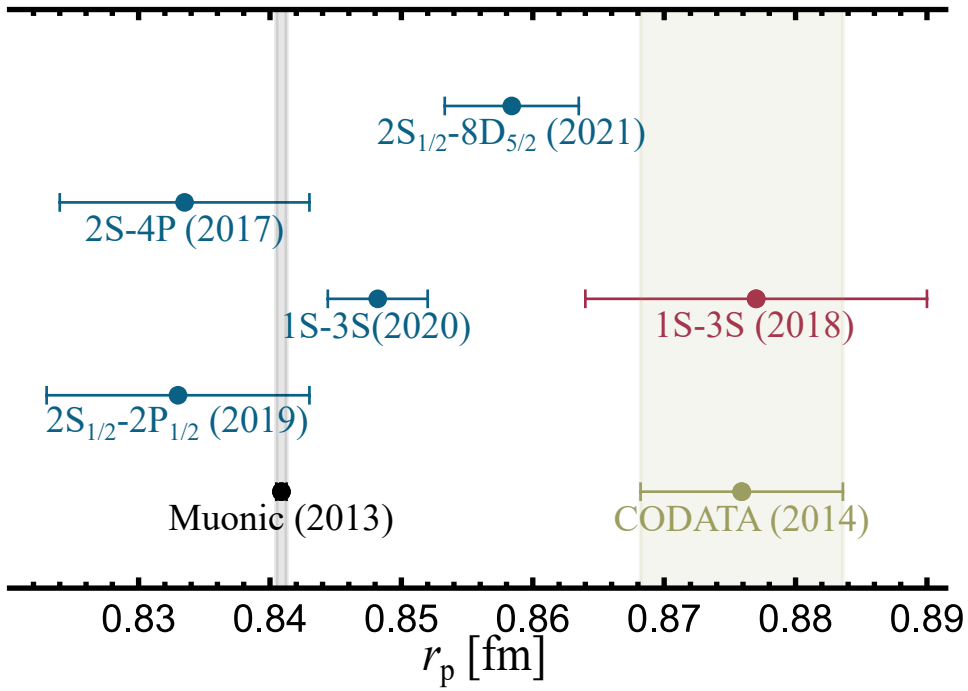

Figure 2.3: Values of the root mean square proton charge radius extracted from H spectroscopy. H measurements from before 2014 are incorporated into the CODATA recommended value of r_p [12]. H measurements since then are individually labelled and are colour coded: blue for measurements in cryogenic beams [29, 31–33], red for measurements in thermal beams [30]. Also included is the value extracted from a measurements in muonic H [35] in black.

2.3.3 The proton charge radius puzzle

In section 2.2.4, I stated that the energy levels of H depend upon both R_∞ and r_p which act as free parameters and must be measured spectroscopically. A value of either parameter can be extracted from a spectroscopic measurement by "fixing" the other with another, known transition frequency. As the 1S–2S transition is known to the highest precision, it is usually chosen to fix a value of R_∞ and extract measurements of r_p from other measured frequency intervals. Unfortunately, the complete set of r_p extracted in this way is **inconsistent**; both internally [12, 13, 34, 37] and with the results of muonic H [35] (see figure 2.3). This is the famous *proton charge radius puzzle*[1] [37] and points to deeper disagreement in the H spectral world-dataset that affect the new physics bounds discussed above. The recent CODATA recommendation [13] of both r_p and R_∞ favours the muonic values over the previous values [12], but it does not alleviate the tension in the H dataset.

[1]This could equally be constructed in terms of a *Rydberg constant puzzle*, as r_P and R_∞ are correlated to 98.9% [92].

Measurements of the intervals between Rydberg states should offer a value of R_∞ that is effectively free of r_p, but even these measurements are in tension. Early measurements of the intervals between circular Rydberg states of n=27 to 30 by De Vries produced a value of R_∞ that was consistent with almost the entire existing spectral data-set [27,34,91] (partly due to a relatively large final error). The Rydberg constant obtained by the more recent measurements of Scheidegger and Merkt, however, does not conform with either the 2014 or the 2018 CODATA recommendations of the Rydberg constant [34]. Not only is it in tension with most of the H spectral data, but it has only a very narrow overlap with the results of De Vries [34].

The source of this puzzle is still an open question, but there are two lines of thought:

1. **New physics shifts**: This inconsistency could be the result of some state dependent new physics shift, like those described in section 2.2.5. It has been noted that the introduction of a long-range Yukawa-type potential goes some way to relieving this tension [33]. This view is bolstered by a recent work that uses a global fit to simultaneously extract both the fundamental physical constants and new physics parameters from the H spectral dataset [39]. It showed that this tension can be alleviated by contributions from a light scalar boson with non-universal coupling. Whilst these are promising results, neither shows a complete resolution of the proton charge radius problems, only reducing the inconsistency. Recent results of Rydberg spectroscopy *may* support an n dependent effect, but the effect of incorporating them into the full H-dataset is not yet clear.

2. **Systematic error**: As discussed in section 2.3.1, beam measurements rely on complex line-shape analysis to extract the transition frequency. It is feasible that this inconsistency is due to unknown systematic considerations that vary between experiments. This view is strengthened by observations about the nature of the H spectral world data and comparisons between “hot” and “cold” measurements. The 2014 CODATA value was constructed from measurements in thermal atomic beams [12], whereas, more modern measurements with cryogenic beams tend to align with results of muonic H (see figure 2.3). This difference is a first indication of a velocity dependent systematic that has not been accounted for. Further support can be found in the disagreement between two recent measurements of the 1S–3S transition [30] and [32], which must be explained in

terms of experimental differences[1] — unless the H atoms in France are different to those in Germany.

Overall, it is still unclear how much, if any, of the proton charge radius puzzle can be put down to the effects of new physics. Regardless, new physics shifts cannot completely resolve this puzzle or adequately explain the disagreement between measurements of the same transition. It is clear that there is at least some contribution from systematic variation between experiments. These systematics must be identified as a matter of urgency.

2.4 Towards new experiments

It is clear that H spectroscopy is in need of an experimental step-change. The beam measurements that have dominated the field for almost 30 years are approaching a fundamental limit to their precision, enforced by the competing effects of atomic motion and statistical pressure. Not only this, but there is strong evidence of unknown systematic errors — likely related to atomic motion in some way — that tension the spectral dataset. This tension is complicated by possible contributions of new physics; since the new physics parameter space is so large (and there is no shortage of potential models) it is impossible to tell how much each effect contributes to the proton charge radius puzzle. Further, almost all spectroscopic values of r_{p} rely on the Parthey *et. al.* measurement of the 1S–2S transition to set the Rydberg constant. This value is also used to extract Scheidegger and Merkts' measurement of the Rydberg constant [34]. As a community, we are in the position where all these measurements depend upon effectively a single measurement of the 1S–2S transition frequency. Even the other 1S–2S measurements that appear in the H spectral dataset [28, 89], were performed with essentially the same experimental set-up by many of the same people. This makes the entire H dataset vulnerable to potential systematic uncertainties in the 1S–2S measurement. A new form of experiment, with a completely different set of systematic errors is essential to resolving this and proceeding with new physics searches.

[1] Whilst it is clear that there is a discrepancy, it is worth noting that there is no reason to favour the cryogenic measurement over the thermal measurement. Neither group has been able to point out the error in the others experiment.

In the same time period, the precision spectroscopy of heavier atoms has been completely revolutionised by the application of *optical trapping* and ultra-cold samples [93]. The greatest success of this has been in OLCs [45–49], which operate at precisions of $\sim 10^{-18}$, surpassing that of the SI second [50]. The evolution of atomic clocks from fountain clocks to OLCs is a clear, motivating analogy for the evolution of precision H spectroscopy: from atomic beams to optical trap[1]. Beyond long interrogation times and the improved precision implied by this analogy, there are a number of clear advantages to H spectroscopy in a tightly confining optical lattice or tweezer array:

- **New dominating systematics**: The effects of atomic motion can be effectively eliminated in an optical lattice/tweezer array by operating in the tight-confining or "Lamb-Dicke" regime [45]. The uncertainty is instead dominated by statistics, and systematics related the long term beam stability and off-resonant atom-photon interactions.
- **Well defined inter-atomic spacing**: When occupation is restricted to one atom per lattice site/tweezer, the inter-atomic spacing is well defined (even controllable in a tweezer array) and stable. This enables control over systematics related to dipole-dipole interactions without sacrificing excitation probabilities and greatly benefits potential Rydberg spectroscopy.
- **Isotope-independent interactions**: The interactions of H with an optical field is necessarily isotope independent (up to small variations due to mass difference). As such, these optical traps are ideal the comparative measurements between H and D that are key to improved bounds on fifth force theories with non-universal coupling [40]. For similar reasons, the system is also ideal for direct tests of CPT symmetry through the comparison of H and $\bar{\text{H}}$ [52–55]. An $\bar{\text{H}}$ lattice clock, operating on the 1S–2S transition has already been proposed [51].

At the time of writing, optically trapped H *has never been realised* — not in a lattice, or tweezers, or any sort of optical dipole trap. The natural first step is to consider the properties of optically trapped H.

[1] An OLC of $\bar{\text{H}}$ has already been proposed as a route to improved spectroscopy of the 1S–2S transition [51].

Chapter 3

HYDROGEN IN OFF-RESONANT OPTICAL FIELDS

In section 2.1, I outlined how dipole allowed transitions between atomic states can be driven by optical fields close to resonance. This was further extended in section 2.3.1 to second-order transitions at two-photon resonances. It is now time to drop the resonant condition all-together and consider the effects of off-resonant fields upon atoms in *bound* atomic states. Such processes are foundational to the optical trapping posited in section 2.4. The following discussion draws from work that has been previously published, appearing in both **(b.)** and the appendices of **(a.)**.

3.1 Off-resonant effects

Far from resonance, it is no longer appropriate to model the atom as the two level system found in section 2.1, since one can no longer neglect coupling to other atomic states. To be off-resonant here requires that the radiation field is far detuned from any atomic resonance, effectively guaranteeing that for any pair of atomic states $\Omega \ll \Delta$. As a result, the RWA does not hold, so both co- and counter-rotating terms must be considered going forwards. Further, we consider the case where $\mathfrak{H}_{\text{int}}$ (equation 2.1) is a small perturbation to $\mathfrak{H}_0$ (when the combined eigenstates are close to the atomic eigenstates).

3.1.1 The light shift

Despite the absence of any significant driving, an off-resonant field still shifts the eigenstates of the combined atomic and interaction Hamiltonian away from the pure atomic states. The resultant "dressed" states can be associated with particular atomic states in the perturbative limit, but are altered by the mixing in of character from other states (see [9] for a simple overview). The resultant shift in energy levels is called the *light shift*.

This shift can be calculated for a many-level atom interacting with a classical field[1] by an application of time-dependent perturbation theory [94]. There is no contribution at first order since dipole selection rules forbid the state from coupling to itself at this order (i.e. $\mathfrak{r}_{aa} = 0$). The leading term in the light shift of atomic state a is therefore second order and is given [94,95]:

$$\delta E_a = \sum_k \left(\frac{\mathcal{E}_0^2 |\boldsymbol{\varepsilon} \cdot \mathfrak{r}_{ka}|^2}{E_{ka} - \omega} + \frac{\mathcal{E}_0^2 |\boldsymbol{\varepsilon} \cdot \mathfrak{r}_{ka}|^2}{E_{ka} + \omega} \right), \tag{3.1}$$

where k indexes *all* atomic states that are dipole coupled to a and $E_{ka} = E_k - E_a$ is the energy difference between states a and k.

The light shift is usually expressed in terms of field intensity instead of amplitude:

$$\delta E_a = 2\pi \alpha_{\mathrm{FS}} \alpha_a(\omega) I, \tag{3.2}$$

where,

$$\alpha_a(\omega) = \sum_k \left(\frac{|\boldsymbol{\varepsilon} \cdot \mathfrak{r}_{ka}|^2}{E_{ka} - \omega} + \frac{|\boldsymbol{\varepsilon} \cdot \mathfrak{r}_{ka}|^2}{E_{ka} + \omega} \right), \tag{3.3}$$

is known as the *atomic polarisability*. Writing the shift in this way draws a clear comparison with the dipole potential formed by the interaction of a neutral particle with a classical radiation field [93]. Here the atomic polarisability can be identified with the real component of the *complex polarisability*.

3.1.2 Off-resonant scattering

Following the analogy with the model in [93], there must also be a term corresponding to dissipation of energy from the field — scattering in an atomic system. In the perturbative picture that has been constructed so far, this dissipation comes from processes which change the atomic state and/or the state of the atomic field. The differential cross section for scattering from initial state a is given by the Kramers-Heisenberg formula [58, 59]:

$$\frac{\mathrm{d}\sigma}{\mathrm{d}\Omega} = \sum_b^{E_{ba} < \omega} \omega \omega_s^3 \alpha_{\mathrm{FS}}^4 \times \left| \sum_k \left(\frac{\boldsymbol{\varepsilon}_s^* \cdot \mathfrak{r}_{bk} \boldsymbol{\varepsilon} \cdot \mathfrak{r}_{ka}}{E_{ka} \mp \omega} + \frac{\boldsymbol{\varepsilon} \cdot \mathfrak{r}_{bk} \boldsymbol{\varepsilon}_s^* \cdot \mathfrak{r}_{ka}}{E_{kb} \pm \omega} \right) \right|^2, \tag{3.4}$$

where ω_s is the frequency of the scattered photon. Upper signs relate to *Raman scattering* proceeding via the absorption of a field photon and emission of a scattered photon with frequency

[1] Equivalently, both perturbative [94] and non-perturbative [59] calculations are possible for the fully quantised field. The results conform with those of a classical field in the limit of large photon numbers.

$\omega_s = -E_{ba} + \omega$. This process is referred to as Stokes or anti-Stokes for $E_b > E_a$ and $E_a > E_b$ respectively. Lower signs relate to *singly stimulated two photon emission* (SSTPE) which involves the double emission of a field frequency photon and a scattered photon $\omega_s = -E_{ba} - \omega$. singly stimulated two photon emission (SSTPE) is energetically forbidden unless $E_b < E_a$ and $E_{ab} > \omega$.

The scattered photon is emitted with direction defined by the co-latitude angle ϑ and azimuthal angle φ. The polarisation of the scattered photon $\boldsymbol{\varepsilon}_s$ can take any orientation in any direction that is normal to this direction of emission. To account for all possible orientations of $\boldsymbol{\varepsilon}_s$, it is necessary to sum across two orthogonal vectors which span the space of polarisation states for the scattered photon: $\boldsymbol{\varepsilon}_1$ and $\boldsymbol{\varepsilon}_2$. The polar angles of these vectors are denoted as ϑ_1 and φ_1 for $\boldsymbol{\varepsilon}_1$, and ϑ_2 and φ_2 for $\boldsymbol{\varepsilon}_2$; we choose:

$$\vartheta_1 = \vartheta - \frac{\pi}{2} \ , \ \varphi_1 = \varphi, \tag{3.5}$$

$$\vartheta_2 = \frac{\pi}{2} \ , \ \varphi_2 = \varphi - \frac{\pi}{2}. \tag{3.6}$$

The total atom-photon scattering rate is then given,

$$R = \int \mathrm{d}\Omega \sum_{\boldsymbol{\varepsilon}_s} \frac{\mathrm{d}\sigma}{\mathrm{d}\Omega} \frac{I}{\omega}, \tag{3.7}$$

where $\int d\Omega$ indicates integration across the solid angle of scattered photon directions. This is conveniently expressed as $R = \sum_b^{E_{ba}<\omega} R_{ba}$, where R_{ba} is the rate of scattering to particular final state b,

$$R_{ba} = \omega_s^3 \alpha_{\mathrm{FS}}^4 \int \mathrm{d}\Omega \sum_{s=1,2} \left| \sum_k \frac{(\boldsymbol{\varepsilon}_s^* \cdot \mathfrak{r}_{bk})(\boldsymbol{\varepsilon} \cdot \mathfrak{r}_{ka})}{E_{ka} \mp \omega} + \frac{(\boldsymbol{\varepsilon} \cdot \mathfrak{r}_{bk})(\boldsymbol{\varepsilon}_s^* \cdot \mathfrak{r}_{ka})}{E_{kb} \pm \omega} \right|^2 I. \tag{3.8}$$

It is phenomenologically useful to think of elastic and inelastic scattering processes separately. Inelastic scattering is the more general of the two and relates to a change in atomic state $b \neq a$. Elastic scattering preserves the atomic state $b = a$, and as a special case of Raman scattering (SSTPE is forbidden for $E_a = E_b$) it is called *Rayleigh* scattering. It should be immediate from equation 3.8 that Rayleigh scattering is closely related to the atomic polarisability of equation 3.3. The difference is, that Rayleigh scattering does not emit a photon back into the original field mode, but with arbitrary direction (see e.g. [58, 59]).

3.2 Calculating two-photon matrix elements

The atomic polarisability and atom-photon scattering rates depend upon two-photon matrix elements of the form:

$$\mathcal{M}_{ba}^{(2)} = \sum_k \frac{(\boldsymbol{\varepsilon}_I^* \cdot \mathfrak{r}_{bk})(\boldsymbol{\varepsilon}_{II} \cdot \mathfrak{r}_{ka})}{E_{ka} \mp \omega} + \frac{(\boldsymbol{\varepsilon}_{II} \cdot \mathfrak{r}_{bk})(\boldsymbol{\varepsilon}_I^* \cdot \mathfrak{r}_{ka})}{E_{kb} \pm \omega}, \tag{3.9}$$

where k indexes all states that are dipole coupled to both the initial state a and the final state b. To keep it general, the photons are distinguished by the subscript I or II on the polarisation vector. In principle, this includes summation over an infinite number of bound states, and integration over a continuum of unbound states. For calculations in alkali atoms, the continuum contributions are small enough to be neglected and the sum rapidly converges over a small number of bound states. Therefore, it is usual to compute these sums by explicitly summing across a few dominating states, taking empirical parameters (e.g. see the work in [95, 96] or similar). However, the continuum cannot be neglected in calculations with H. Attempts to explicitly perform this integral using the analytic wave-functions (equations 2.6 and 2.9) quickly stall against successive integration of hypergeometric functions.

Luckily, it is possible to calculate this matrix element including both bound and unbound states without explicitly computing an integral over continuum by one of two distinct methods. The first is an analytical approach involving the computation of Greens functions (see [60, 97, 98] for details). This allows for polarisability and scattering rates to be written analytically in terms of hypergeometric functions (e.g. [99–101]). Such calculations are technically complex, highly involved, and the formulae are not general — relating to a single process with specific atomic states a and b. The second is a numerical approach, which was first applied in the pioneering calculations of Zernik [102] but has seen significant use since then [103–105]. Unlike the analytic approach, it can be applied to any set of atomic states with minimal variation, and so is used for calculations in **(a)** and **(b)**. It proceeds as follows.

3.2.1 Implicit summation

For later convenience I will express the matrix element 3.9 as two sums,

$$\mathcal{M}^{(2)}_{ba} = \sum_k \frac{(\boldsymbol{\varepsilon}^*_I \cdot \mathfrak{r}_{bk})(\boldsymbol{\varepsilon}_{II} \cdot \mathfrak{r}_{ka})}{E_{ka} \mp \omega} + \sum_k \frac{(\boldsymbol{\varepsilon}_{II} \cdot \mathfrak{r}_{bk})(\boldsymbol{\varepsilon}^*_I \cdot \mathfrak{r}_{ka})}{E_{kb} \pm \omega}, \tag{3.10}$$

labelled (i) and (ii) respectively. Following the example of [104, 105], I apply an implicit summation method (also called the Dalgarno-Lewis method [106, 107]) to express sum (i) in closed analytic form,

$$\sum_k \frac{\boldsymbol{\varepsilon}^*_I \cdot \mathfrak{r}_{bk} \boldsymbol{\varepsilon}_{II} \cdot \mathfrak{r}_{ka}}{E_k - E_a \mp \omega} = \langle b| \boldsymbol{\varepsilon}^*_I \cdot \mathfrak{r} \sum_k \frac{|k\rangle \langle k|}{E_k - E_a \mp \omega} \boldsymbol{\varepsilon}_{II} \cdot \mathfrak{r} |a\rangle . \tag{3.11}$$

It then follows by the spectral theorem that,

$$\sum_k \frac{\boldsymbol{\varepsilon}^*_I \cdot \mathfrak{r}_{bk} \boldsymbol{\varepsilon}_{II} \cdot \mathfrak{r}_{ka}}{E_k - E_a \mp \omega} = \langle b| \boldsymbol{\varepsilon}^*_I \cdot \mathfrak{r} \frac{1}{H_0 - (E_a \pm \omega)} \boldsymbol{\varepsilon}_{II} \cdot \mathfrak{r} |a\rangle . \tag{3.12}$$

A similar result is also found for sum (ii).

The second order matrix elements can then be written as the sum of two first order matrix elements,

$$\mathcal{M}^{(2)}_{ba} = \langle b| \boldsymbol{\varepsilon}^*_I \cdot \mathfrak{r} |\psi_{(i)}\rangle + \langle b| \boldsymbol{\varepsilon}_{II} \cdot \mathfrak{r} |\psi_{(ii)}\rangle , \tag{3.13}$$

where the vectors $|\psi_{(i)}\rangle$ and $|\psi_{(ii)}\rangle$ solve the equations

$$[H_0 - (E_a \pm \omega)] |\psi_{(i)}\rangle = \boldsymbol{\varepsilon}_{II} \cdot \mathfrak{r} |a\rangle \text{ and } [H_0 - (E_b \mp \omega)] |\psi_{(ii)}\rangle = \boldsymbol{\varepsilon}^*_I \cdot \mathfrak{r} |a\rangle . \tag{3.14}$$

In general, the vectors $|\psi_{(i)}\rangle$ and $|\psi_{(ii)}\rangle$ include contributions from both the discrete and continuous parts of the spectrum and cannot be described with the basis of bound eigenstates.

3.2.2 The Sturmian basis

Following the example of [98, 104, 105, 108], I construct a discrete set of Laguerre functions, multiplied by the spherical harmonics:

$$\mathcal{B} = \left\{ \frac{1}{r} S^{(\zeta)}_{\mathtt{n},\mathtt{l}}(r) Y_{\mathtt{lm}}(\theta, \phi) : \mathtt{n} \in \mathbb{N}, \mathtt{l} \in \mathbb{N}_0, |\mathtt{m}| \leq l \right\}, \tag{3.15}$$

where $\zeta \in \mathbb{R} > 0$ is a free parameter. The numbers $\mathtt{n}$ and $\mathtt{l}$ index the Sturmian functions,

$$S^{(\zeta)}_{\mathtt{nl}}(r) := \mathcal{N}_{\mathtt{nl}} (2\zeta r)^{\mathtt{l}+1} e^{-\zeta r} L^{2\mathtt{l}+1}_{\mathtt{n}-1}(2\zeta r), \tag{3.16}$$

where $L_x^y(s)$ are the associated Laguerre polynomials. These functions are normalised $\mathcal{N}_{\mathtt{nl}} = \sqrt{(\mathtt{n}-1)!/(\mathtt{n}+2\mathtt{l})!}$ such that,

$$\int_0^\infty r^2 dr \left(\frac{1}{r} S^{(\zeta)}_{\mathtt{n'l}}\right) \frac{1}{r} \left(\frac{1}{r} S^{(\zeta)}_{\mathtt{nl}}\right) = \delta_{\mathtt{n'n}}. \tag{3.17}$$

Orthogonality in the indices $\mathtt{l}$ and $\mathtt{m}$ is assured by the orthonormality of the spherical harmonics that give the angular components of $\mathcal{B}$. In fact, these angular components are exactly the angular parts of the hydrogen wave-functions (both bound and unbound) and the indices $\mathtt{l}$ and $\mathtt{m}$ can be identified with the orbital angular momentum and magnetic quantum numbers l and m. Meanwhile, the radial functions of $\mathcal{B}$ form a complete set spanning the $L^2(0,\infty)$ Hilbert space — that is the space of square integrable functions over the semi-definite interval (by construction as a set of Laguerre functions, see [109] for proof). Clearly, $\mathcal{B}$ forms a complete set across the Hilbert space relevant to the hydrogen wave-functions[1] and any hydrogen wave-function can be expressed as a linear combination of functions in $\mathcal{B}$:

$$R_{nl}(r)Y_{lm}(\theta,\phi) = Y_{lm}(\theta,\phi) \sum_{\mathtt{n}\in\mathbb{N}} C_{\mathtt{n},n,l} \frac{1}{r} S^{(\zeta)}_{\mathtt{n}l}(r), \tag{3.18}$$

where $C_{\mathtt{n},n,l}$ are constants which define a vector in $\mathcal{B}$.

3.2.3 Solving the Schrödinger equation

Indeed, any atomic state c is represented in the Sturmian basis by some vector $\boldsymbol{c}$. These vectors can be produced by solving the relevant time-independent Schrödinger equation as a generalised eigenvalue problem,

$$\mathcal{H}\boldsymbol{c} = E_c \mathcal{T}\boldsymbol{c}. \tag{3.19}$$

Here $\mathcal{H}$ is the matrix representing the atomic Hamiltonian (equation 2.4) in $\mathcal{B}$ and $\mathcal{T}$ is the overlap matrix, which accounts for the non-trivial overlap between the Sturmian functions (since $\int_0^\infty dr S^{(\zeta)}_{\mathtt{n'},l} S^{(\zeta)}_{\mathtt{n}l} \neq \delta_{\mathtt{n'},\mathtt{n}}$ by equation 3.17). Both matrices are expressed in terms of the analytic matrix elements in equation A.3 and A.5. Since the overlap between the angular parts of $\mathcal{B}$ is trivial, $\mathcal{T}$ is diagonal in both l and m. This is also true for $\mathcal{H}$ since neither the basis $\mathcal{B}$ or H_0 include any mixing in l or m.

[1] In fact, this is true any wave-function in a central potential that is normalised as $\int d\boldsymbol{r}^3 |\Psi(\boldsymbol{r})|^2 = 1$.

Any non-relativistic state will have well-defined quantum numbers l_c and m_c, so the associated vector $\boldsymbol{c}$ is only non-zero for functions of $\mathcal{B}$ with $l = l_c$ and $m = m_c$. As such, equation 3.19 can be re-cast as an eigenvalue problem over a radial[1] sub-set of $\mathcal{B}$ which is only indexed by n:

$$\mathcal{H}_{l_c}\boldsymbol{c} = E_c\mathcal{T}_{l_c}\boldsymbol{c}, \tag{3.20}$$

where $\mathcal{H}_{l_c}$ and $\mathcal{T}_{l_c}$ are matrices over n with a single well defined value of $l = l_c$. Such a problem can be solved very efficiently with numerical methods, but requires a finite basis set. This is achieved by restricting the index n to some finite set of positive integers: $\mathtt{n} \in \mathbb{N} \leq \mathtt{n}_{\max}$. Each state can be identified in a computational spectrum by its eigenvalue E_c which is unique given l is fixed.

3.2.4 Full calculations

The electric dipole operator, $\mathfrak{r}$ also needs to be represented as a matrix in $\mathcal{B}$. This operator always appears in dot product with a photon polarisability $\boldsymbol{\varepsilon}$, and the matrix elements between atomic states a and b are separable,

$$\boldsymbol{\varepsilon} \cdot \mathfrak{r}_{ba} = \sum_{q\in\{0,\pm1\}} \varepsilon_q A_{l_b m_b q, l_a m_a} r_{ba}, \tag{3.21}$$

where q indexes the polarisation over a basis of spherical unit vectors ($\boldsymbol{\varepsilon} = \sum_{q\in\{0,\pm1\}} \varepsilon_q \hat{\boldsymbol{\epsilon}}_q$, see appendix A.2), and the angular $A_{l_b m_b q, l_a m_a}$ and radial matrix elements r_{ba} are defined in equationsA.10 and A.8. The angular component can be calculated analytically, and contains all m dependence. Unlike the Hamiltonian, this operator is not diagonal in l, but couples l to $l \pm 1$. To account for this, the radial part is represented as the sum of two matrices: $\mathcal{R}_l^+$ which couples a given l to $l+1$; and $\mathcal{R}_l^-$ which couples to $l-1$ (see appendix A.2 for analytic expressions of the matrix elements). Each of these is a matrix in $\mathcal{B}$, but extends only over the index n, it sits in the off diagonal formed by l and $l \pm 1$ for a chosen value l.

I will now limit consideration to cases where the initial state a is an S-state, i.e. $l_a = 0$. This simplifies matters as a now couples only to the l-raising part of the dipole operator and intermediate states are limited to P-states. Consider computing sum (i): $|\psi\rangle_{(i)}$ must have a

[1] As equation 3.18 indicates that writing an atomic wave unction in the Sturmian basis is a decomposition over the radial functions only.

well defined $l = 1$ and so is represented by a single vector over the index $\mathtt{n}$. This vector can be calculated by solving the matrix equation over the index $\mathtt{n}$,

$$[\mathcal{H}_{l=1} - (E_a \pm \omega)\mathcal{T}_{l=1}]\,\boldsymbol{\psi}_{(i)} = \mathcal{R}^{+}_{l=0}\boldsymbol{a}. \tag{3.22}$$

Unlike equation 3.20, this is not strictly within a subset of $\mathcal{B}$ defined by a chosen value of l (since the RHS has $l = 0$ whilst the LHS has $l = 1$). However, it can be solved effectively as a matrix equation over the index $\mathtt{n}$ only, as terms with other values of l will ultimately vanish.

The final state b is limited by dipole selection rules to only S-states or D-states, i.e. $l_b = 0$ or 2. If $l_b = 0$ then the radial part of sum (i) can be calculated by computing the inner product,

$$\boldsymbol{b}^T\mathcal{R}^{-}_{1}\boldsymbol{\psi}_{(i)}. \tag{3.23}$$

Otherwise, if $l_b = 2$, then the relevant inner product is instead,

$$\boldsymbol{b}^T\mathcal{R}^{+}_{1}\boldsymbol{\psi}_{(i)}. \tag{3.24}$$

Again, this system of matrix equations is best treated numerically over a finite basis size. In the same way as in section 3.2.3, this is done by restricting $\mathtt{n}$ to range up to some defined maximum[1] $\mathtt{n}_{\max}$.

The total value of sum (i) is then obtained by multiplying the radial component by the total angular contribution, $\sum_{q\in\{0,\pm1\}} \varepsilon_q A_{l_b q q,10} A_{1q0,00}$. The same approach can be used to compute sum (ii) where $\boldsymbol{\psi}_{(ii)}$ solves a similar matrix equation to 3.22, adjusted in line with equation 3.14, and the angular part is $\sum_{q\in\{0,\pm1\}} \varepsilon_q A_{l_b q 0,1q} A_{1qq,00}$ instead. Their sum gives the final value of $\mathcal{M}^{(2)}_{ba}$.

3.3 Numerical Results

The calculations described in the previous section are realised numerically in the software [2] described in **(b.)**. Extensive use is made of the numPy and sciPy packages to solve both the Schrödinger equation (3.19) and equations 3.22, 3.23, and 3.24. This code allows for the

[1] It is worth noting that the computational solution will become exact as $\mathtt{n}_{\max} \to \infty$. Such a calculations can be thought of as 'numerically exact' as they can, in principle, be calculated to any desired precision given sufficient time and resources.

calculation of polarisability and atom-photon scattering rates for S-states of atomic H, D, and even T in the presence of a linearly polarised optical field with user-defined frequency. Both the size of the Sturmian basis (via the maximum value of $\mathtt{n}$ — "$\mathtt{n}_{\max}$") and the value of the free parameter ζ are user defined for each calculation. In all the calculations that follow, I choose $\mathtt{n}_{\max} = 300$ and $\zeta = 0.3$ which is sufficient to ensure convergence for low-lying states.

3.3.1 Polarisability

The polarisability is trivially given by the matrix element $\mathcal{M}^{(2)}_{aa}$ as per equation 3.3. It is straightforward to compute the angular terms under the assumption of linearly polarised light in the $\hat{\boldsymbol{z}}$ direction, i.e. $q = 0$:

$$A_{100,00}A_{000,10} = \frac{1}{\sqrt{3}} \times \frac{1}{\sqrt{3}} = \frac{1}{3}. \tag{3.25}$$

Multiplying this by the numerical solutions to the radial part of $\mathcal{M}^{(2)}_{aa}$ as detailed in section 3.2.4 immediately gives the polarisability of a given S-state a.

The polarisability is plotted in figure 3.1 for both the 1S and 2S states of H for wavelengths ranging from 91 to 800 nm. These results conform very well with the results of an analytic calculation (see Appendix B) away from resonance. On resonance with bound P-states, the denominator of sum (i) vanishes and the polarisability diverges, resulting in a series of poles in figure 3.1. Here $\Omega > \Delta$ and the small perturbation assumption does not hold, so interactions are dominated by the first order resonant transitions of chapter 2.

For wavelengths shorter than the one-photon ionisation threshold (91.3 nm for 1S and 356 nm for 2S) the polarisability is dominated by a forest of poles relating to coupling with the continuum. As such, the polarisability is not plotted for each state beyond this threshold. On the other hand, for wavelengths larger than the lowest Lyman/Balmer wavelength, the polarisability tends asymptotically towards the D.C. polarisability.

Notice that the polarisability of the 1S state is generally much lower than that of the 2S state at optical wavelengths. This is a result of the tight binding of the spherically symmetric ground state and the large energy differences between it and higher lying P-states. The poor polarisability of H in its ground state becomes more clear under comparison with other atomic

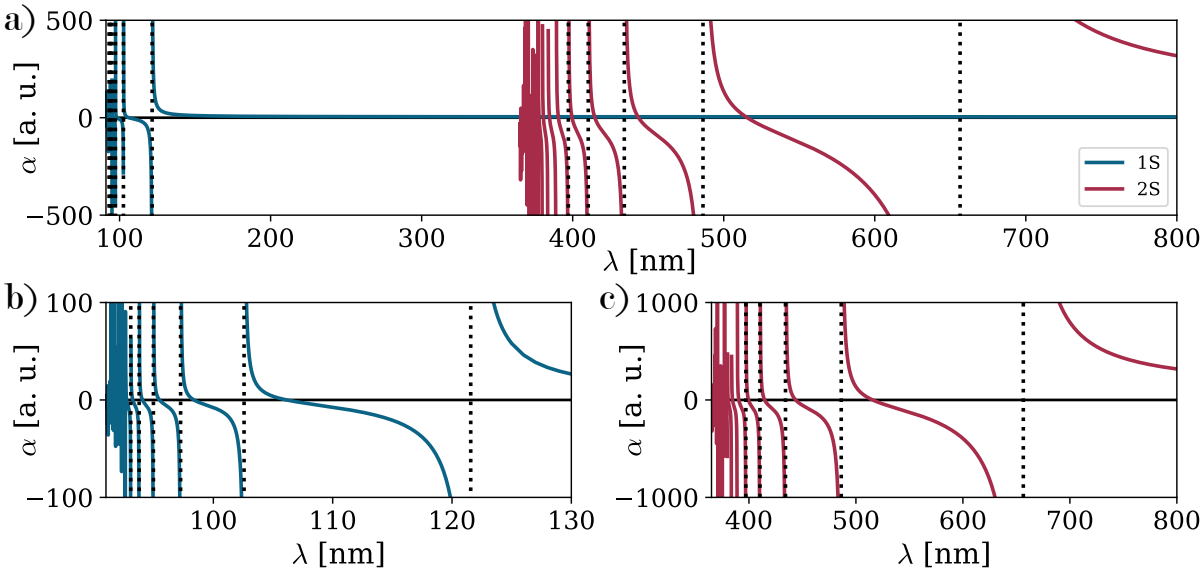

Figure 3.1: The polarisability of both the 1S (blue) and 2S (red) states are shown together in plot a) from 91 to 800nm. Plots b) and c) show the polarisability of the 1S and 2S states respectively each in the region closest to the relevant nP resonances. These 1S and 2S–nP resonances are denoted with black dotted lines up to n=6. The polarisability is not plotted beyond the ionisation threshold — where a forest of continuum resonances dominate.

species. For example, the polarisability of the strontium ground state at 813 nm is 280 a.u. [110] — around 60 times larger than for ground state H.

3.3.2 Off-resonant scattering

Computing the scattering rates is more involved than computing the polarisability as one must integrate over the scattered photon direction. Assuming an initial S-state, $l_a = 0$ and linearly polarised optical field, $\hat{\boldsymbol{\varepsilon}} = \hat{\boldsymbol{z}}$ (or $q = 0$), equation 3.8 can be written as a purely radial sum, multiplied by a shared angular term $\mathcal{A}_{ba}$ (see appendix A.3 for details):

$$\sum_{m_b} R_{ba} = \omega_s^3 \alpha_{\mathrm{FS}}^4 \mathcal{A}_{ba} \left(\sum_k \frac{r_{bk} r_{ka}}{\omega_{ka} \mp \omega} + \frac{r_{bk} r_{ka}}{\omega_{kb} \pm \omega} \right)^2 I, \tag{3.26}$$

where there is an explicit summation over m_b. This is done as, in the absence of an external magnetic field, states with different m_b are degenerate for a given pair n_b, l_b. Note that, since it is assumed that a is an S-state, there is only one value of $m_a = 0$.

The radial sum can be computed numerically as described in section 3.2.4. The angular term is common to both sum (i) and (ii) and can be calculated analytically (again, see appendix A.3

for details),

$$\mathcal{A}_{ba} = \frac{8\pi}{3}\left(\left(A_{l_b 00,10}A_{100,00}\right)^2 + 2\left(A_{l_b(\pm1)(\pm1),10}A_{100,00}\right)^2\right). \tag{3.27}$$

Here the factor of $8\pi/3$ comes from integration of the scattered photon direction and summation over orthogonal polarisations.

For scattering between S states, only $m_b = 0$ is possible and the overall angular term is given:

$$\mathcal{A}_{ba} = \frac{8\pi}{3}\left(\frac{1}{\sqrt{3}} \times \frac{1}{\sqrt{3}}\right)^2 + 0 = \frac{8\pi}{27}. \tag{3.28}$$

By combining equations 3.26 and 3.28 with the definition of atomic polarisability 3.3, one may write the Rayleigh scattering rate as,

$$R_{aa} = \omega^3 \alpha_{\mathrm{FS}}^4 \frac{8\pi}{3}|\alpha_a(\omega)|^2. \tag{3.29}$$

Doing so highlights the close relationship between Rayleigh scattering and the light shift[1] and allows for convenient computation if the polarisability is already known.

When b is a D-state, m_b is restricted to 0 or ±1 by dipole selection rules and the overall angular term is now:

$$\mathcal{A}_{ba} = \frac{8\pi}{3}\left[\left(\sqrt{\frac{4}{15}} \times \sqrt{\frac{1}{3}}\right)^2 + 2\left(\sqrt{\frac{2}{10}} \times \sqrt{\frac{1}{3}}\right)^2\right] = \frac{16\pi}{27}. \tag{3.30}$$

Technically, for b to be considered a single atomic state it must have well defined n, l, *and* m. By summing over m_b, what I am actually considering is the scattering rate from well defined atomic state a to all final states with n_b and l_b. Henceforth, when discussing scattering rates, this sum over m_b will be implied and final states will be identified according to their n, l values: e.g. 3S, or 5D. To obtain the scattering rate for a single value of m_b all one needs to do is to include only the appropriate angular terms; e.g. for scattering to an $l_b = 2$, $m_b = 1$ state, in an external field that is linearly polarised along the $\hat{\boldsymbol{z}}$ direction, the angular term is given $\mathcal{A}_{ba} = (8\pi/3) \times (\sqrt{1/5} \times \sqrt{1/3})^2 = 8\pi/45$.

Both the elastic and total inelastic (summing across Raman scattering and SSTPE processes for *all* allowed final states) scattering rates out of the 2S state are presented in figure 3.2 a).

[1] In the two state model presented by Grimm *et. al.* [93], the scattering given by the imaginary component of the complex polarisability is exactly a Rayleigh process, and a similar relation is obtained.

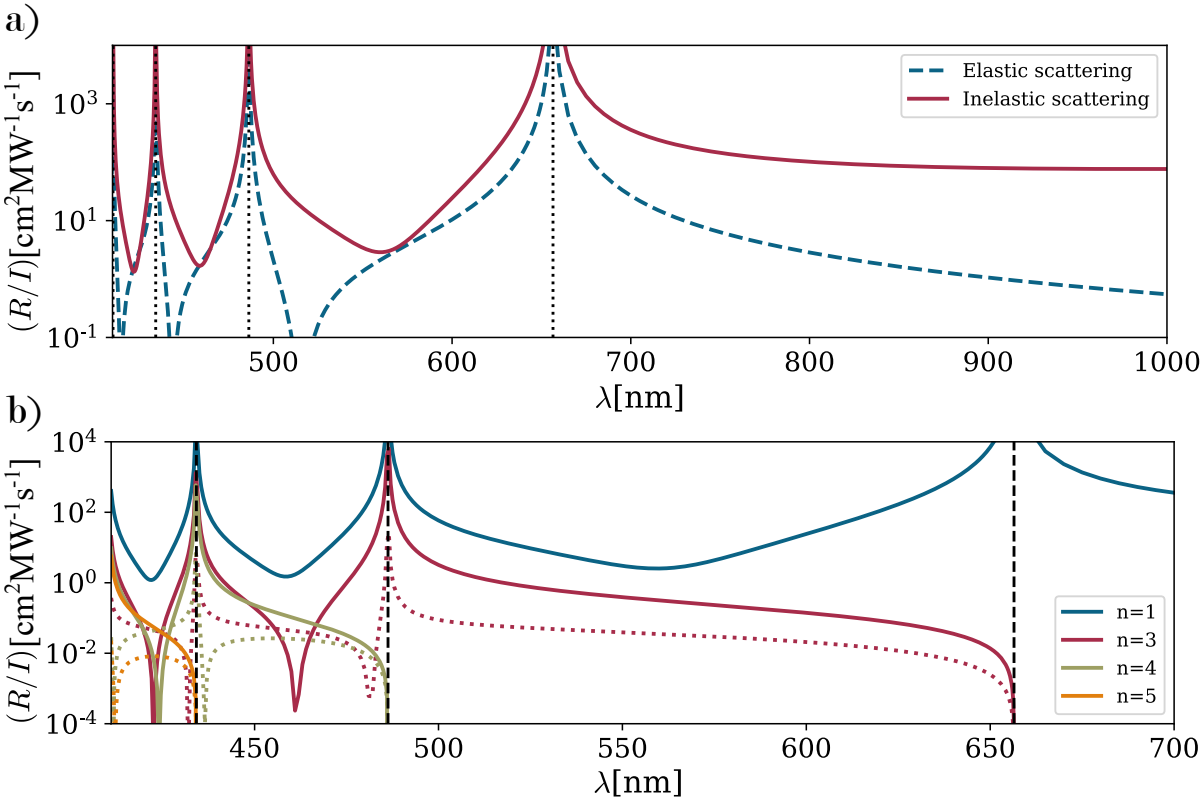

Figure 3.2: Plots of scattering rates out of the 2S state of H across a range of mostly optical wavelengths. Plot a) shows the elastic scattering (dashed blue line) and total inelastic scattering (solid red line) from 410–1000 nm. Plot b) shows the inelastic scattering rate decomposed according to final n, l states (summing across m and including both Raman scattering and SSTPE). Solid lines indicate final S-states while dotted lines indicate final D-states. In both cases, rates are given per second per unit intensity (measured in units of $\mathrm{MWcm^{-2}}$) and black dashed lines indicate 2S-nP resonances.

Both elastic and inelastic scattering rates diverge at the 2S–nP resonances, as for polarisability. Further, the elastic scattering rate drops to zero at one point between each pair of resonances: this relates to a point where the 2S polarisability changes sign. Since $R_{aa} \propto |\alpha_a|^2$ it does not change sign with α_a, but does vanish at the crossing point. In general, it is clear that inelastic scattering is faster than elastic scattering, particularly in regions that are red-detuned from 2S–nP resonances.

Figure 3.2 b) shows the breakdown of the inelastic scattering rate according to final n, l state. Again, these results conform well with liturature values (see appendix C). The 1S state is lower energy than the 2S state and so is accessible via both anti-Stokes Raman scattering and SSTPE at all wavelengths. Scattering to higher lying states is only possible via Stokes Raman

scattering when the frequency of the optical field is high enough to allow this transition[1]. Scattering to the ground, 1S, state clearly dominates the total inelastic scattering rate at all wavelengths, with contributions from high-lying states being very small.

3.3.3 Calculation accuracy

The calculations discussed in this chapter, and performed by the software described in **(b.)**, are done within the non-relativistic theory: the non-relativistic Hamiltonian, equation 2.4, is used and atomic states are given in terms of quantum numbers n, l, and m. The leading order corrections to $\mathcal{M}_{ba}^{(2)}$ come from relativistic effects and field configuration terms which are $O(\alpha_{\mathrm{FS}}^2)$ (see e.g. [101, 111]). This is by far the dominating source of theoretical uncertainty in successive calculations with $\mathcal{M}_{ba}^{(2)}$ and reasonably limits the physical accuracy of polarisability or scattering rates to four significant figures. Where literature values are available, they agree with the numerical results to the level of physical significance (see appendix B).

The computational uncertainty is essentially set by the choice of basis parameters $\mathtt{n}_{\max}$ and ζ. The basis must be large enough to ensure proper convergence over the sums, but a larger basis set is naturally more resource intensive. Larger basis sets are also needed to ensure convergence for calculations involving high-lying states. Further, larger values of ζ cause results to converge more slowly and so also require larger basis sets. Since the choice of ζ is arbitrary, it is convenient to use a small value. Choosing $\mathtt{n}_{\max} = 300$ and $\zeta = 0.3$ results in final values with an estimated computational uncertainty of less than $O(10^{-9})$ (measured by small variations the basis parameters, see **(b.)**) — far smaller than the physical significance of $O(\alpha_{\mathrm{FS}}^2)$.

The only difference between H and D in the the non-relativistic theory is a difference in the reduced mass $O(10^{-4})$. The resultant shift between results of $\mathcal{M}_{ba}^{(2)}$ is of a similar order. So one can expect to see a difference between results for H and D only on the last physically significant figure. Further, the interactions of H and $\bar{\mathrm{H}}$ with optical fields are necessarily identical (under conservation of CPT). As such, the results for H also apply to $\bar{\mathrm{H}}$.

These accurate calculations are an essential first step, not only towards optical trapping of H, but in assessing its suitability for precision spectroscopy. The ability to calculate the polarisab-

[1] In the non-relativistic theory, nS, nP and nD states are degenerate, so this limit is exactly the 2S-nP resonance.

ility at arbitrary wavelengths will be essential to choosing appropriate trapping fields. Further, the atom-photon scattering rates limit the coherence times of trapped atoms, and will help me to optimise the trapping fields and experimental setup. Whilst calculations of this sort have been done before, it is useful to have them unified into a single set of numerical methods that are extendable to a wide range of states. It is this generalisability that allowed new results of scattering rates on the 2S–nS/D, for $n > 3$ to be contributed to the literature.

Chapter 4

MEASUREMENT IN OPTICAL LATTICES

In chapter 2, I motivate a step change from spectroscopy in atomic beams to spectroscopy in cold, optically trapped atoms. Chapter 3 then provides tools for discussing optical trapping and the related effects of scattering. It is time to put these tools to use and assess the suitability of a sample of cold, trapped H for precision spectroscopy. I will focus my attention on the prospective 1S–2S lattice clock discussed in **(a.)**, which will act as an example system for further discussion. Not only is this system the most obvious analogue of the OLC that motivates the move to trapped atoms, but it holds special significance in the H spectral dataset and the unusually long lifetime makes it well suited to a trapped atom measurement. The work presented in this chapter is heavily based upon the declared publication **(a.)**.

4.1 The 1S–2S lattice clock

I will consider the simple 1D lattice clock described in figure 4.1: single H atoms are confined in a 1D lattice formed by a standing wave with angular frequency ω_{latt}. The 1S–2S transition is driven by Doppler-free excitation in a retro-reflected 243 nm beam oriented along the same axis as the lattice. The anti-nodes of the 243 nm wave do not necessarily coincide with the lattice sites in this set up. I note that this effect can be overcome by crossing the lattice beams at a small angle and will not discuss it further.

4.1.1 A magic wavelength lattice

The one dimensional lattice is described by the spatially varying potential (see figure 4.1):

$$U_{\mathrm{latt}}(z) = -U_0 \sin^2(k_{\mathrm{latt}} z), \tag{4.1}$$

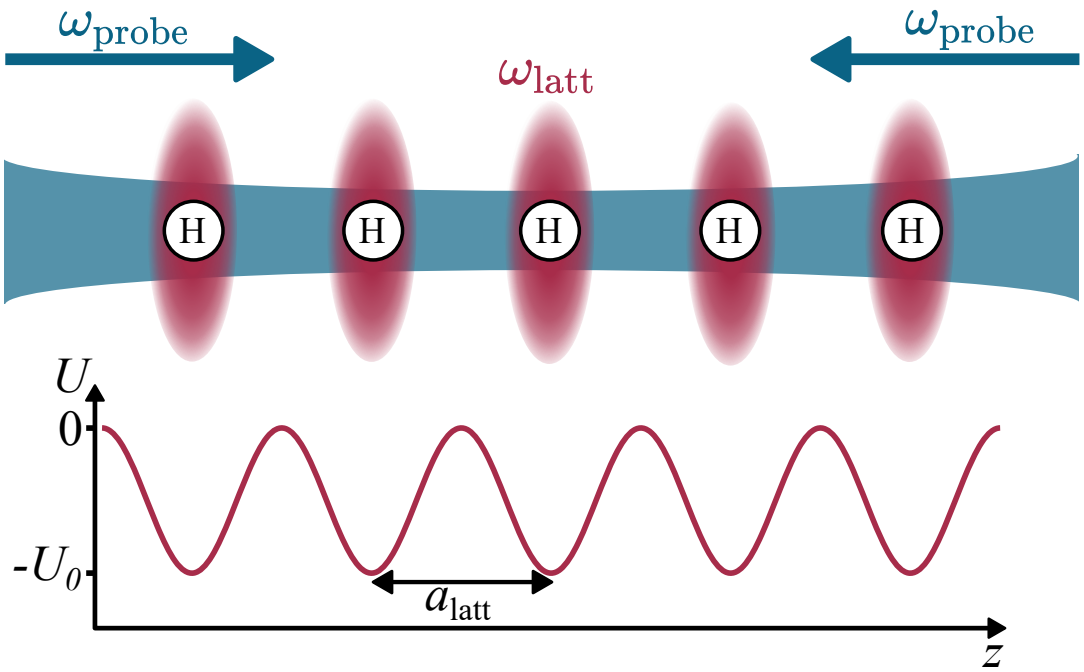

Figure 4.1: Schematic diagram showing the proposed 1D clock. The 1S–2S transition will be driven by two counter-propagating 243 nm beams (represented in blue) that runs co-parallel with a 1D lattice (represented in red). Below that is a plot of the lattice potential, with the lattice constant $a_{\text{latt}} = \lambda_{\text{latt}}/2$ indicated.

where $k_{\text{latt}} = \omega_{\text{latt}}\alpha_{\text{FS}}$ is the angular wave-number of the lattice field and the maximum shift depends upon the peak intensity I_0 as,

$$U_0 = -2\pi\alpha_{\text{FS}}\alpha_a(\omega_{\text{latt}})I_0. \tag{4.2}$$

The depth of the lattice, $|U_0|$ best characterised according to the single photon recoil energy[1] $E_{\text{rec}} = \omega^2\alpha_{\text{FS}}^2/2m_{\text{H}}$, resulting in the dimensionless lattice depth $D = |U_0|/E_{\text{rec}}$ that is more suited to comparison between lattice fields.

It is highly desirable to choose a *magic wavelength* — where the polarisability of both states is equal. Trapping at a magic wavelength eliminates intensity-dependent shifts to the transition frequency that arise from a differential light-shift between the two states. These wavelengths can be estimated by plotting the polarisability of the 1S and 2S states and looking for intersections, as in figure 4.2. To find explicit values for magic wavelengths for the 1S–2S transition in H, I use a Newton-Raphson approach to numerically solve $\alpha_{2S}(\omega) - \alpha_{1S}(\omega) = 0$ in regions around the intersections [2]. I report four magic wavelengths in the range 395–700 nm: 514.646, 443.212, 414.483 and 399.451 nm. The first magic wavelength is already well known in the lit-

[1] Again, this is given in atomic units.

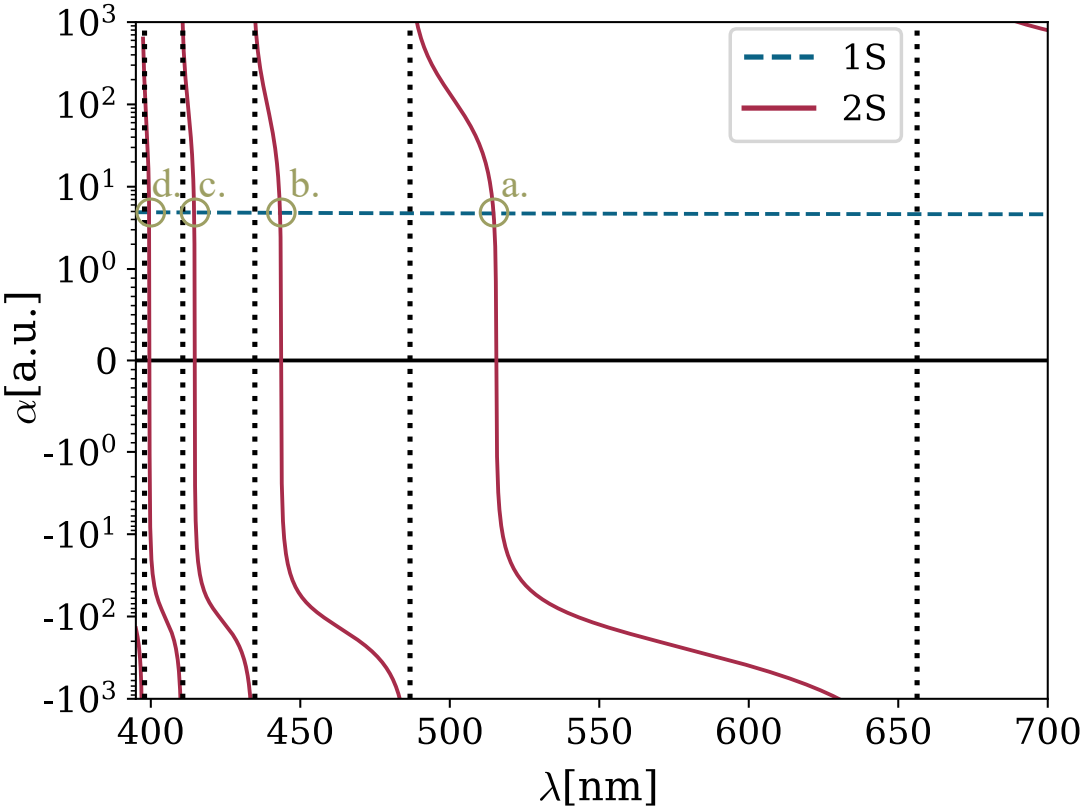

Figure 4.2: The polarisability of the 1S (dashed blue line) and 2S (solid red lines) of H over the wavelength range 395–700 nm. 2S-nP resonances are indicated with dotted black lines. Magic wavelengths are indicated with green circles and labelled: a) - 514.6 nm, b) - 443.2 nm, c) - 414.5 nm, and d) - 399.5 nm.

erature [101, 111], but the others were first reported in **(a.)** (and form part of the results of this thesis).

As discussed in section 3.3.3, values of the atomic polarisability calculated in the non-relativistic theory are physically meaningful up to 4 significant figures, with leading order relativistic and field configuration corrections at $O(\alpha_{\mathrm{FS}}^2)$. Taking a functional approach to error propagation [112], I find that these corrections affect the value of the magic wavelength only as $O(10^{-7})$. The results of my calculation — both values of the magic wavelength and the associated polarisability — conform exactly to the analytical results of Adhikari *et. al.* to this level (where comparison is applicable, see appendix B).

Whilst reporting calculated values of the magic wavelengths to 6 significant figures is justified, a more conservative estimate of the physical accuracy is common in the literature. It is usual to report magic wavelengths to the same level as the polarisability (four significant figures) but use the more accurate value for following calculations to avoid introducing additional error

Table 4.1: Properties associated with the first four 1S–2S magic wavelengths λ_{m}: atomic polarisability α, the gradient of the differential polarisability (in units of $\frac{e^2a_0^2/E_{\mathrm{H}}}{\mathrm{nm}}$, i.e. atomic units of polarisability per nm) and the lattice intensity per unit depth.

λ_{m}[nm]	α[a.u.]	$(d\alpha/d\lambda)\left[\frac{e^2a_0^2/E_{\mathrm{H}}}{\mathrm{nm}}\right]$	$I/D\left[\mathrm{MWcm}^{-2}\right]$
514.6	4.728	-5.213	3.373
443.2	4.810	-12.90	4.470
414.5	4.857	-24.89	5.062
399.5	4.886	-42.09	5.417

(e.g. see [101,111]). This convention is adopted hence-fourth and illustrated in table 4.1, which presents the four calculated magic wavelengths, along with the atomic polarisability[1] and local slope in the differential polarisability. This table also shows the peak lattice intensity required to trap at these wavelengths per unit depth (in recoils). Since the polarisabilty of the 1S state is so small, these are very large, $\sim O(1)\mathrm{MWcm}^{-2}$. Such intensities can be achieved with some effort, particularly at 514.6 nm where significant power is available from frequency doubled 1029 nm radiation (see [51, 113]).

There are many more 1S–2S magic wavelengths than are reported here; in fact there are infinitely many — one in between each pair of 2S–nP resonances (see figure 4.2). Progressing through the series of magic wavelengths, they rapidly become more unstable as the local slope in the 2S polarisability becomes larger (again see figure 4.2 for a visual example of this). Since the interval between successive wavelengths also rapidly decreases, there is not much to be gained from considering arbitrarily many values. The four most stable wavelengths will suffice for the following discussions.

The magic wavelengths for the 1S–2S transition in D are very similar, differing in the fourth significant figure. As such, the discussion in this chapter applies equally well to D as to H with only small variations between the exact values in each case. Further, the results are entirely applicable to $\bar{\mathrm{H}}$.

[1]Note that these differ on the least significant figure from the values reported in [1]. This is because these values were calculated according to the 1S state, where as those in the paper were calculated according to the 2S state. This difference then arises from calculating using only 6 significant figures in the magic wavelength as the 2S state has a much larger polarisability gradient to the 1S. Since the remaining results of [1] (and section 4.4) are reported to 3 sig. fig. this discrepancy is not propagated.

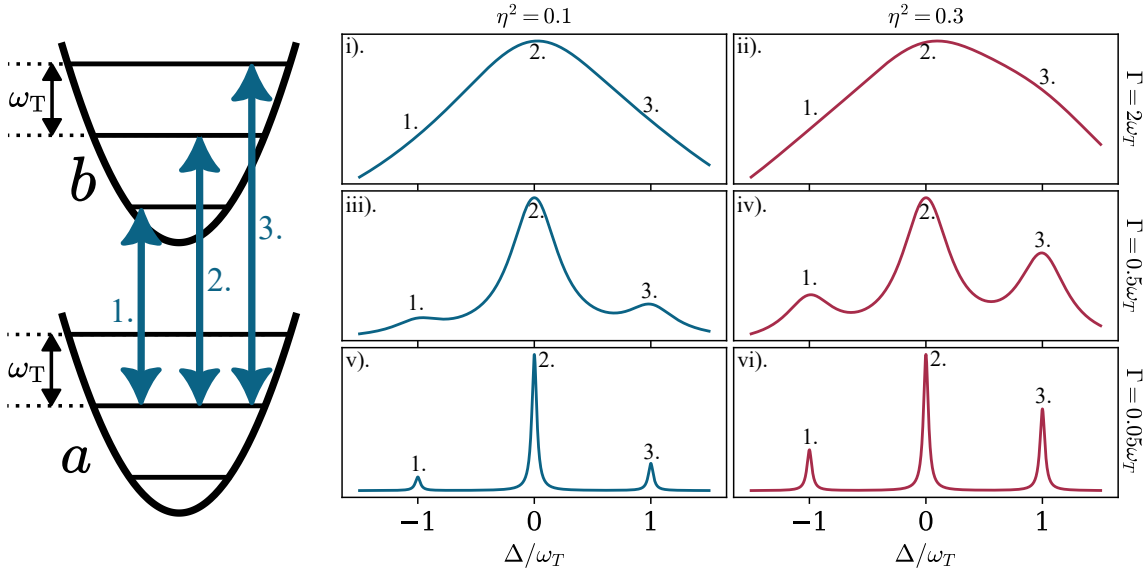

Figure 4.3: Diagram of atomic states a and b at the bottom of a given site in an optical lattice. The horizontal lines represent vibrational states, separated by the trap frequency ω_T — the same for both a and b at a magic wavelength. The arrows labelled 1, 2, and 3, indicate transitions between a and b with concurrent changes to the occupied vibrational state of -1, 0, and $+1$ respectively. These vibrational state transitions are also indicated in the plots labelled i)–vi), which show the spectral line associated with the transition for different values of η^2 and Γ.

4.2 Atomic motion in a local trap

Note: henceforth, it is more convenient to work in terms of S.I. units rather than atomic units.

Cold atoms in deep lattices are localised to the bottom of a single lattice site where it experiences an approximately harmonic local potential. In such a harmonic potential, atomic motion (in the lattice axis z) is restricted to a series of discrete vibrational states, n (see figure 4.3)[1], that are separated by the trap frequency,

$$\omega_T = 2\pi\nu_T = \sqrt{D}\frac{2\pi h}{m_H \lambda^2}. \tag{4.3}$$

The low mass of H results in noticeably larger trap frequencies than is usual in other species — $\nu_T \approx \sqrt{D} \times 2\,\text{MHz}$ at optical wavelengths, around 80–90 times larger than for strontium (Sr) or rubidium (Rb) (equivalent to the mass ratios).

This quantisation of momentum states changes how atomic recoil under photon absorption must be considered. In free space, when an atomic transition is driven by the absorption of

[1]Note that this n is different to the principal quantum number defined previously, but context should be sufficient to differentiate their meaning.

photon(s) from an external field, this comes with an associated change in linear momentum. In a trapped atom, momentum changing effects are restricted exciting discrete transitions between vibrational states, $n \to n'$; coinciding with a shift to the transition frequency of $\Delta n\omega_{\mathrm{T}}$. There are two regimes that are of particular interest to spectroscopy:

- **The Resolved side-band limit:** When the separation of vibrational states is much larger than the line-width, $\nu_{\mathrm{T}} \gg \Delta\nu_{\mathrm{FWHM}}$, the signal is split into a series of independently resolvable lines, each relating to a different vibrational transition. This effect can be seen in the subplots of figure 4.3: as the ratio $\Delta\nu_{\mathrm{FWHM}}/\nu_{\mathrm{T}}$ decreases, signals relating to the three vibrational transition become distinguishable.

- **The Lamb-Dicke regime:** When the separation of vibrational states is much larger than the recoil energy, $h\nu_{\mathrm{T}} \gg E_{\mathrm{probe}}$, transitions between vibrational states are suppressed [93]. Often parameterised in terms of the Lamb-Dickie parameter $\eta = E_{\mathrm{probe}}/h\nu_T$, this effect can be seen in the subplots of figure 4.3: as η increases the ratio of signal relating to the three vibrational transitions changes.

When operating within these two regimes, all motional effects are resolved into independent carrier signals that are suppressed by the relatively low energy of the probe beam. This leaves a symmetric carrier line that is immune to the effects of atomic recoil (see figure 4.3).

4.2.1 Recoil in Doppler-free spectroscopy

Consider the Doppler-free excitation of the two-photon transition $a \to b$. Along with exciting this atomic transition, the transfer of linear momentum to the atom can drive a concurrent change in vibrational state, $n \to n'$. This transition is described by the matrix element ${}_b\langle n'| e^{ik_{\mathrm{probe}}z} + e^{-ik_{\mathrm{probe}}z} |n\rangle_a$; where $\pm k_{\mathrm{probe}}z$ are the momentum kicks from absorption from each co-propagating beam and the subscripts indicate atomic state. Assuming magic wavelength trapping, the external potential between states a and b is identical and the subscripts can be dispensed with. The momentum kicks can be expressed in terms of the ladder operators of the harmonic potential, $\mathfrak{a}^\dagger$ and $\mathfrak{a}$, and the Lamb-Dicke parameter. This gives a

new expression of the Franck-Condon matrix elements,

$$\langle n'| e^{i\eta(\mathfrak{a}^\dagger+\mathfrak{a})} + e^{-i\eta(\mathfrak{a}^\dagger+\mathfrak{a})} |n\rangle . \tag{4.4}$$

which can be expanded as a power series in $i\eta$ as,

$$\langle n'| 2 + 0 - \eta^2(\mathfrak{a}^\dagger + \mathfrak{a})^2 + 0 + O(\eta^4) |n\rangle . \tag{4.5}$$

Assume that η is small, i.e. the Lamb-Dicke condition is fulfilled, then higher order terms are vanishingly small and, explicitly expanding $(\mathfrak{a}^\dagger + \mathfrak{a})$, one finally obtains the Franck-Condon matrix elements,

$$(2 - \eta^2(1-2n)) \langle n'|n\rangle - \eta^2(n+1)(n+2) \langle n'|n+2\rangle + \eta^2 n(n-2) \langle n'|n-2\rangle . \tag{4.6}$$

The first term relates to transitions that do not change the vibrational state of the atom, these contribute to the central carrier signal and are the only terms that survive in the limit $\eta \to 0$. Since odd powers of $i\eta$ cancel in the power series expansion of 4.4, there are no terms that contribute to first order sidebands. Instead the leading order n-changing terms relate to second order sidebands which are detuned from the carrier by $\pm 2\omega_{\mathrm{T}}$. This suppression of first-order sidebands is equivalent to the elimination of the Doppler shift in free space, whilst the remaining second-order sidebands relate to residual shifts from wavefront curvature etc.

When normalised, these Frank-Condon matrix elements give the probability amplitudes for particular vibrational transitions:

$$P_{n\to n'} = \begin{cases} \frac{1}{N}\eta^4(n+1)(n+2) & : n' = n+2 \\ 0 & : n' = n+1 \\ \frac{1}{N}(2-\eta^2-2n\eta^2)^2 & : n' = n \\ 0 & : n' = n-1 \\ \frac{1}{N}\eta^4 n(n-1) & : n' = n-2, \end{cases} \tag{4.7}$$

where N is a constant that enforces the normalisation of probabilities, $\sum_{n'} P_{n\to n'} = 1$. The Lamb-Dicke condition is relaxed from $\eta \ll 1$ for a single photon transition to $\eta^2 \ll 1$ as this mirrors the scaling of the probability amplitudes. The condition on resolved side-bands is also relaxed, requiring that $\Delta\nu_{\mathrm{FWHM}} \ll 2\nu_{\mathrm{T}}$ since only even order sidebands remain.

4.2.2 The second order Doppler shift

In the resolved side-band limit, the carrier line is, in principle, symmetric and completely immune to the effects of atomic motion. Even the residual shifts from wave-front curvature etc, that remain in free space are resolved into the side-bands. However, atoms are still in motion and measurement is subject to the effects of time dilation through the relativistic SOD shift. Following the arguments of Martinez *et. al.*[1] [114] the expectation of the fractional SOD shift on an atom in a particular vibrational state, n, is given:

$$\left\langle \frac{\delta\nu}{\nu} \right\rangle_n = -\frac{h\nu_{\mathrm{T}}}{4m_{\mathrm{H}}c^2}(2n+1). \tag{4.8}$$

As in free space, this shift does not depend upon the direction of the probe beam wave vector $\boldsymbol{k}$ and so is not cancelled in Doppler free spectroscopy.

The analogy between this shift and the free space SOD shift of section 2.3.1 is clear when one views $h\nu_{\mathrm{T}}(2n+1)/m$ as the expectation of squared velocity operator for an atom in vibrational state n, $\langle \mathfrak{v}^2 \rangle_n$. Atoms in higher vibrational states oscillate at a higher frequency[2], relating to a larger expected value of $\langle \mathfrak{v}^2 \rangle$ and so a larger SOD shift. In principle, this n-dependence splits the line into a series of sidebands detuned from the transition frequency by $(2n+1)\delta\nu_0$ (where $\delta\nu_0$ is the shift of the $n = 0$ state), as can be seen in figure 4.4. In practice, the line-width is too large to resolve these lines ($\delta\nu_0 \approx O(10)$ mHz for the 1S–2S transition in H trapped in a $D = 100$ magic wavelength lattice, much smaller than the natural line-width $\Delta\nu_{\mathrm{FWHM}} = 1.27\,\mathrm{Hz}$) and the SOD effect instead introduces a small asymmetric perturbation to the line-shape.

While pure vibrational occupation across the lattice is possible (see chapter 5), thermal occupation is far more common. The fractional SOD shift for a thermal state at temperature T can be calculated by replacing the state index in equation 4.8 with the average occupation number,

$$\bar{n} = \frac{1}{\exp\left(\frac{h\nu_{\mathrm{T}}}{k_{\mathrm{B}}T}\right) - 1}, \tag{4.9}$$

where k_{B} is the Boltzmann constant. One can express this occupation entirely in terms of the trap depth: assume a temperature that is $1/3^{\mathrm{rd}}$ of the trap depth, $T = DE_{\mathrm{rec}}/2k_B$. Combining

[1] The case of a harmonic optical trap is actually simpler than that considered in this work, and modification is straightforward.

[2] At $\omega_{\mathrm{T}}(n+1/2)$ in fact.

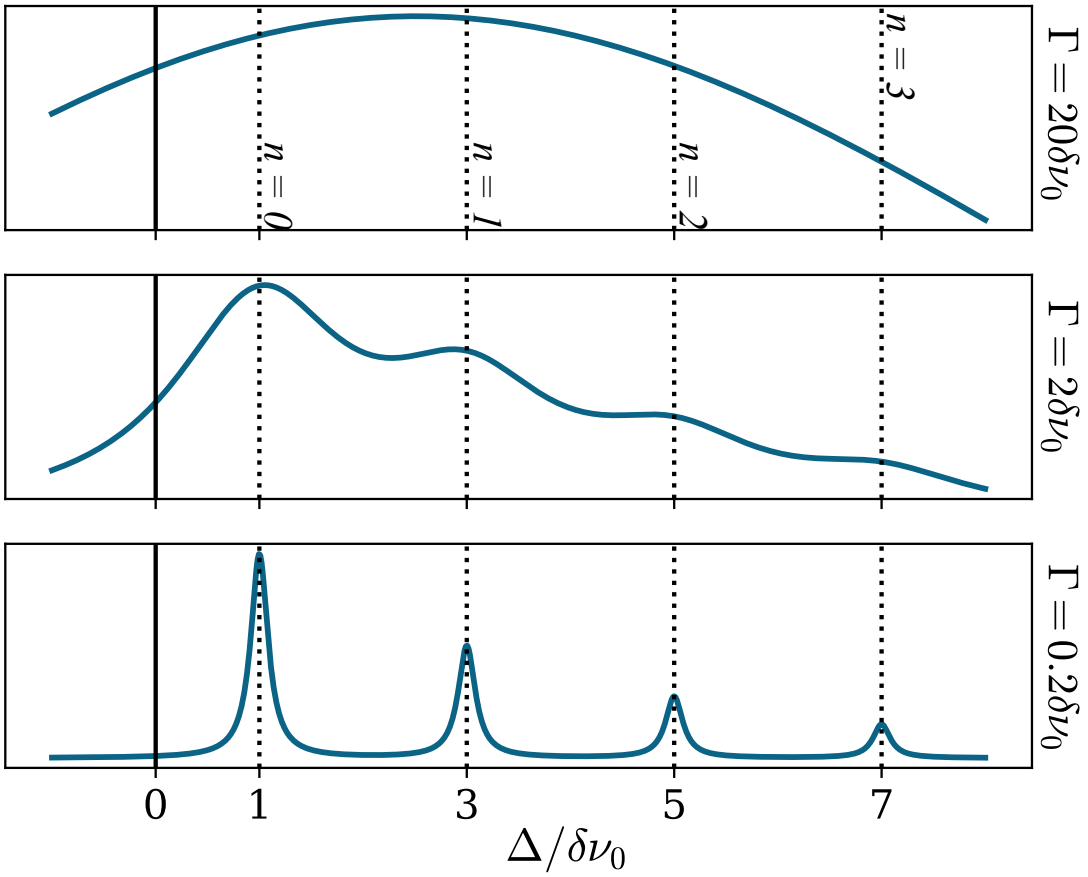

Figure 4.4: Plots of a line-shape showing the influence of the SOD shift assuming thermal occupation of vibrational states and a lattice depth of $D = 100$. Lines relating to occupation of the n=0, 1, 2, and 3 vibration states are indicated with dotted lines.

this with the definition of the trap frequency in equation 4.8, one obtains $h\nu_{\mathrm{T}}/k_B T = 6/\sqrt{D}$, this is used to define the thermal occupation of figure 4.4.

4.3 2S trap lifetimes

In free space, the 2S state is meta-stable, with a lifetime of 125 ms [115]. This state is so long lived because the only lower lying H state is the absolute ground 1S state, which has the same parity as the 2S. As such, spontaneous decay of the 2S state is forbidden by dipole selection rules, and any decay must occur by slower multi-pole interactions[1].

Since this meta-stability comes from parity constraints, it is highly sensitive to effects that mix states of opposite parity. For example, it is well known that the 2S state is susceptible

[1] In the non-relativistic structure, the $2S^{1/2}$ state is higher in energy than the $2P^{1/2}$ (due to the Lamb Shift, see section 2.2.4 and figure 2.2), the small energy difference makes for a very slow decay process.

to *quenching* (an accelerated decay to the ground state) in D.C. electric fields which can significantly shorten its lifetime [116]. The electric field mixes a small amount of P state character into the 2S state via the D.C. Stark effect, enabling spontaneous decay to the 1S state. It is well understood that A.C. fields will similarly quench the 2S state of H [1,99,100,102,117]: mixing between 2S and nP states is the source of the light-shift that is fundamental to optical trapping. It is therefore, essential to understand how the presence of a trapping field affects the lifetime of the 2S state to assess how this influences the prospect of precision spectroscopy in an optical trap.

4.3.1 Inelastic scattering

Quenching in an optical field can be thought of in terms of the off-resonant atom-photon scattering processes of section 3.1.2 (as in [102]). Clearly, elastic Rayleigh scattering does not directly affect the lifetime of the 2S state[1], so only inelastic scattering will be considered. The total inelastic scattering rate is reported per unit depth at the magic wavelengths in table 4.2, along with a breakdown of contributing processes by final nS/D state (calculated according to the method given in chapter 3). Technically, only scattering directly to the 1S state can be called "quenching", as processes with other final states are not enhanced decays to the ground state. However, the low-lying nS/D states (not including the 2S state) are short lived, decaying rapidly and preferentially to the 1S state (in cascade) . As such, they can still be thought of as additional decay channels that limit the lifetime of the 2S state and are included in this discussion. Further, table 4.2 shows that scattering to the 1S state dominates the total inelastic scattering rate out of the 2S state. This is a result of the scaling $R_{\text{in}} \sim \omega_s^3$ and the large 2S–1S energy interval compared to other transitions.

Notice that the inelastic scattering rates are particularly high; exceeding the 2S spontaneous decay rate for depths as low as $O(0.1)E_{\text{rec}}$. Scattering quickly come to dominate the lifetime of the 2S state, quenching it to $O(0.1)$ ms in a $D = 100$ magic wavelength lattice (a standard operating depth in lattice clocks of other species [110]). This is much larger than is expected for the clock states of other atoms. For example, trap-induced scattering rates are around 10^5

[1] Elastic scattering can change the momentum state of a trapped atom however, eventually leading to atom loss from the potential [93]. This heating is a major concern in other trapped atom experiments, but the low polarisability of the 1S state makes it less of a concern for H.

Table 4.2: Break down of contributions to the total inelastic scattering out of the 2S state, labelled according to final state and given as a percentage of the total rate. The total inelastic scattering rate for each magic wavelength is also reported per unit depth.

λ[nm]	1S	3S	3D	4S	4D	5S	5D	6S	6D	R_{in}/D [s^{-1}]
514.6	93.22	6.250	0.5414	-	-	-	-	-	-	61.49
443.2	90.55	4.710	0.2681	3.306	1.168	-	-	-	-	69.41
414.5	88.97	4.396	0.2124	2.560	0.7417	1.985	1.135	-	-	73.90
399.5	87.95	4.262	0.1892	2.347	0.6038	1.572	0.7956	1.309	0.9716	76.78

times smaller for the clock state of ^{88}Sr than for the 2S state of H [110]. Most of this can be put down to the poor polarisability of the 1S state (see figure 3.1) at the magic wavelengths, around 60 times smaller than the polarisability of the Sr ground state at the 813m [110]. Combined with the much larger recoil energy of H, trapping 1S H requires intensities $O(10^4)$ higher than those that trap ground state Sr-88 at the same depth. This leads to an equivalent increase in the inelastic scattering rates as $R_{\text{in}} \sim I_0$ (see equation 3.8).

The final order of magnitude is hiding in the nature of the clock-state meta-stability. As discussed, the meta-stability of the 2S state in H is founded in parity constraints and is broken by parity-mixing effects (figure 4.5 a).). The meta-stability of the Sr-88 clock state is instead supported by spin constraints and is not sensitive to parity mixing effects (see figure 4.5 b).).

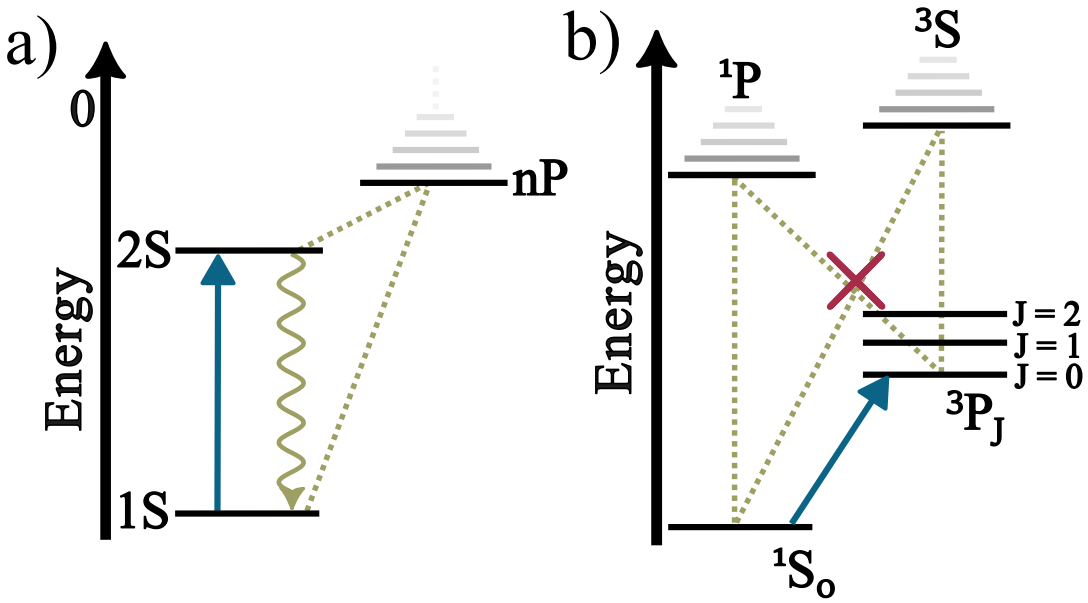

Figure 4.5: Energy level diagrams highlighting the difference between the meta-stability of the clock state in H (a) and ^{88}Sr (b). The clock transition is indicated with a blue arrow. Green lines indicate pathways for second order couplings between the clock state and the ground state.

As a result, there is a core difference between the quenching processes in H and Sr: inelastic scattering in H directly takes population from the 2S state to the ground (and other states). Whereas, in Sr it transfers population between the J states of the ^{3}P manifold which may then spontaneously decay to the ground state.

4.3.2 Two-photon ionisation

Inelastic scattering is not the only process that limits the 2S lifetime in an off-resonant optical field. Whilst not a "quenching" process in the sense previously defined, ionisation contributes a new loss channel and reduces the lifetime of the 2S state. Magic wavelength photons are not sufficiently energetic to affect single photon ionisation, which requires wavelengths shorter than 365 nm. So, to leading order, ionisation at the magic wavelengths proceeds by the simultaneous absorption of two field photons— so-called "two-photon ionisation".

Two-photon ionisation in H has long been a topic of theoretical study [103, 105, 118–121] and, like inelastic scattering, can be treated analytically through the computation of certain Schrödinger's greens functions [60, 97, 98]. Unlike inelastic scattering, high quality software for computing multi-photon ionisation rates in H is already freely available in STRFLO [105]. Calculations proceed in a very similar way to those described in chapter 3: via implicit summation across a basis of (complex) Sturmian functions. The two-photon ionisation rates calculated with STRFLO are reported in table 4.3 along with the inelastic and elastic scattering rates (calculated as per chapter 3) for comparison. Since two-photon ionisation involves the absorption of two photons from the external field, its rate scales as intensity squared[1], and so as the square of the trap depth [105]:

$$R_{\text{ion}}^{(2)} \sim I_0^2 \sim D^2. \tag{4.10}$$

For very shallow lattices, inelastic scattering is the most significant effect, but two-photon ionisation takes over at depths of around $2E_{\text{rec}}$. In deep lattices, two-photon ionisation is the dominant source of decoherence, further reducing the already quenched 2S lifetime to $O(1)$ µs in a $D = 100$ magic wavelength lattice. Such high ionisation rates are, again, a result of the

[1] This scaling holds in the perturbative treatment, at very high intensities this scaling breaks down and the calculation must be non-perturbative. STRFLO is able to do both of these and shows good agreement between the values obtained using both methods for the range of intensity covered here.

Table 4.3: Elastic and inelastic scattering rates per unit depth (D in units of E_{rec}) and the two-photon ionisation rates per unit depth squared for the four 1S–2S magic wavelengths. Also reported is the depth at which the rates of inelastic scattering and two photon ionisation are equal.

λ[nm]	$R_{\mathrm{el}}/D)$ [s^{-1}]	R_{in}/D [s^{-1}]	$R^{(2)}_{\mathrm{ion}}/D^2$ [s^{-1}]	D s.t. $R_{\mathrm{in}} = R^{(2)}_{\mathrm{ion}}$
514.6	7.986×10^{-3}	61.49	32.19	1.910
443.2	1.716×10^{-2}	69.41	30.39	2.292
414.5	2.423×10^{-2}	73.90	29.04	2.545
399.5	2.931×10^{-2}	76.78	28.33	2.710

high intensities required to trap H at the magic wavelengths. Only this time, the effect is exacerbated by the quadratic scaling of the ionisation rate. As a naturally destructive process, ionisation leads to the complete and irrecoverable loss of atoms from the lattice. Mitigating this loss at the magic wavelengths requires operating in very shallow lattices, but even then, depths smaller than $O(0.1)E_{\mathrm{rec}}$ would be required for both inelastic scattering and ionisation to be slower than spontaneous decay.

4.3.3 Non-magic trapping

It is sensible to extend consideration to non-magic wavelengths, particularly those above the two-photon ionisation threshold at 730 nm. Figure 4.6 a) shows the variation of atom-photon scattering and ionisation rates for wavelengths 395–1000 nm at constant intensity. As expected, two-photon ionisation dominates the 2S lifetime up to threshold, where inelastic scattering becomes dominant. Above the two-photon threshold, ionisation must proceed by the absorption of at least three field photons. Three-photon ionisation rates can also be calculated with STRFLO and are generally much smaller than the other plotted rates except for very narrow "2+1" resonances (where two photons drive a resonant transition to another bound state, whilst the third ionises this bound state.). Three-photon ionisation rates are not plotted below 730 nm where 2-photon ionisation dominates, or between 730 and 800 nm where a forest of 2+1 resonances would obscure the plot.

Non-magic trapping results in a differential light-shift between the two states of interest (initially considering 1S and 2S, but this does apply generically) as they are not equal in polarisability. Even though atomic motion is well constrained at the bottom of a lattice site, residual motion remains and the atom experiences a time-dependent external field intensity according

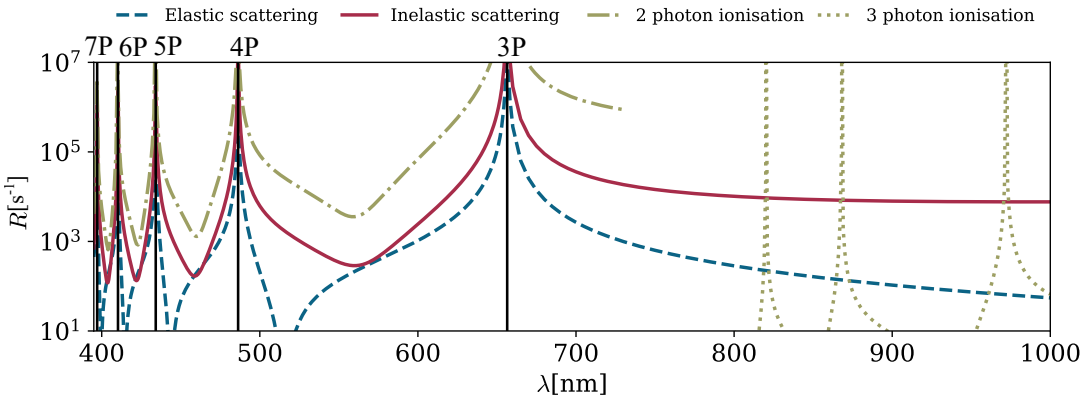

Figure 4.6: Rates of elastic scattering (dashed blue lines), inelastic scattering (solid red lines), two-photon ionisation (dash-dot green lines) and three-photon ionisation (dotted green lines) in the wavelength interval 395–1000 nm. Plot assumes a constant lattice intensity of $I = 100\,\mathrm{MWcm^{-2}}$. Two-photon ionisation rates are plotted up to threshold, whilst three-photon ionisation rates are only plotted for $\lambda > 800\,\mathrm{nm}$. Solid black lines show the 2S–nP resonances and are labelled according to nP state.

to the occupied momentum state. Combined with a differential light-shift, this introduces new systematic shifts to the measurement of the transition frequency.

4.4 Measurement limitations

The previous discussion highlights both the strong motivations for a 1S–2S lattice clock, and some serious departures from existing OLCs. In particular, the lifetime of the clock (2S) state is severely reduced by effects inherent to the trapping field at the required intensities. It is essential to understand how these effects limit the measurement potential of the proposed clock and to compare this to the state of the art beam experiments.

4.4.1 Effective limits on clock line-widths

As seen in section 4.3, the lifetime τ of the atomic transition fundamentally limits the FWHM of the observed spectral line, $\Delta\nu_{\mathrm{FWHM}} > 1/(2\pi\tau)$. Since the 1S state is the absolute ground state and is therefore stable, the lifetime of the transition is entirely given by the lifetime of the 2S state. As discussed in section 4.3, this is unavoidably reduced in the high intensity external fields needed to trap in the 1S state. So the minimal line-width is also broadened according to the trap depth D.

Table 4.4: Complete limits on a 1S–2S H lattice clock operating in the Lamb-Dicke regime according to magic wavelength. The first column gives the trap frequency per unit square root of the lattice depth. The second column gives the depth D_{LD} that ensures $P_{n=0\to n=0} = 0.9$, equivalent to $\eta^2 = 0.381$. The next columns give the intensity required to achieve this depth, the associated minimal 1S–2S line-width, and the ratio $\nu_{\mathrm{T}}/\Delta\nu_{\mathrm{FWHM}}$. The final column gives the expected fractional SOD shift assuming thermal occupation of the vibrational states.

λ[nm]	$\nu_{\mathrm{T}}/\sqrt{D}$[MHz]	$D_{\mathrm{LD}}/E_{\mathrm{rec}}$	I[MWcm^{-2}]	$\Delta\nu_{\mathrm{FWHM}}$[kHz]	$\nu_{\mathrm{T}}/\Delta\nu_{\mathrm{FWHM}}$	$\langle\delta\hat{\nu}/\nu\rangle_{\mathrm{SOD}}$
514.6	1.50	34.5	116	6.43	1370	-2.06×10^{-17}
443.2	2.02	19.0	84.9	1.95	4520	-1.62×10^{-17}
414.5	2.31	14.5	73.3	1.14	7720	-1.48×10^{-17}
399.5	2.48	12.5	67.7	0.857	10300	-1.40×10^{-17}

To make a quantitative statement on the broadening that could be expected in a practical clock, I demand that the probability of remaining in the vibrational ground state is at least 90%, i.e. $P_{n=0\to n=0} \geq 0.9$. This is enforced by requiring the Lamb-Dicke parameter of $\eta^2 \leq 0.381$, which is the case for trap frequencies of $\nu_{\mathrm{T}} = 8.79\,\mathrm{MHz}$ and above. Table 4.4 reports the minimal depth that fulfills this condition — the so-called "minimal Lamb Dicke depth" D_{LD}— at each magic wavelength, along with the intensity required to produce it. Constraining the lattice depth in this way allows me to obtain a lower bound on the transition line-width, set by two-photon ionisation and also reported in table 4.4. These values of $\Delta\nu_{\mathrm{FWHM}}$ are much smaller than the trap frequency, indicating side-bands that are detuned from the carrier by many ($O(10^3$–$10^4)$) times the line-width (see table 4.4) — *deep* in the resolved side-band limit. Finally, the table also provides the expected fractional SOD shift to the 1S–2S transition frequency, assuming thermal occupation of these lattices. These shifts are very small, $O(10^{-17})$, or $O(10)\,\mathrm{mHz}$, which is well below the current measurement precision.

Narrower lines are possible for shorter wavelengths, e.g. 0.857 kHz at 399.5 nm compared to 6.43 kHz at 514.6 nm. This can be understood through the tighter confinement offered by these lattices, resulting in larger trap frequencies for a given depth. For example, a 514.6 nm lattice must be at least $34.5E_{\mathrm{rec}}$ deep to achieve $\eta^2 \leq 0.381$, whilst a 399.5 nm lattice only needs to be deeper than $12.5E_{\mathrm{rec}}$. A shallower lattice naturally reduces the two-photon ionisation rate and relives some of the broadening. Additionally, it should be noted that the two-photon ionisation rate per unit depth squared (as given in table 4.4) also slowly decreases with wavelength, and this plays a small part in the above observation.

These results clearly show that effective control of velocity dependent systematics (through well

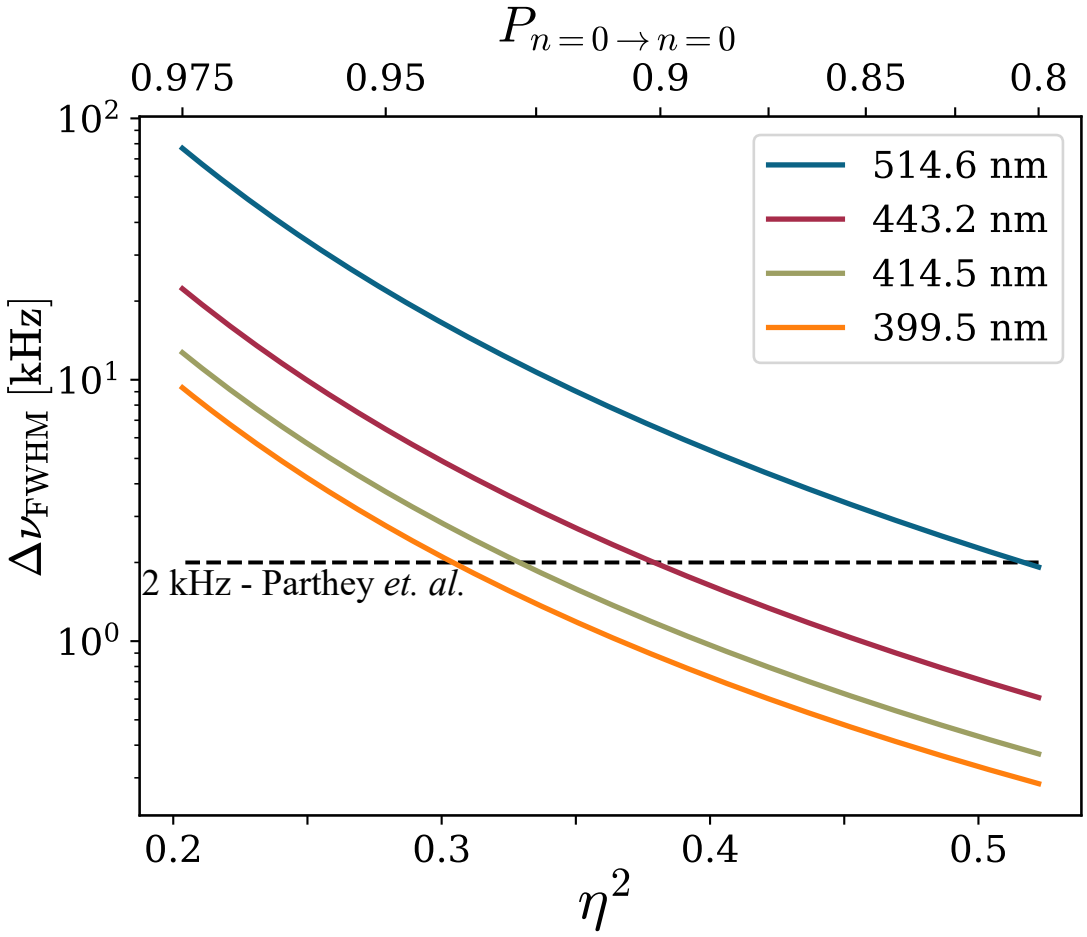

Figure 4.7: The 1S–2S minimal line-width in each of the four magic wavelengths with the Lamb Dicke coefficient η^2. The top x-axis shows how this relates to the probability of remaining in the ground vibrational state under 1S–2S excitation. Also shown, with a dotted line, is the 2 kHz level set by the atomic beam measurement [20].

resolved side-bands, operating within the Lamb-Dicke regime, and constraining the SOD shift) can be achieved in much shallower lattices than is usual in other species, e.g. Sr-88 [45]. This is a direct result of the low mass of H and correspondingly high trap frequencies. Operating in shallower traps mitigates the broadening effects of two-photon ionisation and allows for minimal line-widths $O(1)$ kHz. Even narrower lines can be achieved if one is willing to relax the Lamb-Dicke condition (see figure 4.7). Provided that the resolved side-band limit is maintained (which is assured at these depths) being deep in the Lamb-Dicke regime is not essential to a precision measurement. In practice, minimal line-widths of $O(100)$ Hz are probably the best that could be expected before lattices become too shallow to offer proper confinement.

4.4.2 Comparison with beam measurements

It is instructive to compare this clock to the best 1S–2S measurements in cold beams [20, 28]. The uncertainty in these beam measurements is dominated both by statistical uncertainty and by motional systematics arising from the SOD effect. Careful velocity filtering minimises this effect to an extent, and results in an asymmetric line-shape that depends heavily upon the detailed properties of the velocity distribution. Fitting with a complex line-shape model allows for a final measured width of $\sim 2\,\mathrm{kHz}$ [20]. In the 1S–2S clock described above, most of the effects of atomic motion are resolved into identifiable side-band signals, leaving a generally symmetric carrier signal. Compared to atomic beams, trapped atom experiments benefit from long measurement times and narrow line-widths. Two-photon ionisation at the magic wavelengths, however, limits the 2S lifetime and erodes this advantage. While minimal line-widths of $O(100)\,\mathrm{Hz}$ could be achieved at short magic wavelengths by relaxing the Lamb-Dicke constraints (see figure 4.7), this is only around one order of magnitude lower than the $2\,\mathrm{kHz}$ width observed in beams.

Longer measurement times come at the cost of reduced statistical power, limited by the slow repetition rates and low atom numbers associated with cold, trapped samples. In Sr OLCs, statistical power is improved by driving a fast-cycling transition out of the ground state. The absorption on this transition provides a long time measurement of the ground state population with a very high signal to noise ratio [45]. The clock transition is then identified by a drop in the ground state population, and each measurement of the clock transition is supported by a large number of observed events [45]. Unfortunately, in H all suitable transitions out of the ground state lie at Lyman series wavelengths. The lack of laser power in the far-VUV region of the spectrum [122] makes mimicking this scheme impractical. While trap-induced ionisation will provide a background-free readout, it is limited to only one event per 1S–2S transition.

It is impossible to begin to estimate the statistical uncertainty associated with a clock without a complete experimental proposal. This is because the final statistical power of a measurement will depend critically on technical quantities such as the duty cycle, the final temperature, and read-out mechanism. Cooling and loading H into optical traps is currently and open problem, and will be discussed in chapter 5. But, it is clear that optimising the experimental cycle and

achieving efficient read-out will be crucial to minimising the statistical uncertainty of trapped atom experiments.

It is clear that this H lattice clock will not be competitive with state of the art atomic/ion clocks [50, 123, 124] as an absolute frequency reference. However, such a clock offers a *new* measurement of the 1S–2S transition in H that is effectively free from the velocity dependent systematics that *may* be at the heart of the proton charge radius puzzle (see section 2.3.3). Comparisons between the well established beam measurement and this new measurement will act as a litmus test for unidentified systematic shifts. Further, since the 1S–2S transition is so central to the H dataset, it is highly desirable to repeat this measurement in a new system. The same results apply to clocks of D and $\bar{\text{H}}$ — in fact, an $\bar{\text{H}}$ 1S–2S lattice clock has already been proposed for improved precision given the small number of available anti-atoms [51]. Comparative measurements of the 1S–2S transition in H, D and $\bar{\text{H}}$ are critical to modern tests of fundamental physics (see chapter 2 and [38, 40, 52–55]). These improved systematics seem to come at the cost of worse statistics, but it remains to be seen whether this can be remedied by efficient readout and loading schemes.

4.4.3 Implications for other transitions

The implications of these results extend to the potential measurements of other H frequency intervals; particularly to those involving high-lying Rydberg states, where the positional certainty provided by a lattice (or ideally tweezer array) is essential to control dipole interaction systematics. While usable magic wavelengths for these transitions are unlikely, there are a number of methods that can be employed to counter the effects of non-magic trapping in these measurements; the most simple of which is to turn off the trap and perform the measurement in a shorter time at high Rabi frequency [125]. Consider specifically the case of a 2S-Rydberg transition.

These transitions do not require deep trapping in the 1S state, so one can trap with much lower intensities by choosing a wavelength with large 2S polarisability (see figure 3.1). Away from the points where α_{2S} changes sign (and naturally polarisability is very small), there is a significant decrease in the rates of multi-photon ionisation and inelastic scattering for a given 2S lattice depth, as plotted in figure 4.8. Note that this range of wavelengths extends over regions of

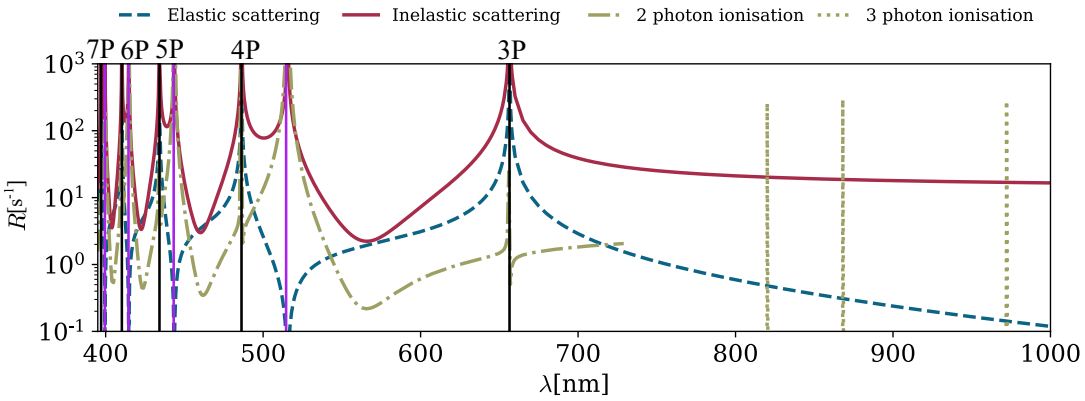

Figure 4.8: Rates of elastic scattering (dashed blue lines), inelastic scattering (solid red lines), two-photon ionisation (dash-dot green lines) and three-photon ionisation (dotted green lines) in the wavelength interval 395–1000 nm. Plot assumes a constant 2S lattice depth of $D = 10$. Two-photon ionisation rates are plotted up to threshold, whilst three-photon ionisation rates are only plotted for $\lambda > 800$ nm. Solid black lines show the 2S–nP resonances and are labelled according to nP state. 1S–2S magic wavelengths are denoted by vertical lines in purple.

both red and blue detuning for the 2S state, affecting whether the atom will be trapped at the node or the anti-node of the standing wave respectively. The calculation ignores the sign of the potential when calculating the depth, so actual loss rates observed in blue detuned traps may be lower than reported. Regardless, using a non-magic wavelength enables deep trapping with longer 2S lifetimes.

Even then, the lifetime of the 2S state is unlikely to dominate the line-width of the transition compared to the shorter lifetimes of the other states. Take a 1000 nm lattice as an example: the 2S lifetime is dominated by inelastic scattering which only quenches it to ~ 6 ms at a trap depth of $D = 100$. This lifetime is generally larger than the lifetimes of these H Rydberg states: at $n = 30$, states with low-l have lifetimes $O(10)$ µs, while states with high-l can have lifetimes of 100's µs [126, 127]. In this case the line-width is dominated by the lifetime of the Rydberg state and the achievable measurement time, quenching only serves to limit the achievable initial 2S population. Ultimately, the main concern for these measurements will be avoiding issues related to differential light shifts and stray electric fields whilst maintaining tight confinement and well defined separation.

Chapter 5

ULTRA-COLD, TRAPPED HYDROGEN

Chapter 4 concerned the spectroscopy of H confined in an optical lattice with no more than one atom per site in low-lying momentum states, mirroring those of modern OLCs [45]. This system provides the tight control of motional systematics that are essential to a new 1S–2S measurement and the well-defined inter-atomic spacing required for precision Rydberg spectroscopy. The natural next step is to consider how one might produce such a system. This is a question both of cooling H and loading it into tightly confining optical traps. As it turns out, this is not a trivial matter and has been a barrier to progress for some time.

Usually, optical tools such as magneto-optical traps and optical molasses are used to cool atoms and load optical lattices/tweezers [9, 128]. However, these processes are severely limited for H by the lack of laser power available for Lyman series wavelengths: continuous wave (CW) beams at 121 nm are limited to powers of only $\sim 10\,\mathrm{nW}$ [129, 130], whilst pulsed lasers suffer from short pulses and slow repetition rates [122]. Almost 30 years separate the first report of laser cooled H [131] and the recent laser cooling of $\bar{\mathrm{H}}$ [74], yet little progress in the output power can be seen[2]. Attempts to mimic the meta-stable state cooling of helium [132, 133] are hampered by unfavourable branching ratios and slow re-pumping rates: 30 W of cw 243 nm light can expect to give a 1S–2S scattering rate of only $\sim 1\,\mathrm{kHz}$ [134].

Deprived of the standard techniques, attention has turned to a variety of novel approaches for producing ultra-cold, trapped H — some more successful than others. Two approaches are worth special mention: First is the possible threshold dissociation of a laser cooled alkaline-earth hydride as described in [56]. The group of T. Zelevinksy has already demonstrated laser cooling of CaH and CaD molecules towards this goal [135, 136]. Second, it might be possible to leverage the induced decay of the 2S state to load an optical dipole trap in the 1S. The group

[2]Pulsed Lyman-α lasers were used in each case with comparable pulse lengths. Whilst the 2021 laser had a lower duty cycle, it had on average around 10 to 100 times more photons per pulse and was solid sate rather than dye based. The much longer cooling times for $\bar{\mathrm{H}}$ vs H can be put down to the very low anti-atom densities available.

of T. Udem is currently working on an implementation of this using a velocity selected atomic beam [70].

Despite this recent progress, there remains only one experimentally proven route to ultra-cold H: the evaporative cooling approach that led to BEC in 1998 [57].

5.1 A Bose Einstein Condensate of Hydrogen

The BEC of H came only three years after the first observation of BECs in dilute alkali vapors in 1995 [137–139]. The full details of this experiment can be found in the original report [57] and associated thesis [140]. However, it is useful to give a brief overview of the procedure here:

- First, cold H atoms are produced by RF dissociation of H_2 molecules at $\sim 1\,\mathrm{K}$. These atoms flow into a cell with a superimposed 550 mK deep Ioffe-Pritchard type magnetic trap.
- Hot atoms are cooled by contact with the walls of the cell, which are held at 275 mK by cryogenics. A film of super fluid ^{4}He on the walls reduces contact time and prevents recombination.
- The gas of H thermalises via inter-atomic collisions, cold atoms may become trapped whilst hot atoms go on to re-collide with the cold walls. State selective trapping ensures that the remaining atomic gas is spin polarised.
- The trapped atoms are cooled to 120 µK by evaporation over a saddle-point at one end of the trap. Ejected atoms are thermally isolated from the trapped atoms by sticky collisions with the cell walls (now at 150 mK).
- Past 120 µK, atoms settle into the harmonic region of the trap and high energy trajectories have long escape times. The sample is further cooled by forced evaporation with an RF-knife, reaching temperatures as low as 20 µK.

The onset of BEC was observed at a temperature of 50 µK for densities of $1.8 \times 10^{14}\,\mathrm{cm}^{-3}$. Ultimately, the experiment produced a condensate of 10^9 H atoms, with a peak density of $4.8\pm$

$1.1 \times 10^{15}\,\mathrm{cm}^{-3}$. The high condensate densities can be understood in light of the anomalously small S-wave scattering length of H: taken as[1] $a_\mathrm{s} = 0.721\,\text{Å}$ [145].

Despite the unusually high number of condensed atoms, the condensate fraction (the ratio of atoms in the condensate compared to those available for condensation) is surprisingly small: estimated as $< 7\%$ [57]. The high condensate density drastically increases the rate of dipolar relaxation (spin relaxation to un-trapped states due to the interaction between atomic magnetic dipoles, see [140] for a full discussion), which becomes the dominant loss channel. The condensate is constantly replenished by cooling in the surrounding thermal cloud, which is ultimately limited by the slow rate of rethermalising collisions in the gas (since a_s is so small). The condensate fraction is a reflection of an equilibrium between these two competing processes that favours smaller condensates.

Since this experiment, the study of BECs in H has not progressed and the results have never been replicated. A major reason for this is the technical complexity of the experiment, especially compared to the requirements of alkali BECs — which have seen continual study and development. In the past 25 years, there has been significant progress on techniques for producing and manipulating alkali BECs which could be applied to improve the situation in H. For example, a condensate formed in an entirely optical trap (as demonstrated in [146]) in the absolute ground state is no longer susceptible to dipolar relaxation; and condensation through the manipulation of trap geometry (see e.g. [147, 148]) may go some way to alleviating the reliance on a slow evaporation rate. Combined with the rapid advance in cryogenic technology in recent years (e.g. commercially available dilution refrigerators from companies such as BlueFors and Oxford Instruments) the prospect of a new H BEC experiment becomes all the more promising. In fact, new cryogenic realisations of ultra-cold H have already been applied to the study of magnons [149], and the Grassian collaboration is progressing towards a new ultra-cold H experiment [150].

Clearly, the capacity is there for a modernised experiment, it simply needs sufficiently strong motivation.

[1] Specifically the triplet scattering length which dominates over the singlet. The exact value of this scattering length is dependent upon choice of scattering potential, see [141, 142] and the references therein, but 0.721 Å is chosen as an accepted middle ground. Also, note that this length is isotope dependent, see [143, 144].

5.1.1 Suitability for spectroscopy

While a BEC is, in many ways, the ultimate limit of an ultra-cold sample, it is not an appropriate sample for precision spectroscopy. Resonances are subject to significant shifts and broadening due to inter-atomic interactions. Indeed, the major changes to the 1S–2S line under Doppler-free spectroscopy were a key way of experimentally identifying the presence of a condensate [57, 140].

This is not the end of the story, as a BEC is a vital stage in the production of the highly ordered lattice systems used in quantum gas microscopes [151]. These experiments leverage the many-body dynamics of an interacting Bose gas in a lattice to drive the transition to a MI phase — characterised by uniform occupation of highly localised atoms in the ground vibrational state. MIs of Bosonic alkali atoms are routinely produced [151, 152]. If such a phase could be produced in H, it would seem ideal for the 1S–2S lattice clock and precision spectroscopy discussed in chapter 4.

The properties of H are notably different to the heavier alkali atoms, and it is not immediately clear that a process which is usual in atoms like Rb or caesium will be feasible for H (take laser cooling for example). It is therefore the goal of this chapter to try to identify a route to H MI, and to examine its implications for precision spectroscopy.

5.2 The super fluid to Mott insulator transition

I begin with the many body physics of a degenerate Bose gas in an optical lattice. Consider the simple 3D lattice potential with wave-vector $\boldsymbol{k} = k_x\hat{\boldsymbol{x}} + k_y\hat{\boldsymbol{y}} + k_z\hat{\boldsymbol{z}}$, parameterised by the unit-less depth D,

$$V_{\text{latt}} = DE_{\text{rec}}\left(\sin^2(k_x x) + \sin^2(k_y y) + \sin^2(k_z z)\right). \tag{5.1}$$

The spacing between nearest neighbour lattice sites is given by the lattice constant $a = \lambda/2 = \pi/|\boldsymbol{k}|$.

The solutions to the single particle Schrödinger equation are conveniently given in terms of a

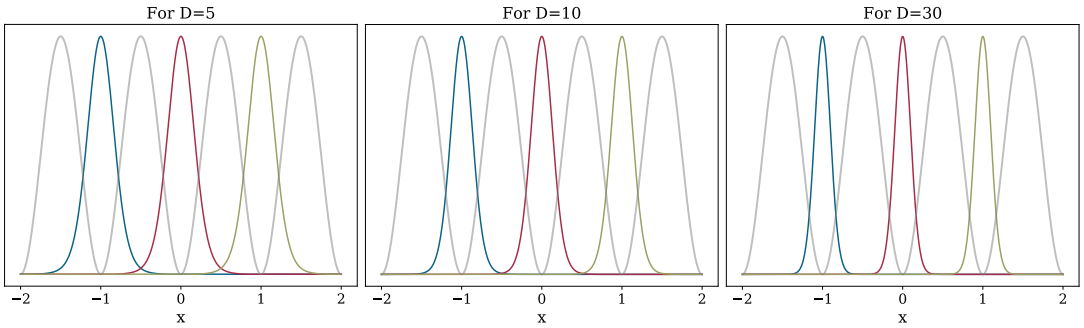

Figure 5.1: Illustrative plots of the Wannier functions in a 514.6 nm optical lattice along a single axis. Three functions localised to adjacent sites along x (in units of a) are plotted at three different lattice depths and are differentiated with colour. These plots were generated with numerical Wannier functions according to appendix C. The grey line indicates the lattice potential with no meaning to its height.

set of Wannier functions (see, e.g. [153]),

$$w_n(\boldsymbol{r} - \boldsymbol{R}_j) = \frac{1}{\mathcal{V}} \int_{\mathrm{BZ}} d\boldsymbol{q} e^{-i\boldsymbol{R}_j \cdot \boldsymbol{q}} \phi_{n,\boldsymbol{q}}(\boldsymbol{r}), \tag{5.2}$$

where $\phi_{n,\boldsymbol{q}}$ is the n-th band Bloch function with quaismomentum $\boldsymbol{q}$, $\boldsymbol{R}_j$ is spatial coordinate of the local minimum in lattice site j, and $\mathcal{V}$ is the volume of the first Brillouin zone (BZ). Each Wannier function is centred on the potential minima of a given lattice site and is local to that site (see figure 5.1) — as opposed to the delocalised Bloch functions which extend across the whole lattice. In the case of a *degenerate* Bose gas, only the lowest Bloch band is relevant. As such, I take $n = 0$ and neglect this index going forwards.

5.2.1 The Bose Hubbard Model

One can now begin to think of each lattice site in isolation, with its own local potential and occupation (number of atoms in the local potential) — given for site j in terms of the number operator $\mathfrak{s}_j$ (the occupation of site j is the eigenvalue of this operator[1], s_j). This occupation is not necessarily static and atoms may tunnel or "hop" from between sites i and j according to the application of the relevant creation and annihilation operators ($\mathfrak{a}_j^\dagger$ and $\mathfrak{a}_j$ respectively for site j): $-J\mathfrak{a}_j^\dagger \mathfrak{a}_i$, where the tunnelling potential[2] is given [152, 154],

$$J = \int d\boldsymbol{r} w^*(\boldsymbol{r} - \boldsymbol{R}_j) \left[\frac{-\hbar^2}{2m} \nabla^2 + V_{\mathrm{latt}}(\boldsymbol{r}) \right] w(\boldsymbol{r} - \boldsymbol{R}_i). \tag{5.3}$$

[1] Usually, $\mathfrak{n}_j$ and n_j would denote this operator and the site occupation. In this thesis, n is already used extensively in other contexts so cannot be used here.

[2] Here, I call this J in line with [154]. It is worth noting that t is also a common in other works, e.g. [155,156].

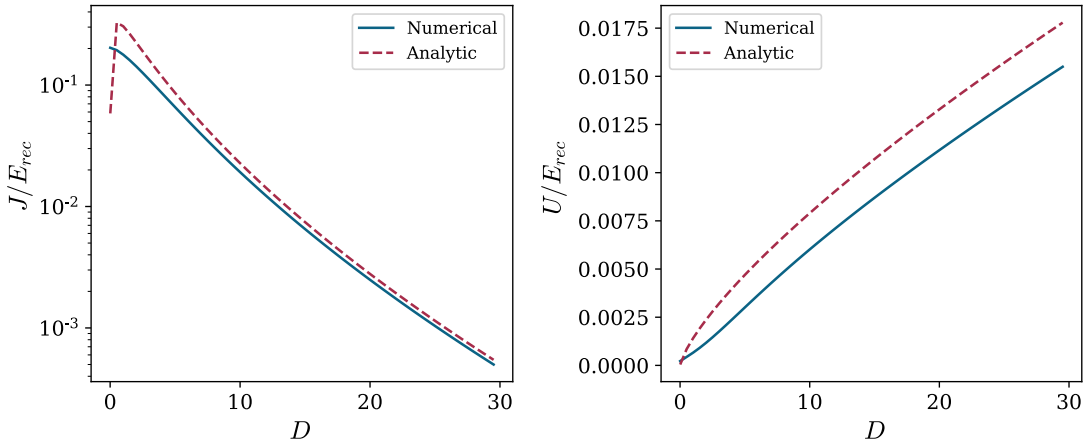

Figure 5.2: A comparison between numerical(red dashed lines) and analytic (blue solid lines) values of J and U. In both cases, J and U are calculated for varying depths per unit recoil in a 514.6 nm optical lattice (as in equation 5.1).

In the low energy regime implied by a degenerate Bose gas, it is appropriate to restrict consideration to hopping between pairs of nearest neighbour sites only [154].

Atoms occupying the same lattice site interact according to the potential [152, 154],

$$U = \frac{4\pi\hbar^2 a_s}{m} \int d\boldsymbol{r} |w(\boldsymbol{r})|^4, \tag{5.4}$$

where a_S is the S-wave scattering length as discussed above. In principle, these interaction can be attractive or repulsive. I will consider only the repulsive case which includes H.

The potentials J and U can be computed numerically, as described in appendix C, or by approximating the Wannier functions as Gaussian (appropriate in sufficiently deep lattices) to obtain analytic expressions [157]:

$$\frac{J}{E_\mathrm{rec}} \approx \frac{4}{\sqrt{\pi}} D^{\frac{3}{4}} \exp\left(-2\sqrt{D}\right) \text{ and } \frac{U}{E_\mathrm{rec}} \approx \sqrt{\frac{8}{\pi}} k a_\mathrm{s} D^{\frac{3}{4}}. \tag{5.5}$$

A comparison between these two approaches is given in figure 5.2 which shows reasonable agreement for all but the most shallow lattices. Whilst the numerical approach is generally favoured in calculations, the scaling laws above are useful for understanding results.

These effects are united in the *Bose-Hubbard Hamiltonian* [154, 157],

$$\mathfrak{H}_\mathrm{BH} = -J \sum_{i \neq j} \mathfrak{a}_j^\dagger \mathfrak{a}_i + \frac{U}{2} \sum_i \mathfrak{s}_i(\mathfrak{s}_i - 1) - \mu \sum_i \mathfrak{s}_i. \tag{5.6}$$

where the final term ensures conservation of total atom number over the whole lattice via the chemical potential μ. This Hamiltonian describes the many-body dynamics of a degenerate Bose gas in the lattice $V_\mathrm{latt}(\boldsymbol{r})$.

5.2.2 Bose Hubbard ground states

Ground states of the Bose-Hubbard Hamiltonian (equation 5.6) can be found in two limiting cases: first, in the limit $U/J \to 0$, hopping dominates the many-body dynamics and atoms are delocalised across many lattice sites. This is called the SF phase and is characterised by maximum variance in occupation and minimal variance in quantum phase [154, 157]. In the opposing limit, $J/U \to 0$, hopping is suppressed and atoms are localised to particular lattice sites. Minimising energy given the large penalty for multiple occupation enforces a uniform filling $\bar{s}$ across the whole lattice. When there are an integer number of atoms per lattice site, i.e. $\bar{s} \in \mathbb{N}$ (commensurate filling) one obtains a MI which shows minimal variance in occupation and maximum variance in quantum phase [154, 157]. When atom and lattice numbers do not exactly divide (incommensurate filling), the MI is perturbed by an additional SF phase which pervades the entire lattice [157].

The ideas of commensurate/incommensurate filling rest on an infinite, uniform lattice potential. In a real system, the lattice is bounded according to some external potential $V_{\text{ext}}(\boldsymbol{r})$, which confines the gas to a finite region of space and breaks the homogeneity of the system. The effect of this potential is accounted for in the Bose-Hubbard model by the introduction of a local chemical potential (see e.g. [154, 157]),

$$\mu_j = \mu - V_{\text{ext}}(\boldsymbol{R}_j), \tag{5.7}$$

which gives a spatially varying phase. In the $J/U \to 0$ limit, the system is divided into regions of MI phase with a local filling given according to the local chemical potential [154, 157],

$$\bar{s}_j = \text{Mod}_{\mathbb{N}}\left(\frac{\mu_j}{U}\right). \tag{5.8}$$

Henceforth, I will assume that the external potential is harmonic, with a geometric average trap frequency ω_{T}. The maximum chemical potential is then given [158],

$$\mu = \left(\frac{15}{16}\frac{a^3 N U m^{3/2}\omega_{\text{T}}^3}{\sqrt{2}\pi}\right)^{2/5}, \tag{5.9}$$

in terms of the total atom number N. An external potential of this kind results in the "wedding cake" structure of MI phases shown in figure 5.3 (a).

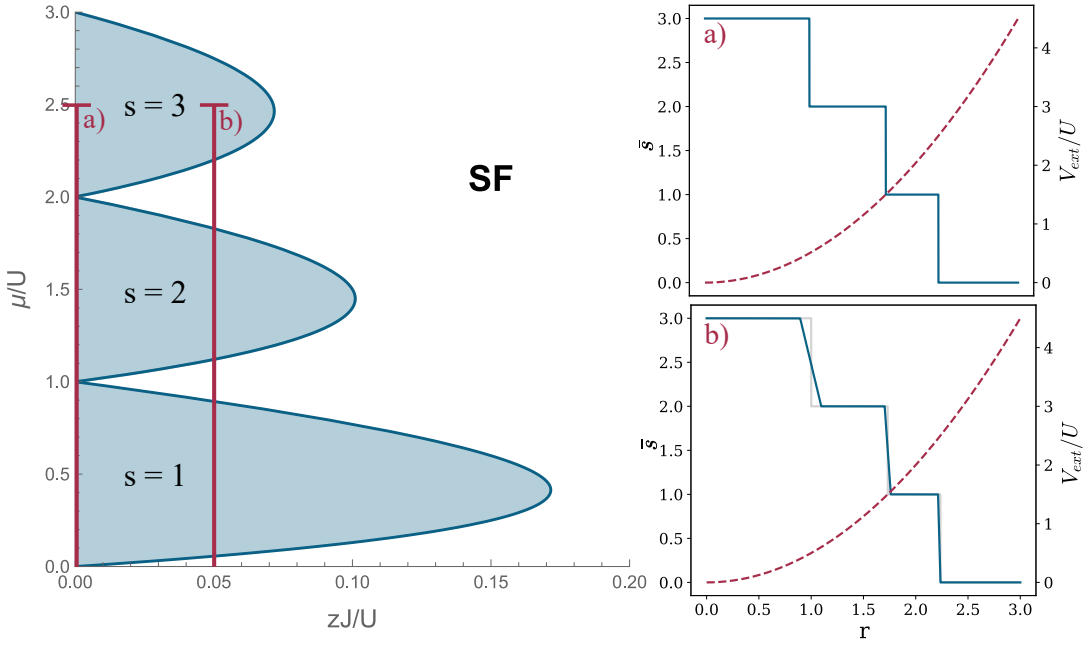

Figure 5.3: The mean field theory phase diagram showing the ground states of the Bose Hubbard Hamiltonian. The MI phases are labelled according to filling. The red lines a) and b) show the range in phase space covered by a harmonically varying local chemical potential with $\mu = 2.5U$ at the centre for two values of J/U. The radial variation of average site filling is shown by the blue line in the accompanying inserts, while the red line shows the external potential.

5.2.3 The phase transition

One can pass between the SF and MI phases by smoothly varying the ratio U/J from one limit to the other. Whilst the phase transition cannot be treated exactly, a mean field theory treatment can be applied to produce the phase diagram (figure 5.3) and to estimate a critical point [154, 157]:

$$\left(\frac{U}{J}\right)_{\text{crit}} = \begin{cases} 5.8z & : \bar{s} = 1 \\ 4\bar{n}z & : \bar{s} >> 1. \end{cases} \tag{5.10}$$

Here, z denotes the number of nearest neighbours to each lattice site, 6 for V_{latt} of equation 5.1.

This transition is central to the production of MIs for use in quantum gas microscopes. The first step is to produce a BEC of the chosen species and confine it to a shallow lattice. The degenerate gas naturally occupies the many-body ground state and realises the SF phase [154]. Since $U/J \sim e^{2\sqrt{D}}$, changing the lattice depth D provides control[1] of the all important ratio

[1]Note that this ratio can also be controlled by varying the scattering length a_s via Feshbach resonances.

U/J. By smoothly ramping up the lattice depth, one can (reversibly) drive the transition to the MI phase (see [152, 157, 159]).

Driving the SF–MI phase transition requires that the system remains in the ground state throughout the ramping process — that it is *adiabatic*. Achieving this in finite time depends on fulfilling the adiabatic criteria,

$$\hbar|\dot{\mathfrak{H}}_{\mathrm{BH}}| << \Delta E^2. \tag{5.11}$$

Both U and μ vary slowly with D, so the exponentially varying J comes to dominate the rate of change of the Hamiltonian. Remaining adiabatic in the SF phase requires that tunnelling is fast enough for the gas to follow the Thomas Fermi ground state. In this case the energy gap is given by the tunneling potential, $\Delta E \approx J$ [160]. The adiabatic condition can then be written:

$$\frac{\hbar|\dot{J}|}{J^2} << 1, \tag{5.12}$$

which demonstrates good agreement with experimental results [160]. Working in the Gaussian approximations of equation 5.5, one can produce a condition on the ramping rate $\dot{D}$:

$$\hbar\dot{D} << \frac{16D^{7/4}}{\sqrt{\pi}\hbar\left|3-4\sqrt{D}\right|}e^{-2\sqrt{D}}E_{\mathrm{rec}} = f(D)E_{\mathrm{rec}}, \tag{5.13}$$

where $f(D)$ is some function that depends entirely upon depth[1].

Previous discussions of the MI phase have assumed that all tunnelling between lattice sites ceases, $J \to 0$. This condition is achieved only when $D \to \infty$, which is physically unreasonable (and relates to $U \to \infty$). For the finite depths of real experiments, there is some residual hopping that blurs the boundary between MI states, see figure 5.3 (b). To leading order in zJ/U, the MI lobe of filling $\bar{n} > 1$ is then bounded in phase space by the conditions [155, 156]:

$$\frac{\mu}{U} < \bar{s}\left(1-\frac{zJ}{U}\right) \text{ and } \frac{\mu}{U} > (\bar{s}-1)\left(1+\frac{zJ}{U}\right). \tag{5.14}$$

The $\bar{s}=1$ lobe is bounded above as $(1-zJ/U)$ and below as zJ/U. These conditions can be used to predict the phase and filling of any lattice site for a given final depth D.

[1] This is an approximate condition that will be suitable for my later purposes. A more detailed approach can be found in [161].

Table 5.1: Critical lattice depths for the SF–MI phase transition in atomic hydrogen at listed wavelengths. Calculations use the mean-field critical point (equation 5.10) and assume filling of $\bar{s} = 1$. Values reported are numerical with analytic approximations in brackets.

λ[nm]	1064	514.6	443.2	414.5	399.5
$D_{\mathrm{crit}}/E_{\mathrm{rec}}$	34.2(34.0)	30.1(29.9)	29.3(29.1)	29.0(28.7)	28.8(28.5)

5.3 Mott insulators of hydrogen

It is now time to apply the above understanding specifically to a degenerate gas of H. The first task is to estimate the lattice depth related to the critical ratio of equation 5.10 at $\bar{s} = 1$, call this D_{crit}. This can be done numerically as described in appendix C, or (expecting D_{crit} to be sufficiently large) approximately with the expression:

$$D_{\mathrm{crit}} = \frac{1}{4}\left[\ln\left(\frac{\sqrt{2}a}{\pi a_s}\left(\frac{U}{J}\right)_{\mathrm{crit}}\right)\right]^2. \tag{5.15}$$

Table 5.1 reports values of D_{crit} at each of the H 1S–2S magic wavelengths (see chapter 4) and 1064 nm. Both numerical and approximate values are presented and show good agreement, as would be expected for deep traps. The variation of this depth with λ can be understood in the context of equation 5.15, which shows $D_{\mathrm{crit}} \sim (\ln(\lambda))^2$. These critical depths are notably larger than is usual in Rb, which only require depths of around $13E_{\mathrm{rec}}$ [151, 152, 159]. This can be put down to the small S-wave scattering length of H which leads to smaller values of U.

Calculating a time-scale for the transition involves enforcing this condition on a known ramping profile — usually with some "S" shape to prevent sharp changes at the start and end. For now, it is sufficient to estimate time-scales via comparison with other atoms. Consider Rb; it is routine to drive the SF–MI transition in a 1064 nm lattice over times $O(100)$ ms [152, 158–160]. The recoil energy for H in a 514.6 nm lattice is around 350 times larger than for Rb in the 1064 nm lattice. Since $\dot{D}_{\mathrm{max}} \sim E_{\mathrm{rec}}$, the ramping may be around 350 times faster in the H system than the Rb system whilst still being adiabatic. Even given the larger critical depth, one can still expect to drive the SF–MI transition in time scales of $O(1\text{–}10)$ ms.

5.3.1 Controlling filling fractions

A key requirement for the measurements discussed in chapter 4 is a maximum of one atom per lattice site only which eliminates uncertainty due to the on-site interaction shift. I have

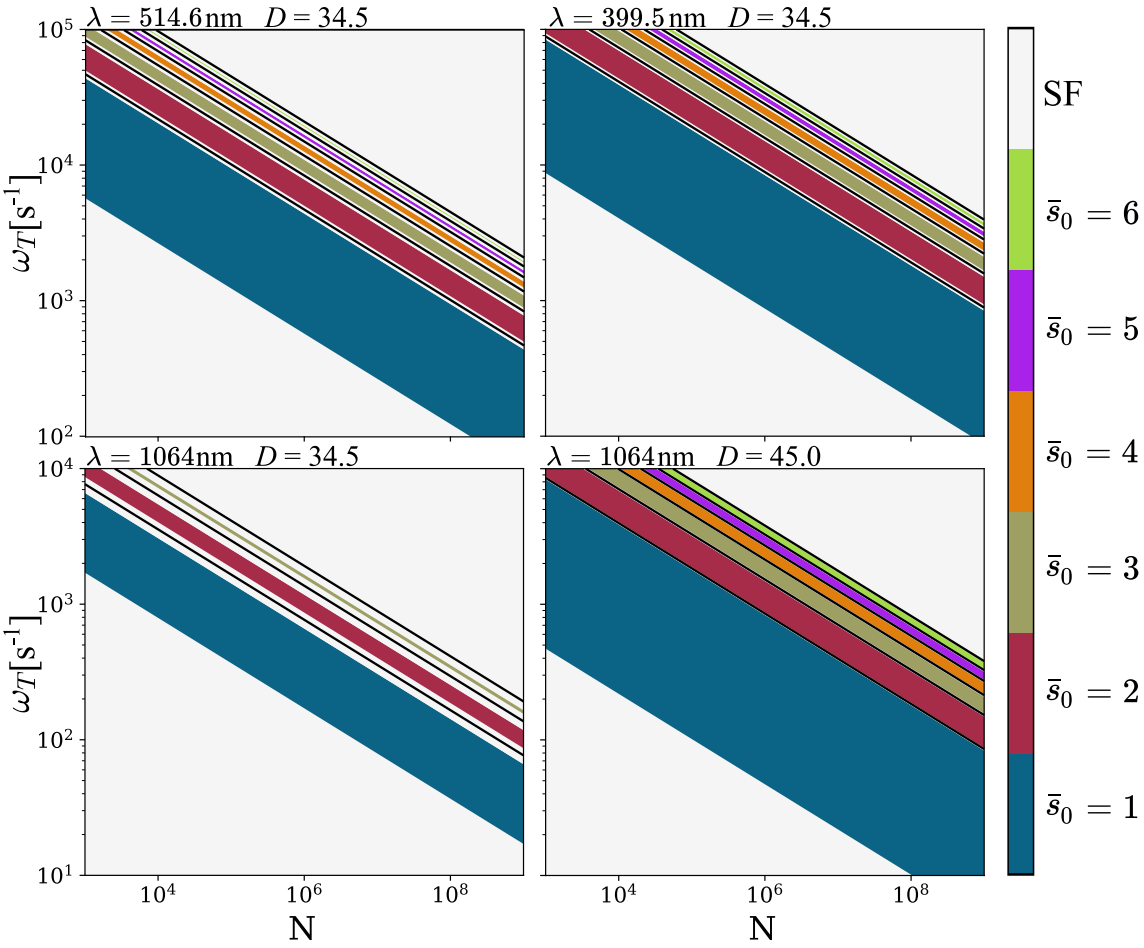

Figure 5.4: The expected ground state phase at the centre of a harmonic external potential in the parameter space of atom number N and external trap frequency ω_T. Plots assume a degenerate H gas in an optical lattice with specified wavelength and depth. Coloured segments indicate the phases for finite J, while black lines indicate transitions between MI filling states in the limit $J \to 0$ (up to the largest filling possible at finite J).

already discussed how one can predict the MI structure in section 5.2.3. It is now desirable to control the structure instead and ensure unitary filling in all MI regions. Working under the assumption of a harmonic external potential, it is sufficient to ensure a MI phase at the centre with unitary filling, i.e. $\bar{s}_0 = 1$. The lattice depth and wavelength can be fixed by measurement constraints, such as the need to be magic, and the need to pass the critical point. This leaves the total atom number N and the external trap frequency ω_T as the only free parameters in μ/U.

Figure 5.4 shows the phase at the centre of the external potential in the space of these parameters. Since $\mu/U \sim N^{2/5}$ and $\sim \omega_\mathrm{T}^{6/5}$, increasing either value causes the centre to pass through MI phases with successive fillings. Since calculation assumes a finite depth D, multiple regions

of SF phase exist: between the MI phases; for small values of μ/U that are "below" the $\bar{s} = 1$ lobe; and "above" the MI bands where U/J is not sufficient to be critical for high filling lobes.

It is clear that higher atom numbers require lower external trap frequencies to achieve the $\bar{s}_0 = 1$ phase. The dependence of this phase upon the wavelength is clear and can be understood in terms of the scaling $\mu/U \sim \lambda^{3/5}$. The dependence upon the lattice depth is far less obvious, as $\mu/U \sim D^{-9/20}$ and the range of depths shown in figure 5.4 is not sufficient to see this change at the given scale.

Take as an example, the magnetically trapped H condensate of [57]. This condensate contained 10^9 atoms in the harmonic region of the magnetic trap with a geometric average trap frequency of $\omega_{\mathrm{T}} = 3380\,\mathrm{s}^{-1}$. In a 514.6 nm lattice with $D = 34.5$, this gives $\mu/U = 10.6$ so[1] $\bar{n}_0 = 11$; whilst in the equivalent 399.5 nm lattice, $\mu/U = 4.97$ so[2] $\bar{s}_0 = 5$. To achieve unitary filling would require a reduction of the trap frequency to $440\,\mathrm{s}^{-1}$ for the 514.6 nm lattice or $840\,\mathrm{s}^{-1}$ in the 399.5 nm lattice. This reduction in external trap frequency relates to a decrease in the peak condensate density by up to an order of magnitude, which goes some way to alleviating the issue of dipolar relaxation.

5.3.2 The lattice beam profile

The lattice beams that form the potential V_{latt} are not homogeneous in intensity across their cross section. Instead they have some profile which has intensity peaking at the centre of the beam and exponentially decaying with increasing distance — a Gaussian beam (see [162]). Combining the profiles of the three orthogonal beams (assuming them to be identical in every other respect) gives an approximately spherical intensity profile:

$$I(r) = I_0 e^{-2r^2/w^2}, \tag{5.16}$$

where I_0 is the peak intensity that defines the depth of the lattice and w is the waist size of the beam. For r smaller than w, this variation in intensity provides a harmonic effective external potential,

$$V_{\mathrm{opt}}(r) \approx \frac{1}{2} m \omega_{\mathrm{opt}}^2 r^2, \tag{5.17}$$

[1] In actuality, this lobe is not accessible at this depth, so the centre will be in a SF state.
[2] This time, the lobe is accessible, but centre falls within the SF jacket between the $\bar{s} = 5$ and $\bar{s} = 6$ lobes.

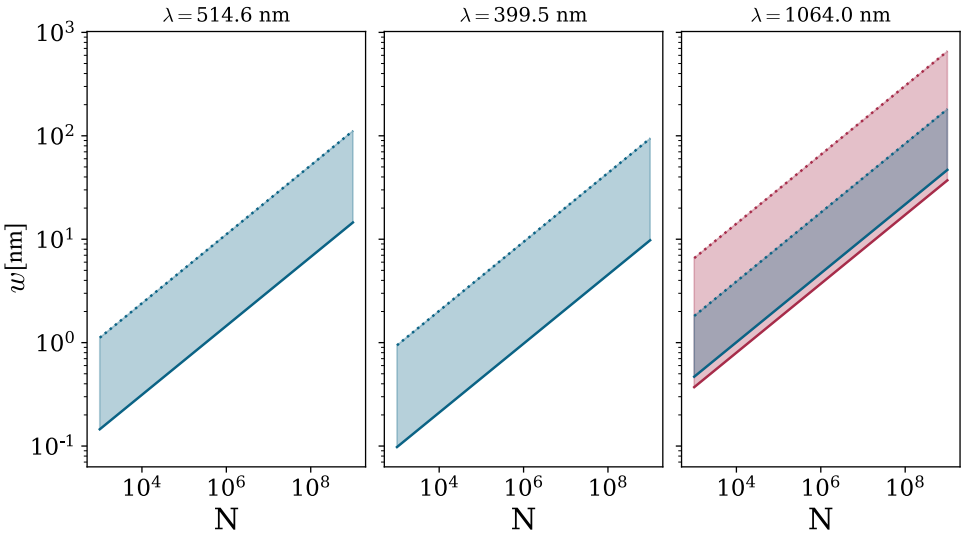

Figure 5.5: Bounds on Gaussian beam waists that will permit a $\bar{s}_0 = 1$ MI for a range of condensate numbers across three lattice wavelengths. In all three cases, the thick line indicates the lower bound, dotted lines indicate the upper bound, while the region in between is coloured. Blue indicates bounds for a lattice of depth $D = 34.5$ while red indicates bounds for $D = 45.0$.

with the trap frequency,

$$\omega_{\text{opt}} = \sqrt{\frac{D}{2}} \frac{h}{m_{\text{H}} a w}. \tag{5.18}$$

As in section 4.2, the low mass of H results in generally large trap frequencies that quickly dominate the external potential: e.g. a 514.6 nm lattice at $D = 34.5$ formed from Gaussian beams with 10 μm waists will give $\omega_{\text{opt}} = 6.57 \times 10^5\,\text{s}^{-1}$. Not only is this frequency 2 orders of magnitude larger than the external trap frequency of [57], but it precludes access to the $\bar{s}_0 = 1$ MI for any atom number, see figure 5.4.

The frequency ω_{opt} is heavily dependent upon the properties of the lattice itself, which cannot be tuned without affecting the entire system. The only parameter that is somewhat decoupled from the essential lattice properties is the beam waist w. Figure 5.5 shows the range of w that permit an $\bar{s}_0 = 1$ MI for the same lattices as in figure 5.4. Specific values of these ranges are reported in Table 5.2. One finds that waists of < 1 mm are only possible for 10^5 (for the magic wavelengths, 10^4 for 1064 nm) atoms or fewer. Even then, waists > 100 µm are almost universally required.

The need for such large beam waists introduces a serious technical problem: producing a lattice that can achieve $D > 30$ for 1S H requires very high beam intensities at any optical wavelength (see the 1S polarisability in figure 3.1). In a Gaussian beam, the average intensity

Table 5.2: Table showing the range of beam waist sizes that relate to an $\bar{s}_0 = 1$ filling MI state in two magic wavelength lattices of $D = 34.5$ at various atom numbers N. Atom numbers are given in orders of magnitude ranging from 10^3 to 10^9. Beam waists are given in mm to two significant figures.

$D = 34.5$							
$\log_{10}(N)$	3	4	5	6	7	8	9
w range [mm] $\lambda = 1064\,\mathrm{nm}$	0.47–1.8	1.0–3.9	2.2–8.4	4.7–18	10–39	22–84	47–180
w range [mm] $\lambda = 514.6\,\mathrm{nm}$	0.15–1.1	0.31–2.4	0.67–5.2	1.5–11	3.1–24	6.7–52	15–110
w range [mm] $\lambda = 399.5\,\mathrm{nm}$	0.098–0.94	0.21–2.0	0.45–4.4	0.98–9.4	2.1–20	4.5–44	9.8-94
$D = 45.0$							
w range [mm] $\lambda = 1064\,\mathrm{nm}$	0.37–6.6	0.80–14	1.7–30	3.7–66	8.0–140	17–300	37–660

scales according to power and waist as $I \sim P/w^2$, so maintaining a given intensity for wider beams requires quadratically increasing power. Given the high powers that would be required for narrow beams, the long-term stability of the source power/frequency becomes a serious concern.

5.4 Potential for modern experiments

As it stands, the conditions for creating a unitary MI from the BEC of Fried *et. al.* [57,140] are not ideal. The high number of the atoms in the condensate make it difficult to achieve unitary filling for external trap frequencies higher than $O(100)\,\mathrm{Hz}$. Relaxing the external magnetic trap to reach these trap frequencies is not a big problem, but doing so it in the lattice beam intensity profile requires waists of 10's–100's of mm. Non-Gaussian beam profiles may ease some of the focus requirements, and the $\bar{s}_0 = 1$ phase can be accessed for larger values of ω_T if N is decreased through natural (or forced) decay. The previous approach cannot be used as it is, but it may be adjusted into something more feasible using the modern techniques of cold atom experiments.

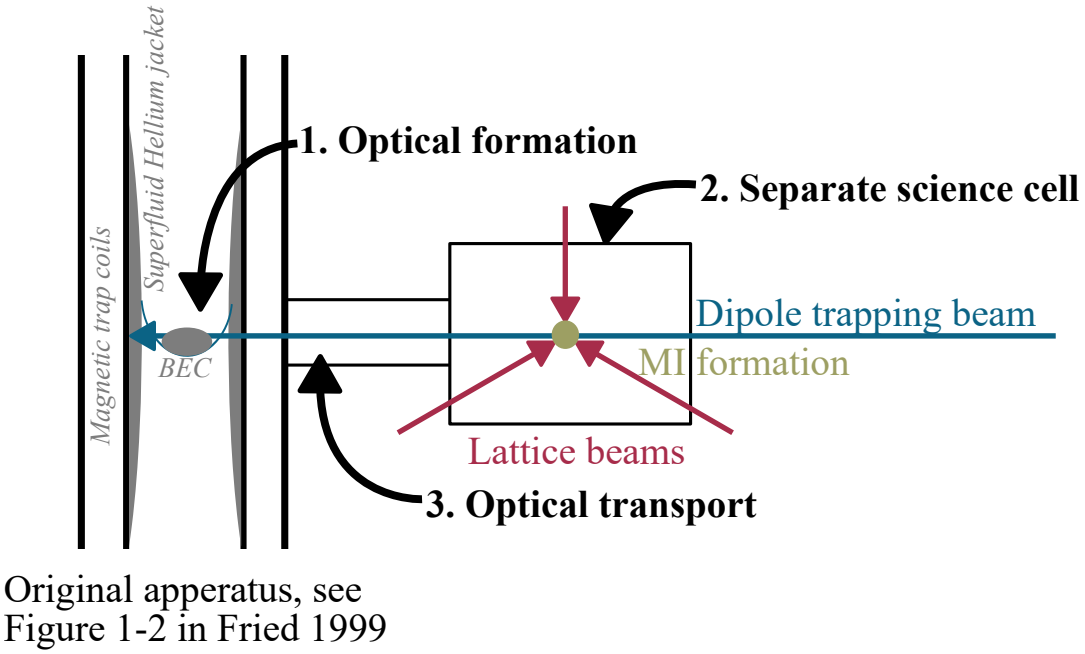

Figure 5.6: Sketch diagram indicating how the existing experimental method could be modernised for the production of a H MI. Only a simple indication of the existing experiment is given, with some key features pointed out in grey (a full description can be found in [140]). The three main changes are highlighted in **bold**: Optical formation, a separate science cell, and an optical transport stage.

5.4.1 A sketch proposal

Here, I will present an outline of what could be done to improve the H BEC experiment's suitability for producing a $\bar{s}_0 = 1$ MI. This is not an exhaustive evaluation of all possible improvements, nor is it a proposal for a new experiment. The intention is to highlight areas that could benefit most obviously from modernisation, and indicate how they could bring the result in line with a $\bar{s}_0 = 1$ MI. This sketch is outlined in 5.6, with more detailed explanations appearing in the text below:

1. **Optical formation:** Dipolar relaxation is the leading limitation on condensate lifetime in the existing experiment. An optical trap is confining for all magnetic sub-states and allows formation in the absolute ground state. This enables the effective elimination of dipolar relaxation from the condensed sample regardless of its density. A new formation method is an opportunity to achieve the smaller condensates that more easily enter the $\bar{s}_0 = 1$ phase.

2. **Separate science chamber:** It is standard practice in modern cold atom experiments,

to cool in one part of the experiment and then transfer to a separate "science chamber" for measurement. This distances the measurement from the complex field environment of the dilution fridge and allows for greater systematic control. Further, a separate science cell can be built with much better optical access than is possible in a dilution fridge, allowing for more advanced optical design and more advantageous field profiles.

3. **Optical transport:** Once a separate science cell has been established, it becomes an essential step to move the BEC from its formation stage to this cell. Since the BEC should already be optically confined, optical transport becomes the natural next step. Introducing this stage gives further opportunity for manipulating the properties of the BEC: e.g. through allowed loss to reduce N or manipulating the shape of the potential.

Put together, these changes allow a significant improvement in the prospects for controlling the parameters N and (to some extent) ω_{T} at the point of MI formation. Further, they should allow the H BEC to progress beyond the limitations imposed by dipolar relaxation. However, this sketch is not an experimental proposal and there are serious uncertainties surrounding a number of these changes: e.g. whilst optical formation has been posited, it is not immediately obvious how this will combine with the existing method; and optical transport necessitates an opening in the side of the cooling stage which will affect the cooling process.

5.4.2 Measurement limitations

It is clear that a unitary filling MI of H is, at least in principle, viable. It must be remembered, however, that such a MI was in mind explicitly as a suitable system for precision spectroscopy. Ultimately, this suitability is limited by the atomic properties of H in a way that is not obvious upon first inspection.

The anomalously small S-wave scattering length of H fundamentally weakens the onsite interaction potential U and leads to unusually large critical depths (table 5.1). Since the SF–MI transition is necessarily reversible, this sets lower bounds on lattice depths which are, mostly, larger than the minimal Lamb Dicke trap depths listed in table 4.3. While this necessarily puts the OLCs of chapter 3 deep in the Lamb Dicke regime, it increases the effect of trap-induced broadening. For example, achieving MI in a 399.5 nm lattice requires depths of at least $D = 29$,

which is 2.32 times larger than the relevant minimal Lamb Dicke depth of section. At this depth, two-photon ionisation broadens the 1S–2S line-width of 4.15 kHz, compared to the 0.857 kHz expected at the minimal Lamb Dicke depth $D = 12.5$.

It is essential to understand that the SF–MI transition occurs for a condensate in the atomic ground state and critical depths must be considered in terms of trapping the 1S state. As such, even measurements in non-magic traps must maintain these high lattice intensities. The key concern lies in the combination of these intensity requirements and the width requirements of section 5.3.2: for example, a unitary filling MI in a 1064 nm lattice requires a minimal depth of $28.8E_{\mathrm{rec}}$, or a peak field intensity of at least $23.6\,\mathrm{MWcm}^{-2}$. In a Gaussian beam, this must be focused to a waist $O(1)$ mm (depending on the number of atoms in the condensate , figure 5.5) demanding initial laser powers of at least $O(0.1)$ MW (a similar estimate for a 514.6 nm lattice indicates powers of at least $O(10)$ kW). Such large laser powers *may* be possible with some effort, but stabilising it (both in power and frequency) over the long time scales demanded in such an experiment imposes significant technical challenges.

Whilst a MI of H with uniform filling $\bar{s} = 1$ is certainly possible, its suitability for a precision spectroscopy experiment is dubious — limited by the atomic properties of H in ways that are not obvious upon first inspection. The small scattering length and reversible nature of the phase transition enforce deep traps for the 1S state — and so very high intensities. In itself, this limits potential 1S–2S OLCs, with minimal line-widths necessarily exceeding 4 kHz. In combination with the demands of weak external confinement, it begins to limit the experiment on a technical level. Overall, it is unclear if the promised regularity and ground state occupation of an $\bar{s}_0 = 1$ MI are worth the necessary deep trapping and long duty cycle.

Chapter 6

CONCLUSIONS AND OUTLOOK

It is easy to get excited by the potential evidence for new physics in the H spectral data-set, particularly as it appears to support popular minimal extensions to the SM [39] (e.g. Higgs-portal models, Dark photons etc.). However, it is impossible to draw meaningful conclusions regarding fifth forces while the question of unresolved systematics remains unanswered. In this thesis, I have studied the potential application of optical trapping to the precision spectroscopy of H, in search of tight control of motional systematics and improved precision.

This thesis reports several important contributions to the field of precision H spectroscopy, including the development of new, freely-available, software for the calculation of polarisability and atom-photon scattering rates of S-state H in linearly polarised off-resonant optical fields — as reported in chapter 3 (and **(b.)**). This software was put to work in chapter 4, where I derived new limits on the operation of proposed H/$\bar{\text{H}}$ lattice clocks. I highlighted the previously overlooked[2] effect of trap-induced broadening arising from multi-photon ionisation and inelastic atom-photon scattering in the 2S state (section 4.3). The high lattice intensities required by the poor polarisability of the H ground state result in this effect dominating the line-width of the 1S–2S transition. By combining this with results of atomic motion in a tightly confining optical trap (section 4.2), I placed reasonable limits on achievable line-widths that maintain the Lamb-Dickie regime (section 4.4). The large trap frequencies inherent to H mean that this can be achieved for much shallower lattices than is necessary for heavier atoms. I also report three new magic wavelengths for the 1S–2S magic wavelengths where narrower lines are possible (section 4.1.1). These results were also reported in the declared publication **(a.)** [1].

The lattice clock of chapter 4 (and **(a.)**) offers a new measurement of the 1S–2S transition in H, D and $\bar{\text{H}}$ in a common environment that is effectively free from systematics relating to atomic motion. This improvement in systematic uncertainty comes at an apparent cost in statistical uncertainty, but more work is needed to be sure. Such a measurement would

[2] e.g. in the work of Kawasaki [163] or the $\bar{\text{H}}$ clock proposal [51].

be incredibly useful: for comparison with the current value as a first test of systematic error within the current spectral data-set; for comparisons between H and D to place bounds on new physics with non-universal coupling that is independent of current tension in the data-set [40]; and for comparisons between H and $\bar{\mathrm{H}}$ with minimal systematic differences as a direct test of CPT violation. However, a precise measurement of the 1S–2S transition cannot go very far in resolving the proton charge radius puzzle or bounding new physics on its own. The ideal experiment would include trapped measurements of intervals including a range of high-lying Rydberg states. Intervals between Rydberg states offer a value of the Rydberg constant that is effectively decoupled from the proton charge radius (as per [27] and [34]). Combining these intervals with the new measurement of the 1S–2S transition (in a similar system) gives a data-set which could be used to extract values of r_{p}, R_{∞} and new physics parameters that are completely independent of the current H spectral data-set and its internal tensions.

While the 1S–2S measurement has been considered in detail in this thesis, analysis of the effects of optical trapping on the measurement of Rydberg intervals has been far less in-depth. Rydberg states are very sensitive to D.C. shifts from external electric fields and have very complicated Stark maps. As such, control of stray electric fields is essential, and the potential systematic contribution in an optical trap must be studied. In a similar vein, the trap lifetime of these Rydberg states must be considered: estimation of ionisation rates could be done with the STRFLO code, but the large number of possible final states (and a general extension beyond S-states) means that my approach to atom-photon scattering would need serious amending. Further, a full measurement protocol, that maximises the advantages of trapped atoms whilst minimising the effects of non-magic trapping, must be explicitly formulated. Such a formulation would, naturally, depend heavily upon the specifics of the loading mechanism.

I discussed the issue of cooling/trapping in chapter 5, where I considered the proven cryogenic/evaporative route to H BEC. I studied the possibility of driving the SF–MI transition to produce a low-entropy, ultra-cold lattice of H for spectroscopy (section 5.2). For the first time, I reported the critical conditions for this transition in H and compared them to Rb (section 5.3). I found that anomalously small S-wave scattering length resulted in large critical depths, but also allowed rapid adiabatic ramping. I calculated new conditions for achieving unitary filling (section 5.3.1) and found that the external potential from the lattice beams is a critical

limiting factor, requiring absurdly large Gaussian waists with high peak intensities (section 5.3.2). While a unitary filling MI is possible, it is clear that it sits within a highly unfavourable region of parameter space, both from a technical perspective and as an environment for precision spectroscopy.

Without a suitable MI in mind, there is little motivation to reproduce a BEC of H from the perspective of precision spectroscopy. However, the cryogenic/evaporative methods of cooling H should not be immediately discarded. Prior to condensation, the method reliably produces ultra-cold (120 µK) gasses of H at high densities by saddle-point evaporation alone [57,140]. It is perfectly reasonable to consider loading a lattice/tweezer array by superimposing the potential over the gas. Since $E_{\mathrm{rec}} \sim 10's$ µK at the magic wavelengths, stochastic loading in this way might provide a sufficient probability for trapping cold H atoms in suitably shallow traps. OLCs loaded in this manner could theoretically operate at the minimal line-widths of table 4.3. This should be the topic of further investigation, along with sophisticated methods for preventing $s > 1$ on any given site, minimising vibrational state, and maximising the number of occupied lattice sites.

When I began working on this topic, there was a sense that a step-change in experimental procedure was needed but no clear paths towards this had yet been formulated. In the past three and a half years, new global fits [39, 40], additional spectroscopic results [33, 34], and advances in $\bar{\mathrm{H}}$ physics [74, 164] have enhanced the motivation for change. The core problems identified at the start of this thesis — tension in the H data-set, uncertain cooling/trapping prospects etc. — persist, but now there are at least two groups actively working towards optically trapped H with viable experimental schemes [70,135,136]. To this rapidly developing field, this thesis has contributed new software for the calculation of essential optical trapping parameters; new limits on the operation of a 1S–2S lattice clock (and the implications of this upon other measurements); and an assessment of the feasibility of a unitary filling MI of H — the ultimate low-entropy lattice system.

It is likely that the groups of T. Zelevinsky and T. Udem will achieve ultra-cold H confined in tweezer arrays at some point in the near future. This will open the door to precision spectroscopy of both the 1S–2S transition and high-lying Rydberg states with a completely new set of dominating systematics. However, the community must not again fall into the trap

of relying upon a small number of central frequency measurements conducted by a single group with a single method. The ideal scenario would involve the comparison of multiple, independent H data-sets produced by different groups. Once all systematic tension has been removed, then the exciting work of bounding new physics can begin in earnest.

Appendix A

ANALYTIC DETAILS FOR CHAPTER 3

A.1 Matrices for the Schrödinger equation

Parts of this appendix follow work that can be found in **(a.)**.

The Hamiltonian

The matrix elements of $\mathcal{H}$ are given by the integral,

$$\mathcal{H}_{\mathtt{n}'l'm',nlm} = \int d\boldsymbol{r}^3 \frac{1}{r} S^{(\zeta)}_{\mathtt{n}'l'}(r) Y_{lm}(\theta,\phi) \mathfrak{H}_0 \frac{1}{r} S^{(\zeta)}_{\mathtt{n}'l'}(r) Y_{lm}(\theta,\phi). \tag{A.1}$$

The Hamiltonian is the same as that given in equation 2.4 and written as the product of radial and angular components. Since the spherical harmonics are eigenfunctions of the angular part of $\mathfrak{H}_0$, it is straightforward to show that this integral reduces to,

$$\mathcal{H}_{\mathtt{n}'l'm',\mathtt{n}lm} = \delta_{l'l}\delta_{m'm} \int_0^\infty dr S^{(\zeta)}_{\mathtt{n}'l'} \left[-\frac{1}{2}\left(\frac{d^2}{dr^2} - \frac{l'(l'+1)}{r^2} \right) - \frac{1}{r} \right] S^{(\zeta)}_{\mathtt{n}l}. \tag{A.2}$$

This simplifies matters, as it is only necessary to treat cases where $l' = l$. This integral can be computed analytically using the relations between Laguerre polynomials given in [3] to give,

$$\begin{aligned} \mathcal{H}_{\mathtt{n}'l'm',\mathtt{n}lm} = \delta_{l'l}\delta_{m'm} \Bigg[\left(\frac{1}{2}\eta(\mathtt{n}'+l) - 1 \right) \delta_{\mathtt{n}'\mathtt{n}} + \frac{1}{4}\eta\sqrt{\mathtt{n}'(\mathtt{n}'+2l+1)}\delta_{\mathtt{n}'(\mathtt{n}-1)} \\ + \frac{1}{4}\eta\sqrt{(\mathtt{n}'-1)(\mathtt{n}'+2l)}\delta_{\mathtt{n}'(\mathtt{n}+1)} \Bigg]. \end{aligned} \tag{A.3}$$

This matrix is real, symmetric, tridiagonal in $\mathtt{n}$, and diagonal in l and m.

The overlap matrix

The overlap between pairs of basis functions also forms a matrix in $\mathcal{B}$ defined by the matrix elements,

$$\begin{aligned} \mathcal{T}_{\mathtt{n}'l'm',\mathtt{n}lm} &= \left(\int_0^\infty dr S^{(k)}_{\mathtt{n}'l'}(r) S^{(k)}_{\mathtt{n}l}(r) \right) \left(\int_0^\pi \sin\theta d\theta \int_0^{2\pi} d\phi Y^*_{l'm'}(\theta,\phi) Y_{lm}(\theta,\phi) \right) \\ &= \delta_{l'l}\delta_{m'm} \int_0^\infty dr S^{(k)}_{\mathtt{n}'l'}(r) S^{(k)}_{\mathtt{n}l}(r). \end{aligned} \tag{A.4}$$

The resultant radial integral can be computed analytically in the same way as for the Hamiltonian, giving the matrix elements,

$$\mathcal{T}_{\mathtt{n}'l'm'} = \frac{1}{2k}\delta_{l'l}\delta_{m'm}\left(2(\mathtt{n}+l)\delta_{\mathtt{n}'\mathtt{n}} - \sqrt{\mathtt{n}(\mathtt{n}+2l+1)}\delta_{\mathtt{n}'(\mathtt{n}+1)} - \sqrt{(\mathtt{n}-1)(\mathtt{n}+2l)}\delta_{\mathtt{n}'(\mathtt{n}-1)}\right). \tag{A.5}$$

A.2 The dipole matrix element

I begin by defining a basis of spherical unit vectors for polarisation:

$$\hat{\boldsymbol{\varepsilon}}_{-1} = \frac{\hat{\boldsymbol{x}} - i\hat{\boldsymbol{y}}}{\sqrt{2}}, \qquad \hat{\boldsymbol{\varepsilon}}_0 = \hat{\boldsymbol{z}}, \qquad \hat{\boldsymbol{\varepsilon}}_{+1} = -\frac{\hat{\boldsymbol{x}} + i\hat{\boldsymbol{y}}}{\sqrt{2}}.$$

Any polarisation vector may then be written simply in this basis as $\boldsymbol{\varepsilon} = \sum_{q\in\{0,\pm1\}} \varepsilon_q \hat{\boldsymbol{\varepsilon}}_q$. I am interested in the dipole matrix element between two atomic states a and b:

$$\boldsymbol{\varepsilon}\cdot\boldsymbol{r}_{ba} = \sum_{q\in\{0,\pm1\}} \varepsilon_q \int d\boldsymbol{r}^3 R^*_{n_b,l_b}(r) Y^*_{l_b,m_b}(\theta,\phi)\hat{\boldsymbol{\varepsilon}}_q\cdot\mathfrak{r} R_{n_a,l_a}(r) Y_{l_a,m_a}(\theta,\phi) \tag{A.6}$$

The dipole operator may be written in the spherical unit basis as,

$$\hat{\varepsilon}_q\cdot\mathfrak{r} = \sqrt{\frac{4\pi}{3}} r Y_{1q}(\theta,\phi). \tag{A.7}$$

and the dipole matrix element may be written as the product of angular and radial components,

$$\boldsymbol{\varepsilon}\cdot\mathfrak{r}_{ba} = r_{ba}\sum_{q\in\{0,\pm1\}} \varepsilon_q A_{l_b m_b q, l_a m_a}. \tag{A.8}$$

The radial component is given by the radial matrix element:

$$r_{ba} = \int_0^\infty r^2 dr R^*_{n_b,l_b}(r) r R_{n_a,l_a}(r). \tag{A.9}$$

The angular part is given by the matrix elements,

$$\begin{aligned} A_{l_b m_b q, l_a m_a} &= \sqrt{\frac{4\pi}{3}}\int_0^\pi \sin\theta d\theta \int_0^{2\pi} d\phi Y^*_{l_b m_b}(\theta,\phi) Y_{1q}(\theta,\phi) Y_{l_a m_a}(\theta,\phi) \\ &= (-1)^{-(m_a+q)}\sqrt{(2l_a+1)(2l_b+1)} \times \begin{pmatrix} l_b & 1 & l_a \\ 0 & 0 & 0 \end{pmatrix}\begin{pmatrix} l_b & 1 & l_a \\ -(m_b) & q & m_a \end{pmatrix}\delta_{m_b,m_a+q}. \end{aligned} \tag{A.10}$$

It is necessary to consider the representation of the radial matrix element in $\mathcal{B}$. Luckily, the form of the angular matrix elements helps simplify matters — A is non-zero only when $|l - l'| = 1$. As such, r_{ba} can be represented as the sum of two matrices in $\mathcal{B}$:

$$\mathcal{R}^{+}_{\mathtt{n}',\mathtt{n}l_a} = \int_0^\infty dr S^{(\zeta)}_{\mathtt{n}'(l_a+1)}(r) r S^{(\zeta)}_{\mathtt{n}l_a}(r), \tag{A.11}$$

which couples states of given l_a to those with $l_b = l_a + 1$; and

$$\mathcal{R}^{-}_{\mathtt{n}',\mathtt{n}l_a} = \int_0^\infty dr S^{(\zeta)}_{\mathtt{n}'(l_a-1)}(r) r S^{(\zeta)}_{\mathtt{n}l_a}(r), \tag{A.12}$$

which couples l_a to $l_a - 1$. Just as for $\mathcal{H}$ and $\mathcal{T}$, these integrals can be solved to give analytic formulae for the matrix elements. The computation in this case is far more involved than for $\mathcal{H}$ or $\mathcal{T}$, but is still based upon the applications of relations between Laugerre polynomials found in [3]. Ultimately one obtains matrix elements:

$$\begin{aligned}\mathcal{R}^{+}_{\mathtt{n}',\mathtt{n}l_a} = \frac{1}{4\zeta^2}\Big[&-\sqrt{(\mathtt{n}'+2l_a+2)(\mathtt{n}'+2l_a+1)(\mathtt{n}'+2l_a)(\mathtt{n}'-1)}\delta_{\mathtt{n}'(\mathtt{n}+1)} \\ &+2(2\mathtt{n}'+l_a)\sqrt{(\mathtt{n}'+2l_a+2)(\mathtt{n}'+2l_a+1)}\delta_{\mathtt{n}'\mathtt{n}} - 6(\mathtt{n}'+l_a+1)\sqrt{\mathtt{n}'(\mathtt{n}'+2l_a+2)}\delta_{\mathtt{n}'(\mathtt{n}-1)} \\ &+2(2\mathtt{n}'+3l_a+4)\sqrt{\mathtt{n}'(\mathtt{n}'+1)}\delta_{\mathtt{n}'(\mathtt{n}-2)} - \sqrt{(\mathtt{n}'+2l_a+3)(\mathtt{n}'+2)(\mathtt{n}'+1)\mathtt{n}'}\delta_{\mathtt{n}'(\mathtt{n}-3)}\Big],\end{aligned} \tag{A.13}$$

for the l-raising matrix, and

$$\begin{aligned}\mathcal{R}^{-}_{\mathtt{n}',\mathtt{n}l_a} = \frac{1}{4\zeta^2}\Big[&-\sqrt{(\mathtt{n}+2l_a-2)(\mathtt{n}+2l_a-1)(\mathtt{n}+2l_a)(\mathtt{n}-1)}\delta_{\mathtt{n}'(\mathtt{n}-1)} \\ &+2(2\mathtt{n}+l_a-1)\sqrt{(\mathtt{n}+2l_a)(\mathtt{n}+2l_a-1)}\delta_{\mathtt{n}'\mathtt{n}} - 6(\mathtt{n}+l_a)\sqrt{\mathtt{n}(\mathtt{n}+2l_a)}\delta_{\mathtt{n}'(\mathtt{n}+1)} \\ &+2(2\mathtt{n}+3l_a+1)\sqrt{\mathtt{n}(\mathtt{n}+1)}\delta_{\mathtt{n}'(\mathtt{n}+2)} - \sqrt{(\mathtt{n}+2l_a+1)(\mathtt{n}+2)(\mathtt{n}+1)\mathtt{n}}\delta_{\mathtt{n}'(\mathtt{n}+3)}\Big],\end{aligned} \tag{A.14}$$

for the l-lowering.

A.3 Angular parts for S state scattering

For the calculations considered in section 3.3, the external field is assumed to be linearly polarised in the $\hat{\boldsymbol{z}}$ direction. As such, $\varepsilon_0 = 1$ while $\varepsilon_{\pm 1} = 0$ and only terms with $q = 0$ survive. The scattered photon however, is not generally limited in is polarisation. Therefore, it has a polarisation vector,

$$\boldsymbol{\varepsilon}_s = \sum_{q\in\{-1,0,1\}} \sqrt{\frac{4\pi}{3}} Y_{1q}(\vartheta_s, \varphi_s)(-1)^q \hat{\boldsymbol{\varepsilon}}_{-q}. \tag{A.15}$$

Calculations are further restricted to initial S-states, $l_a = 0$. This restricts k to P states only and so each sum has a single angular term that is common to all terms in the sum. The angular terms of the two sums differ only by the terms $A_{l_b m_b - q, 1 m_k} A_{1 m_k 0,00}$ for (i) and $A_{l_b m_b 0, 1 m_k} A_{1 m_k - q,00}$ for (ii). $A_{l_b m_b - q, 1 m_k} A_{1 m_k 0,00}$ and $A_{l_b m_b 0, 1 m_k} A_{1 m_k - q,00}$ can be written explicitly using equation (A.10). Applying the delta functions and ignoring common terms leaves the possible equality:

$$\begin{pmatrix} l_b & 1 & 1 \\ q & -q & 0 \end{pmatrix} \begin{pmatrix} 1 & 1 & 0 \\ 0 & 0 & 0 \end{pmatrix} \stackrel{!}{=} (-1)^q \begin{pmatrix} l_b & 1 & 1 \\ q & 0 & -q \end{pmatrix} \begin{pmatrix} 1 & 1 & 0 \\ q & -q & 0 \end{pmatrix}. \tag{A.16}$$

For l_b an even number (assured for an initial S state), symmetries of the Wigner 3-j symbol mean that the first symbol on the LHS is equal to the first symbol and sign term on the RHS. One can then check the remaining symbol for each allowed value of $q \in 0, \pm 1$ and see that the equality holds. One can also check that $A_{l_b m_b 1, 1 m_k} = A_{l_b m_b - 1, 1 m_k}$. Therefore, all terms in both sums share a common angular term, and equation (3.8) can be recast as equation (3.26):

$$R_{ba} = \omega_s^3 \alpha_{\mathrm{FS}}^4 \mathcal{A}_{ba} \left(\sum_k \frac{r_{bk} r_{ka}}{E_{ka} \mp \omega} + \frac{r_{bk} r_{ka}}{E_{kb} \pm \omega} \right)^2 I, \tag{A.17}$$

where the angular term is given by:

$$\mathcal{A}_{ba} = \int d\Omega \left[\sum_{s=1,2} \sum_{q \in \{0, \pm 1\}} \left| \sqrt{\frac{4\pi}{3}} (-1)^q Y_{1q}^*(\vartheta_s, \varphi_s) A_{l_b m_b - q, 1 m_k} A_{1 m_k, 00} \right|^2 \right]. \tag{A.18}$$

Terms in the integrand are vanishing in all cases except when $m_k = 0$, and $m_b = m_k - q = -q$ due to the delta functions present in A.10. As such, for a final state b with well defined m_b, only a single vale of q contributes to the above integral and scattering is allowed for final states with $m_b \in \{0, \pm 1\}$. Summing over all possible values of m_b and applying the definitions of ϑ_s and φ_s in 3.6, one obtains,

$$\begin{aligned} \sum_{m_b} \mathcal{A}_{ba} = \int d\Omega \Bigg[& \left| \sin(\vartheta) A_{l_b 00, 10} A_{10,00} \right|^2 + 0 + \left| -\frac{\sqrt{2}}{2} \cos(\vartheta) e^{i\varphi} A_{l_b 11, 10} A_{10,00} \right|^2 + \\ & \left| -i \frac{\sqrt{2}}{2} e^{i\varphi} A_{l_b 11, 10} A_{10,00} \right|^2 + \left| -\frac{\sqrt{2}}{2} \cos(\vartheta) e^{-i\varphi} A_{l_b - 1 - 1, 10} A_{10,00} \right|^2 + \left| i \frac{\sqrt{2}}{2} e^{-i\varphi} A_{l_b - 1 - 1, 10} A_{10,00} \right|^2 \Bigg] \\ = & \int d\Omega \left[\sin^2(\vartheta) (A_{l_b 00, 10} A_{10,00})^2 + \left(\cos^2(\vartheta) + 1 \right) (A_{l_b \pm 1 \pm 1, 10} A_{10,00})^2 \right]. \end{aligned} \tag{A.19}$$

Integrating over the direction of the scattered photon yields the final result,

$$\sum_{m_b} \mathcal{A}_{ba} = \frac{8\pi}{3} \left((A_{l_b 00, 10} A_{10,00})^2 + 2 (A_{l_b \pm 1 \pm 1, 10} A_{10,00})^2 \right). \tag{A.20}$$

Appendix B

COMPARISONS BETWEEN NUMERICAL RESULTS AND ANALYTIC THEORY

Existing literature values are not available for all results calculated in this thesis. Where they are, it is instructive to compare between my calculations and those of others.

B.1 Atomic polarisability

Tables of H polarisability do not appear in the literature, so there are no explicit reported values to compare against. However, Adhikari *et. al.* do report analytic expressions for the polarisability of the H 1S and 2S states [111]. Figure B.1 compares these analytic expressions to the numerical calculations described in chapter 3. Away from the 1/2S – nP resonances (where I expect the numerical approach to break down), I find that the computational results agree with the analytic results far beyond the limit of physical significance[2] — $O(10^{-4})$.

B.2 Magic wavelengths

Only one magic wavelength for the 1S–2S transition in H has been reported in the literature: 514.646 nm with associated polarisability 4.72750 a.u. [111]. These values match the results of numerical calculation with $\mathtt{n}_{\max} = 300$ and $\zeta = 0.3$ to the reported precision.

Beyond this, a number of magic wavelengths for other 1S–nS and 2S–nS transitions have recently been reported in the analytic calculations of Adhikari *et. al.* [101]. Table B.1 compares these magic wavelengths, as well as local polarisability gradient, to the results of calculation with the software [2]. I find exact agreement (to the reported precision of 10^{-6}) in the values of

[2]Note that figure B.1 calculates the absolute difference in a.u. For the 2S state, polarisability away from the zero crossings is generally very large (especially around the resonances).

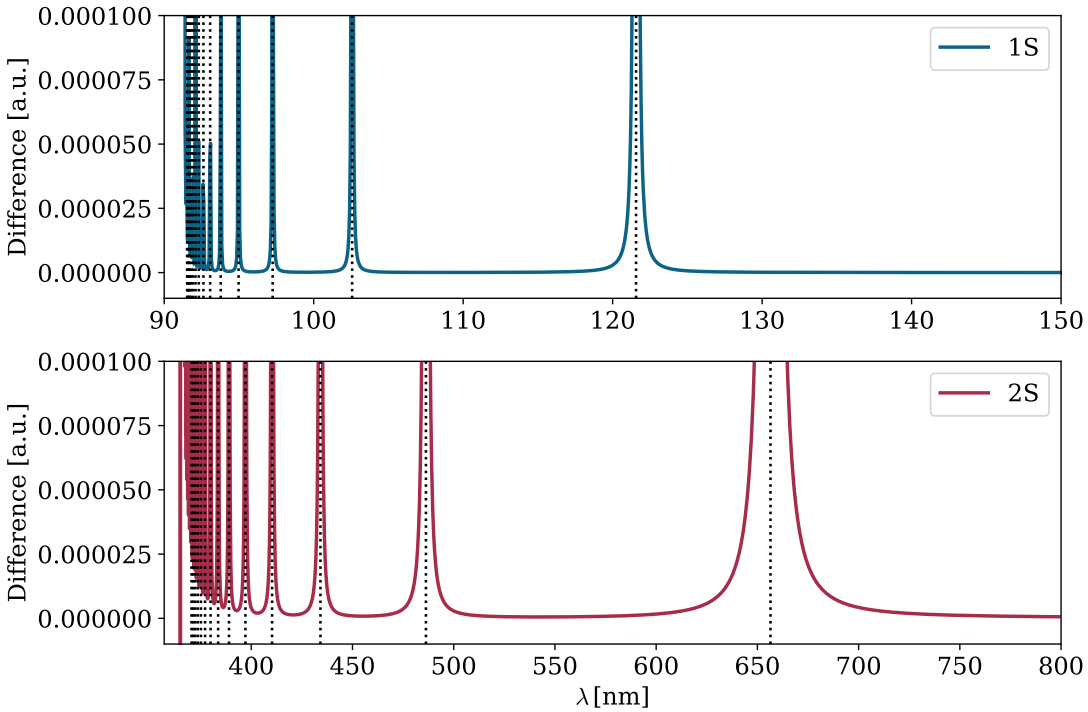

Figure B.1: The between the calculated 1S (a) and 2S (b) polarisability compared to analytic formulae. Dotted black lines indicate 1/2S–nP resonances. Difference is plotted for the same range of wavelengths as appears in figure 3.1, given in nm. The colours also match those used in figure 3.1.

the magic wavelengths. Small discrepancies in the value of χ, can be put down to the inclusion of the reduced mass into the Bohr radius when Adhikari *et. al.* define their units.

B.3 Atom-photon scattering rates

Explicit values of atom-photon scattering rates are not common in the literature. However, values of the scattering cross sections for the 2S–1S (both Raman scattering and SSTPE) are repoted in works by Klarsfeld [99] and Heno etl. al. [100]. Table B.3 reports these rates along with a numerical value calculated from the scattering rates of [2] according to equation 3.7:

$$\sigma = R\frac{\omega}{I}. \tag{B.1}$$

Note that the analytic expressions used by Klarsfeld and Heno scale according to the classical electron radius r_e as $\sigma \sim r_e^2$. Klarsfeld takes the value $r_e = 2.81777 \times 10^{-15}\,\mathrm{cm}$. The modern CODATA recommended value should read $r_e = 2.81794 \times 10^{-15}\,\mathrm{cm}$, which should be further corrected by the reduced mass to be consistent with the rest of the calculation as r_e/μ_H. As

Table B.1: Table of magic wavelengths, and the slope in the differential polarisability at this wavelength, calculated using this software for a variety of 1S–nS and 2S–nS transitions. Also, the difference between these values and the values reported by Adhikari *et al* in [101] Calculated values are presented to 6 significant figures to match those reported by Adhikari *et al.* Deviations are presented to match the number of decimal places of the values they relate to. In the case when a value is exactly zero, it is written only as 0, i.e. $0 = 0.000$. The term $\frac{e^2 a_0^2/E_\mathrm{H}}{\mathrm{nm}}$ defines the atomic unit of polarisability.

Transition	Calculated		Deviation from [101]	
	λ[nm]	$\chi\left[\frac{e^2a_0^2/E_\mathrm{h}}{\mathrm{nm}}\right]$	$\Delta\lambda$[nm]	$\Delta\chi\left[\frac{e^2a_0^2/E_\mathrm{h}}{\mathrm{nm}}\right]$
1S–2S	514.646	-5.2129	0	0.0057
1S–3S	1371.85	-10.922	0	0.012
1S–4S	2812.77	-23.064	0	0.025
1S–5S	4938.67	-53.080	0	0.058
1S–6S(I)	6321.10	-27.047	0	0.030
1S–6S(II)	7094.95	49.447	0	-0.054
1S–7S	9255.47	-69.631	0	0.076
1S–8S	13066.4	-113.08	0	0.13
2S–3S	1359.73	-13.325	0	0.015
2S–4S	2807.60	-24.013	0	0.026
2S–5S	4936.47	-53.773	0	0.058
2S–6S(I)	6307.82	-27.573	0	0.030
2S–6S(II)	7097.28	+50.404	0	-0.055
2S–7S	9253.80	-69.985	0	0.077
2S–8S	13065.4	-113.34	0	0.13

such the literature values reported in table B.3 are corrected as $\sigma \to \sigma \times 1.00096$. Under this correction, the numerical results show good agreement to the literature values up to the reported accuracy. Small differences in the last significant figure can be put down to rounding errors when correcting the literature terms. Larger differences around the 2S–3P resonance at 656.3 nm where perturbation theory becomes inappropriate.

Further comparison can be made to the scattering cross sections for the 2S–3S/D processes as reported by Heno [100]. These results are reported in table B.2 with the same considerations as before and show a similar level of agreement up to rounding errors.

Table B.2: Table of atom-photon scattering cross sections for the 2S–3S/D processes in H. There are two columns for each process: “H" which gives the results listed in the work of Heno *et. al.* [100]; and “N" which gives the numerical results of calculation with the code described in chapter 3 [2]. Numerical results are always given to 4 significant figures, while literature values are given to the reported precision and are corrected as $\sigma \rightarrow \sigma \times 1.00096$. The numbers in brackets indicate powers of 10: e.g. 4.86(-23) is equivalent to writing 2.86×10^{-23}. All values are given in units of cm^2.

λ[nm]	2S–3S		2S–3D	
	H	N	H	N
488	4.86(-23)	4.869(-23)	5.36(-24)	5.367(-24)
514.5	4.44(-25)	4.431(-25)	3.83(-26)	3.842(-26)
530	2.41(-25)	2.416(-25)	1.95(-26)	1.952(-26)
647.1	6.13(-27)	6.134(-27)	4.03(-28)	4.036(-28)

Table B.3: Table of atom-photon scattering cross sections for the 2S–1S Raman scattering, 2S–1S SSTPE and 2S–2S processes in H. There are three columns for each process: “K" which gives the results listed in the work of Klasfeld [99]; “H" which gives the results listed in the work of Heno *et. al.* [100]; and “N" which gives the numerical results of calculation with the code described in chapter 3 [2]. Numerical results are always given to 4 significant figures, while literature values are given to the reported precision and are corrected as $\sigma \to \sigma \times 1.00096$. The numbers in brackets indicate powers of 10: e.g. 1.05(-21) is equivalent to writing 1.05×10^{-21}. All values are given in units of cm^2.

λ[nm]	2S–1S RS			2S–1S SSTPE			2S–2S		
	K	H	N	K	H	N	K	H	N
488	-	1.05(-21)	1.052(-21)	-	7.18(-25)	7.176(-25)	-	1.28(-22)	1.286(-22)
500	2.253(-23)	-	2.252(-23)	7.472(-25)	-	7.472(-25)	8.354(-25)	-	8.355(-25)
514.5	-	5.84(-24)	5.841(-24)	-	7.84(-25)	7.835(-25)	-	1.14(-27)	1.235(-27)
530	1.932(-24)	1.93(-24)	1.932(-24)	8.227(-25)	8.23(-25)	8.227(-25)	1.245(-25)	1.24(-25)	1.245(-25)
600	6.988(-24)	-	6.988(-24)	1.006(-24)	-	1.006(-24)	3.451-24)	-	3.452(-24)
647.1	-	9.69(-22)	9.686(-22)	-	1.13(-24)	1.134(-24)	-	1.51(-22)	1.514(-22)
655	4.563(-20)	-	4.561(-20)	-	-	1.156(-24)	6.266(-21)	-	6.264(-21)
657	3.623(-19)	-	3.627(-19)	-	-	1.162(-24)	4.824(-20)	-	4.828(-20)
657.5	-	9.65(-20)	9.695(-20)	-	1.16(-24)	1.163(-24)	-	1.27(-20)	1.281(-20)
693.4	1.285(-22)	-	1.285(-22)	1.265(-24)	-	1.264(-24)	1.048(-23)	-	1.048(-23)
694.3	-	1.24(-22)	1.239(-22)	-	1.26(-24)	1.267(-24)	-	9.99(-24)	9.995(-24)
800	2.371(-23)	-	2.371(-23)	1.574(-24)	-	1.574(-24)	7.074(-25)	-	7.073(-25)
900	1.568(-23)	-	1.568(-23)	1.877(-24)	-	1.877(-24)	2.335-25)	-	2.335(-25)
1000	1.302(-23)	-	1.301(-23)	2.190(-24)	-	2.190(-24)	1.089(-25)	-	1.089(-25)
1060	1.220(-23)	1.22(-23)	1.220(-23)	2.382(-24)	2.38(-24)	2.381(-24)	7.509(-26)	7.51(-26)	7.509(-26)
10600	-	4.38(-23)	4.379(-23)	-	3.81(-23)	3.815(-23)	-	3.30(-30)	3.302(-30)

Appendix C

NUMERICAL CALCULATIONS OF THE WANNIER FUNCTIONS.

We note that for a separable 3D potential like V_{latt}, the Bloch functions are also separable into 3 orthogonal 1D functions: $\phi_{\boldsymbol{q}}(\boldsymbol{r}) = \phi_{q_x}(x)\phi_{q_y}(y)\phi_{q_z}(z)$. We can then write the Wannier functions $w(\boldsymbol{r} - \boldsymbol{R}_i) = \prod_\nu w(x_\nu - X_{\nu,i})$, as the product of 1D functions,

$$w(x_\nu - X_{\nu,i}) = \sqrt{\frac{a}{2\pi}} \int_{\pi/a}^{\pi/a} dq_\nu e^{-iX_{\nu,i}q_\nu} \phi_{q_\nu}(x_\nu). \tag{C.1}$$

These 1D Wannier functions are plotted in figure 5.1 and can themselves be computed in terms of a Fourier transform of the Bloch functions [153]:

$$w(x_\nu - X_i) = \int_{-\pi/a}^{\pi/a} dq_\nu e^{iq_\nu(x-X_i)} \sum_{j\in\{-l,\ldots,l\}} c_j^{0,q} e^{i2k_{\text{light}}x_\nu j}. \tag{C.2}$$

Where the complex coefficients $c_j^{(n,q)}$ can be computed by solving the eigenvalue equation

$$\sum_{j'=-\infty}^{\infty} H_{jj'} c_{j'}^{(n,q)} = E_n c_j^{(n,q)}, \tag{C.3}$$

with the Hamiltonian (in units of E_{rec}),

$$H_{j'j} = ((2jk_{\text{light}} + q)^2 + D/2)\delta_{j'j} - (D/4)\delta_{j'(j\pm1)}. \tag{C.4}$$

To treat this numerically, j mus be restricted to some finite set of integers, $j \in \{-j_{\max}, ..., j_{\max}\}$. For the lowest band one gets goof results by choosing $j_{\max} \approx 10$. The 1D function is computed for specific x_ν by numerical integration over 100 values of q_ν distributed evenly from $-\pi/a$ to π/a.

The tunneling and interaction potentials J and U are given as integrals of Wannier functions in chapter 5. Consider the interaction potential first. It is simple to show that U can be written in terms of the 1D Wannier functions,

$$U = \frac{4\pi\hbar^2 a_s}{m} \left(\int dx |w(x)|^4 \right)^3. \tag{C.5}$$

Spatial integration is implemented in the same way as integration over the quasimomentum, only this time over a 800 values of x distributed evenly from $-4a$ to $4a$.

Expressing J in terms of the 1D functions requires a little more effort. Start by applying the definition of the Wannier functions to equation 5.2. Given that the Bloch functions are, by construction, eigenfunctions of this one particle Hamiltonian $-\hbar^2/2m + V_{\text{latt}}(\boldsymbol{r})$, J can be written as:

$$J = \frac{a^3}{(2\pi)^6} \int_{\text{BZ}} d\boldsymbol{q} e^{i\boldsymbol{q}\cdot\boldsymbol{R}_i} \int_{\text{BZ}} d\boldsymbol{q'} e^{i\boldsymbol{q'}\cdot\boldsymbol{R}_j} E_0(\boldsymbol{q}) \int d\boldsymbol{r}^3 \phi^*_{0,\boldsymbol{q}}(\boldsymbol{r}) \phi_{0,\boldsymbol{q'}}(\boldsymbol{r}). \tag{C.6}$$

By applying the orthonormality of the Bloch functions, and definitions of the 3 dimensional delta function, one eventually obtains:

$$J = \left(\frac{a}{2\pi}\right)^3 \int_{\text{BZ}} d\boldsymbol{q} e^{i\boldsymbol{q}\cdot(\boldsymbol{R}_i - \boldsymbol{R}_j)} E_0(\boldsymbol{q}), \tag{C.7}$$

$$= \left(\frac{a}{2\pi}\right)^3 \int_{-\pi/a}^{\pi/a} \int_{-\pi/a}^{\pi/a} \int_{-\pi/a}^{\pi/a} dq_x dq_y dq_z e^{iq_x(X_i - X_j)} e^{iq_y(Y_i - Y_j)} e^{iq_z(Z_i - Z_j)} \left(E_0(q_x) + E_0(q_y) + E_0(q_z)\right), \tag{C.8}$$

$$= \frac{a}{2\pi} \left(\delta_{Y_i,Y_j}\delta_{Z_i,Z_j} \int_{-\pi/a}^{\pi/a} dq_x e^{iq_x(X_i - X_j)} E_0(q_x) + \delta_{Z_i,Z_j}\delta_{X_i,X_j} \int_{-\pi/a}^{\pi/a} dq_y e^{iq_y(Y_i - Y_j)} E_0(q_y) + \right.$$
$$\left. \delta_{X_i,X_j}\delta_{Y_i,Y_j} \int_{-\pi/a}^{\pi/a} dq_z e^{iq_z(Z_i - Z_j)} E_0(q_z) \right). \tag{C.9}$$

By the construction of the lattice potential, nearest neighbour pairs lie in the same principle direction, so we finally get an expression for the tunnelling potential (restricted to nearest neighbour interactions) in terms of a single 1D integral:

$$J = \frac{a}{2\pi} \int_{-\pi/a}^{\pi/a} dq e^{iq(X_i - X_j)} E_0(q). \tag{C.10}$$

This integral can be computed in the same way as the 1D Wannier functions.

Finally, the critical depth D_{crit} can be found using the above computations of J and U. One sets up the calculations of U and J as functions of the depth D, and then uses a Newton-Raphson approach to solve the equation $U(D) - 5.8zJ(D) = 0$ for positive values of D.

These methods are realised in Python and are available on GitHub [165].

BIBLIOGRAPHY

[1] Joseph Peter Scott, RM Potvliege, David Carty, and Matthew PA Jones. Trap induced broadening in a potential hydrogen lattice clock. *Metrologia*, 2023. doi:10.1088/1681-7575/ad1e37.

[2] J. P. Scott. Hydrogen-s-state-2-photon(1.0). https://doi.org/10.5281/zenodo.10034256, 2023.

[3] I. S. Gradshteĭn and I. M. Ryzhik. *Table of integrals, series, and products*. Academic Press, 8th edition, 2015.

[4] BIPM. *Le Système international d'unités / The International System of Units ('The SI Brochure')*. Bureau international des poids et mesures, ninth edition, 2019. URL: http://www.bipm.org/en/si/si_brochure/.

[5] D. R. Hartree. The wave mechanics of an atom with a non-coulomb central field. part i. theory and methods. *Mathematical Proceedings of the Cambridge Philosophical Society*, 24(1):89–110, 1928. doi:10.1017/S0305004100011919.

[6] *Springer handbook of atomic, molecular, and optical physics*. Springer, 2nd ed. edition, 2006.

[7] AE Kramida. A critical compilation of experimental data on spectral lines and energy levels of hydrogen, deuterium, and tritium. *Atomic Data and Nuclear Data Tables*, 96(6):586–644, 2010. doi:10.1016/j.adt.2010.05.001.

[8] M. Horbatsch and E. A. Hessels. Tabulation of the bound-state energies of atomic hydrogen. *Physical Review A*, 93:022513, 2016. doi:10.1103/PhysRevA.93.022513.

[9] Christopher J Foot. *Atomic physics*, volume 7. OUP Oxford, 2004.

[10] Paul Strange. *Relativistic Quantum Mechanics: With Applications in Condensed Matter and Atomic Physics*. Cambridge University Press, 1998.

[11] Peter J. Mohr, Barry N. Taylor, and David B. Newell. Codata recommended values of the fundamental physical constants: 2010. *Journal of Physical and Chemical Reference Data*, 41(4):043109, 2012. doi:10.1063/1.4724320.

[12] Peter J Mohr, David B Newell, and Barry N Taylor. Codata recommended values of the fundamental physical constants: 2014. *Journal of Physical and Chemical Reference Data*, 45(4):043102, 2016. doi:10.1063/1.4954402.

[13] Eite Tiesinga, Peter J. Mohr, David B. Newell, and Barry N. Taylor. Codata recommended values of the fundamental physical constants: 2018. *Reviews of Modern Physics*, 93:025010, 2021. doi:10.1103/RevModPhys.93.025010.

[14] Theodor W Hänsch, Arthur L Schawlow, and George W Series. The spectrum of atomic hydrogen. *Scientific American*, 240(3):94–111, 1979.

[15] Theodor W Hänsch. Nobel lecture: passion for precision. *Reviews of Modern Physics*, 78(4):1297, 2006. doi:10.1103/RevModPhys.78.1297.

[16] Savely G Karshenboim. Precision physics of simple atoms: Qed tests, nuclear structure and fundamental constants. *Physics reports*, 422(1-2):1–63, 2005. doi:10.1016/j.physrep.2005.08.008.

[17] Joerg Jaeckel and Sabyasachi Roy. Spectroscopy as a test of coulomb's law: a probe of the hidden sector. *Physical Review D*, 82(12):125020, 2010. doi:10.1103/PhysRevD.82.125020.

[18] Yevgeny V Stadnik. Probing long-range neutrino-mediated forces with atomic and nuclear spectroscopy. *Physical Review Letters*, 120(22):223202, 2018. doi:10.1103/PhysRevLett.120.223202.

[19] Mitrajyoti Ghosh, Yuval Grossman, and Walter Tangarife. Probing the two-neutrino exchange force using atomic parity violation. *Physical Review D*, 101(11):116006, 2020. doi:10.1103/PhysRevD.101.116006.

[20] Christian G. Parthey, Arthur Matveev, Janis Alnis, Birgitta Bernhardt, Axel Beyer, Ronald Holzwarth, Aliaksei Maistrou, Randolf Pohl, Katharina Predehl, Thomas Udem, Tobias Wilken, Nikolai Kolachevsky, Michel Abgrall, Daniele Rovera, Christophe Salomon, Philippe Laurent, and Theodor W. Hänsch. Improved measurement of the hydrogen 1s–2s transition frequency. *Physical Review Letters*, 107:203001, Nov 2011. doi:10.1103/PhysRevLett.107.203001.

[21] EW Hagley and FM Pipkin. Separated oscillatory field measurement of hydrogen 2 s 1/2-2 p 3/2 fine structure interval. *Physical Review Letters*, 72(8):1172, 1994. doi:10.1103/PhysRevLett.72.1172.

[22] M Weitz, A Huber, F Schmidt-Kaler, D Leibfried, W Vassen, C Zimmermann, K Pachucki, TW Hänsch, L Julien, and F Biraben. Precision measurement of the 1s ground-state lamb shift in atomic hydrogen and deuterium by frequency comparison. *Physical Review A*, 52(4):2664, 1995. doi:10.1103/PhysRevA.52.2664.

[23] B. de Beauvoir, F. Nez, L. Julien, B. Cagnac, F. Biraben, D. Touahri, L. Hilico, O. Acef, A. Clairon, and J. J. Zondy. Absolute frequency measurement of the 2s–8s/d transitions in hydrogen and deuterium: New determination of the rydberg constant. *Physics Review Letters*, 78:440–443, 1997. doi:10.1103/PhysRevLett.78.440.

[24] S Bourzeix, B De Beauvoir, F Nez, MD Plimmer, Ferdinando de Tomasi, L Julien, F Biraben, and DN Stacey. High resolution spectroscopy of the hydrogen atom: determination of the 1 s lamb shift. *Physical review letters*, 76(3):384, 1996. doi:10.1103/PhysRevLett.76.384.

[25] C. Schwob, L. Jozefowski, B. de Beauvoir, L. Hilico, F. Nez, L. Julien, F. Biraben, O. Acef, J.-J. Zondy, and A. Clairon. Optical frequency measurement of the 2s–12d transitions in hydrogen and deuterium: Rydberg constant and lamb shift determinations. *Physics Review Letters*, 82:4960–4963, 1999. doi:10.1103/PhysRevLett.82.4960.

[26] B. de Beauvoir, C. Schwob, O. Acef, L. Jozefowski, L. Hilico, F. Nez, L. Julien, A. Calairon, and F. Biraben. Metrology of the hydrogen and deuterium atoms: Determination of the rydberg constant and lamb shifts. *European Physical Journal D*, 12:1434–6079, 2000. doi:10.1007/s100530070043.

[27] Joel Christopher De Vries. *A precision millimeter-wave measurement of the Rydberg frequency*. Phd thesis, Massachusetts Institute of Technology, 2001.

[28] Arthur Matveev, Christian G. Parthey, Katharina Predehl, Janis Alnis, Axel Beyer, Ronald Holzwarth, Thomas Udem, Tobias Wilken, Nikolai Kolachevsky, Michel Abgrall, Daniele Rovera, Christophe Salomon, Philippe Laurent, Gesine Grosche, Osama Terra, Thomas Legero, Harald Schnatz, Stefan Weyers, Brett Altschul, and Theodor W. Hänsch. Precision measurement of the hydrogen 1s–2s frequency via a 920-km fiber link. *Physical Review Letters*, 110:230801, 2013. doi:10.1103/PhysRevLett.110.230801.

[29] A. Beyer, L. Maisenbacher, A. Matveev, R. Pohl, K. Khabarova, A. Grinin, T. Lamour, D. C. Yost, T. W. Hänsch, N. Kolachevsky, and T. Udem. The rydberg constant and proton size from atomic hydrogen. *Science*, 358(6359):79–85, 2017. doi:10.1126/science.aah6677.

[30] Hélène Fleurbaey, Sandrine Galtier, Simon Thomas, Marie Bonnaud, Lucile Julien, Fran çois Biraben, Fran çois Nez, Michel Abgrall, and Jocelyne Guéna. New measurement of the 1s–3s transition frequency of hydrogen: Contribution to the proton charge radius puzzle. *Physical Review Letters*, 120:183001, 2018. doi:10.1103/PhysRevLett.120.183001.

[31] N. Bezginov, T. Valdez, M. Horbatsch, A. Marsman, A. C. Vutha, and E. A. Hessels. A measurement of the atomic hydrogen lamb shift and the proton charge radius. *Science*, 365(6457):1007–1012, 2019. doi:10.1126/science.aau7807.

[32] A. Grinin, A. Matveev, D. C. Yost, L. Maisenbacher, V. Wirthl, R. Pohl, T. W. Hänsch, and T. Udem. Two-photon frequency comb spectroscopy of atomic hydrogen. *Science*, 370(6520):1061–1066, 2020. doi:10.1126/science.abc7776.

[33] A. D. Brandt, S. F. Cooper, C. Rasor, Z. Burkley, A. Matveev, and D. C. Yost. Measurement of the $2s_{1/2}$–$8d_{5/2}$ transition in hydrogen. *Physical Review Letters*, 128:023001, 2022. doi:10.1103/PhysRevLett.128.023001.

[34] Simon Scheidegger and Frédéric Merkt. Precision-spectroscopic determination of the binding energy of a two-body quantum system: The hydrogen atom and the proton-size

puzzle. *Physical Review Letters*, 132(11):113001, 2024. doi:10.1103/PhysRevLett.132.113001.

[35] Randolf Pohl, Ronald Gilman, Gerald A Miller, and Krzysztof Pachucki. Muonic hydrogen and the proton radius puzzle. *Annual Review of Nuclear and Particle Science*, 63:175–204, 2013. doi:10.1146/annurev-nucl-102212-170627.

[36] Weizhi Xiong and Chao Peng. Proton electric charge radius from lepton scattering. *Universe*, 9(4):182, 2023. doi:10.3390/universe9040182.

[37] Haiyan Gao and Marc Vanderhaeghen. The proton charge radius. *Reviews of Modern Physics*, 94(1):015002, 2022. doi:10.1103/RevModPhys.94.015002.

[38] Matthew PA Jones, Robert M Potvliege, and Michael Spannowsky. Probing new physics using rydberg states of atomic hydrogen. *Physical Review Research*, 2(1):013244, 2020. doi:10.1103/PhysRevResearch.2.013244.

[39] Cédric Delaunay, Jean-Philippe Karr, Teppei Kitahara, Jeroen CJ Koelemeij, Yotam Soreq, and Jure Zupan. Self-consistent extraction of spectroscopic bounds on light new physics. *Physical Review Letters*, 130(12):121801, 2023. doi:10.1103/PhysRevLett.130.121801.

[40] Robert M Potvliege, Adair Nicolson, Matthew PA Jones, and Michael Spannowsky. Deuterium spectroscopy for enhanced bounds on physics beyond the standard model. *Physical Review A*, 108(5):052825, 2023. doi:10.1103/PhysRevA.108.052825.

[41] Hannah Banks and Matthew McCullough. Charting the fifth force landscape. *Physical Review D*, 103(7):075018, 2021. doi:10.1103/PhysRevD.103.075018.

[42] Savely G Karshenboim. Precision physics of simple atoms and constraints on a light boson with ultraweak coupling. *Physical Review Letters*, 104(22):220406, 2010. doi:10.1103/PhysRevLett.104.220406.

[43] Philippe Brax and Clare Burrage. Atomic precision tests and light scalar couplings. *Physical Review D*, 83(3):035020, 2011. doi:10.1103/PhysRevD.83.035020.

[44] MS Safronova, D Budker, D DeMille, Derek F Jackson Kimball, A Derevianko, and Charles W Clark. Search for new physics with atoms and molecules. *Reviews of Modern Physics*, 90(2):025008, 2018. doi:10.1103/RevModPhys.90.025008.

[45] Andrei Derevianko and Hidetoshi Katori. Colloquium: Physics of optical lattice clocks. *Reviews of Modern Physics*, 83(2):331, 2011. doi:10.1103/RevModPhys.83.331.

[46] Masao Takamoto, Feng-Lei Hong, Ryoichi Higashi, and Hidetoshi Katori. An optical lattice clock. *Nature*, 435(7040):321–324, 2005. doi:10.1038/nature03541.

[47] Rodolphe Le Targat, Xavier Baillard, Mathilde Fouché, Anders Brusch, Olivier Tcherbakoff, Giovanni D Rovera, and Pierre Lemonde. Accurate optical lattice clock with ^{87}sr atoms. *Physical Review Letters*, 97(13):130801, 2006. doi:10.1103/PhysRevLett.97.130801.

[48] Andrew D Ludlow, Martin M Boyd, Tanya Zelevinsky, Seth M Foreman, Sebastian Blatt, Mark Notcutt, Tetsuya Ido, and Jun Ye. *Physical Review Letters*, 96(3):033003, 2006. doi:10.1103/PhysRevLett.96.033003.

[49] Zeb W Barber, Chad W Hoyt, Christopher W Oates, Leo Hollberg, Aleksei V Taichenachev, and Valera I Yudin. Systematic study of the ^{87}sr clock transition in an optical lattice. *Physical Review Letters*, 96(8):083002, 2006. doi:10.1103/PhysRevLett.96.083002.

[50] Tobias Bothwell, Dhruv Kedar, Eric Oelker, John M Robinson, Sarah L Bromley, Weston L Tew, Jun Ye, and Colin J Kennedy. Jila sri optical lattice clock with uncertainty of 2.0×10^{-18}. *Metrologia*, 56(6):065004, 2019. doi:10.1088/1681-7575/ab4089.

[51] Paolo Crivelli and Nikolai Kolachevsky. Optical trapping of antihydrogen towards an atomic anti-clock. *Hyperfine Interactions*, 241(1):1–11, 2020. doi:10.1007/s10751-018-1549-4.

[52] Michael Ahmadi, Bruno Ximenez Rodrigues Alves, CJ Baker, W Bertsche, E Butler, A Capra, C Carruth, CL Cesar, M Charlton, S Cohen, et al. Observation of the 1s–2s transition in trapped antihydrogen. *Nature*, 541(7638):506–510, 2017. doi:10.1038/nature21040.

[53] M Ahmadi, BXR Alves, CJ Baker, W Bertsche, A Capra, C Carruth, CL Cesar, M Charlton, S Cohen, R Collister, et al. Characterization of the 1s–2s transition in antihydrogen. *Nature*, 557(7703):71–75, 2018. doi:10.1038/s41586-018-0017-2.

[54] G. M. Shore. Strong equivalence, lorentz and cpt violation, anti-hydrogen spectroscopy and gamma-ray burst polarimetry. *Nuclear Physics B*, 717:86–118, 2005. doi:10.1016/j.nuclphysb.2005.03.040.

[55] V Alan Kostelecký and Arnaldo J Vargas. Lorentz and cpt tests with hydrogen, antihydrogen, and related systems. *Physical Review D*, 92(5):056002, 2015. doi:10.1103/PhysRevD.92.056002.

[56] Ian C. Lane. Production of ultracold hydrogen and deuterium via doppler-cooled feshbach molecules. *Physical Review A*, 92:022511, Aug 2015. doi:10.1103/PhysRevA.92.022511.

[57] Dale G Fried, Thomas C Killian, Lorenz Willmann, David Landhuis, Stephen C Moss, Daniel Kleppner, and Thomas J Greytak. Bose-einstein condensation of atomic hydrogen. *Physical Review Letters*, 81(18):3811, 1998. doi:10.1103/PhysRevLett.81.3811.

[58] Rodney Loudon. *The quantum theory of light*. Oxford University Press, third edition, 2010.

[59] Claude Cohen-Tannoudji, Jacques Dupont-Roc, and Gilbert Grynberg. *Atom-photon interactions: Basic processes and applications*. Wiley-vch, 2004.

[60] Robin A Swainson and Gordon WF Drake. A unified treatment of the non-relativistic and relativistic hydrogen atom ii: The green functions. *Journal of Physics A: Mathematical and General*, 24(1):95, 1991. doi:10.1088/0305-4470/24/1/020.

[61] Valérie Véniard and Bernard Piraux. Continuum-continuum dipole transitions in femtosecond-laser-pulse excitation of atomic hydrogen. *Physical Review A*, 41(7):4019, 1990. doi:10.1103/PhysRevA.41.4019.

[62] James Lewis Friar and GL Payne. Higher-order nuclear-size corrections in atomic hydrogen. *Physical Review A*, 56(6):5173, 1997. doi:10.1103/PhysRevA.56.5173.

[63] Krzysztof Pachucki, Vojtěch Patkóš, and Vladimir A Yerokhin. Three-photon-exchange nuclear structure correction in hydrogenic systems. *Physical Review A*, 97(6):062511, 2018. doi:10.1103/PhysRevA.97.062511.

[64] W. A. Barker and F. N. Glover. Reduction of relativistic two-particle wave equations to approximate forms. iii. *Physical Review*, 99:317–324, 1955. doi:10.1103/PhysRev.99.317.

[65] K Pachucki and SG Karshenboim. Nuclear-spin-dependent recoil correction to the lamb shift. *Journal of Physics B: Atomic, Molecular and Optical Physics*, 28(7):L221, 1995. doi:10.1088/0953-4075/28/7/004.

[66] Glen W Erickson and Donald R Yennie. Radiative level shifts, i. formulation and lowest order lamb shift. *Annals of Physics*, 35(2):271–313, 1965. doi:10.1016/0003-4916(65)90081-3.

[67] Gordon WF Drake and Robin A Swainson. Bethe logarithms for hydrogen up to n= 20, and approximations for two-electron atoms. *Physical Review A*, 41(3):1243, 1990. doi:10.1103/PhysRevA.41.1243.

[68] Glen W. Erickson. Energy levels of one-electron atoms. *Journal of Physical and Chemical Reference Data*, 6(3):831–870, 1977. doi:10.1063/1.555557.

[69] Richard H Parker, Chenghui Yu, Weicheng Zhong, Brian Estey, and Holger Müller. Measurement of the fine-structure constant as a test of the standard model. *Science*, 360(6385):191–195, 2018. doi:10.1126/science.aap7706.

[70] T Udem. private communication.

[71] Constantia Alexandrou, Kyriakos Hadjiyiannakou, Giannis Koutsou, Konstantin Ottnad, and Marcus Petschlies. Model-independent determination of the nucleon charge radius from lattice qcd. *Physical Review D*, 101(11):114504, 2020. doi:10.1103/PhysRevD.101.114504.

[72] Aharon Davidson. $b - l$ as the fourth color within an $\mathrm{SU}(2)_L \times \mathrm{U}(1)_R \times \mathrm{U}(1)$ model. *Physical Review D*, 20:776–783, 1979. doi:10.1103/PhysRevD.20.776.

[73] RE Marshak and Rabindra N Mohapatra. Quark-lepton symmetry and b- l as the u (1) generator of the electroweak symmetry group. *Physics Letters B*, 91(2):222–224, 1980. doi:10.1016/0370-2693(80)90436-0.

[74] CJ Baker, W Bertsche, A Capra, C Carruth, CL Cesar, M Charlton, A Christensen, R Collister, A Cridland Mathad, Stefan Eriksson, et al. Laser cooling of antihydrogen atoms. *Nature*, 592(7852):35–42, 2021. doi:10.1038/s41586-021-03289-6.

[75] Donal O'Connell, Michael J. Ramsey-Musolf, and Mark B. Wise. Minimal extension of the standard model scalar sector. *Physical Review D*, 75:037701, 2007. doi:10.1103/PhysRevD.75.037701.

[76] Bob Holdom. Two u (1)'s and ϵ charge shifts. *Physics Letters B*, 166(2):196–198, 1986. doi:10.1016/0370-2693(86)91377-8.

[77] Ulrich D Jentschura and István Nándori. Atomic physics constraints on the x boson. *Physical Review A*, 97(4):042502, 2018. doi:10.1103/PhysRevA.97.042502.

[78] Nicolás Viaux, Márcio Catelan, Peter B Stetson, GG Raffelt, Javier Redondo, Aldo AR Valcarce, and Achim Weiss. Neutrino and axion bounds from the globular cluster m5 (ngc 5904). *Physical Review Letters*, 111(23):231301, 2013. doi:10.1103/PhysRevLett.111.231301.

[79] Justin Khoury and Amanda Weltman. Chameleon fields: Awaiting surprises for tests of gravity in space. *Physical Review Letters*, 93(17):171104, 2004. doi:10.1103/PhysRevLett.93.171104.

[80] Justin Khoury. Chameleon field theories. *Classical and Quantum Gravity*, 30(21):214004, 2013. doi:10.1088/0264-9381/30/21/214004.

[81] Clare Burrage and Jeremy Sakstein. Tests of chameleon gravity. *Living reviews in relativity*, 21:1–58, 2018. doi:10.1007/s41114-018-0011.

[82] L Essen, RW Donaldson, MJ Bangham, and EG Hope. Frequency of the hydrogen maser. *Nature*, 229(5280):110–111, 1971. doi:10.1038/229110a0.

[83] L Essen, RW Donaldson, EG Hope, and MJ Bangham. Hydrogen maser work at the national physical laboratory. *Metrologia*, 9(3):128, 1973.

[84] P Petit, M Desaintfuscien, and C Audoin. Temperature dependence of the hydrogen maser wall shift in the temperature range 295-395 k. *Metrologia*, 16(1):7, 1980. doi:10.1088/0026-1394/16/1/003.

[85] Nikolai Kolachevsky, Arthur Matveev, Janis Alnis, Christian G Parthey, Savely G Karshenboim, and TW Hänsch. Measurement of the 2 s hyperfine interval in atomic hydrogen. *Physical Review Letters*, 102(21):213002, 2009. doi:10.1103/PhysRevLett.102.213002.

[86] RG Bullis, C Rasor, WL Tavis, SA Johnson, MR Weiss, and DC Yost. Ramsey spectroscopy of the $2s_{1/2}$ hyperfine interval in atomic hydrogen. *Physical Review Letters*, 130(20):203001, 2023. doi:10.1103/PhysRevLett.130.203001.

[87] DJ Berkeland, EA Hinds, and MG Boshier. Precise optical measurement of lamb shifts in atomic hydrogen. *Physical Review Letters*, 75(13):2470, 1995. doi:10.1103/PhysRevLett.75.247.

[88] Olivier Arnoult, François Nez, Lucile Julien, and François Biraben. Optical frequency measurement of the 1s–3s two-photon transition in hydrogen. *The European Physical Journal D*, 60(2):243–256, 2010. doi:10.1140/epjd/e2010-00249-6.

[89] Christian G Parthey, Arthur Matveev, Janis Alnis, Randolf Pohl, Thomas Udem, Ulrich D Jentschura, Nikolai Kolachevsky, and Theodor W Hänsch. Precision measurement of the hydrogen-deuterium 1 s- 2 s isotope shift. *Physical review letters*, 104(23):233001, 2010. doi:10.1103/PhysRevLett.104.233001.

[90] Dylan C Yost, A Matveev, Alexey Grinin, Elisabeth Peters, Lothar Maisenbacher, Axel Beyer, Randolf Pohl, N Kolachevsky, K Khabarova, TW Hänsch, et al. Spectroscopy of the hydrogen 1 s- 3 s transition with chirped laser pulses. *Physical Review A*, 93(4):042509, 2016. doi:10.1103/PhysRevA.93.042509.

[91] Ulrich D Jentschura and Dylan C Yost. Precision rydberg state spectroscopy with slow electrons and the proton-radius puzzle. *Physical Review A*, 108(6):062822, 2023. doi:10.1103/PhysRevA.108.062822.

[92] K Yu Khabarova and Nikolai N Kolachevsky. Proton charge radius. *Physics-Uspekhi*, 64(10):1038, 2021. doi:10.3367/UFNe.2021.06.038986.

[93] Rudolf Grimm, Matthias Weidemüller, and Yurii B Ovchinnikov. Optical dipole traps for neutral atoms. In *Advances in atomic, molecular, and optical physics*, volume 42, pages 95–170. Elsevier, 2000. doi:10.1016/S1049-250X(08)60186-X.

[94] M. Haas, U. D. Jentschura, and C. H. Keitel. Comparison of classical and second quantized description of the dynamic stark shift. *American Journal of Physics*, 74(1):77–81, 2006. doi:10.1119/1.2140742.

[95] Fam Le Kien, Philipp Schneeweiss, and Arno Rauschenbeutel. Dynamical polarizability of atoms in arbitrary light fields: general theory and application to cesium. *The European Physical Journal D*, 67(5):1–16, 2013. doi:10.1140/epjd/e2013-30729-x.

[96] Mevan Gunawardena, DS Elliott, MS Safronova, and U Safronova. Determination of the static polarizability of the $8s^2s_{1/2}$ state of atomic cesium. *Physical Review A*, 75(2):022507, 2007.

[97] Tudor A Marian. Bound-bound two-photon transition matrix elements for the hydrogen atom in the dipole approximation. *Physical Review A*, 39(8):3816, 1989. doi:10.1103/PhysRevA.39.3816.

[98] Alfred Maquet, Valérie Véniard, and Tudor A Marian. The coulomb green's function and multiphoton calculations. *Journal of Physics B: Atomic, Molecular and Optical Physics*, 31(17):3743, 1998. doi:10.1088/0953-4075/31/17/004.

[99] S Klarsfeld. Interaction of metastable hydrogenlike atoms with electromagnetic radiation. *Physical Review A*, 6(1):506, 1972. doi:10.1103/PhysRevA.6.506.

[100] Y Heno, A Maquet, and R Schwarcz. Raman-like scattering processes in metastable hydrogenic atoms. *Journal of Applied Physics*, 51(1):11–14, 1980. doi:10.1063/1.327404.

[101] Chandra M Adhikari, Jonathan C Canales, Thusitha PW Arthanayaka, and Ulrich D Jentschura. Magic wavelengths for 1s–ns and 2s–ns transitions in hydrogenlike systems. *Atoms*, 10(1):1, 2022. doi:10.3390/atoms10010001.

[102] Wolfgang Zernik. Interaction of optical and infrared radiation with metastable hydrogen atoms. *Physical Review*, 133(1A):A117, 1964. doi:10.1103/PhysRev.133.A11.

[103] Y Gontier and M Trahin. Multiphoton processes in a hydrogen atom. *Physical Review A*, 4(5):1896, 1971. doi:10.1103/PhysRevA.4.1896.

[104] RM Potvliege and R Shakeshaft. High-order above-threshold ionization of hydrogen in perturbation theory. *Zeitschrift fuer Physik, D*, 11(1):93–94, 1989. doi:10.1103/PhysRevA.39.1545.

[105] RM Potvliege. Strflo: A program for time-independent calculations of multiphoton processes in one-electron atomic systems i. quasienergy spectra and angular distributions. *Computer physics communications*, 114(1-3):42–93, 1998. doi:10.1016/S0010-4655(98)00073-3.

[106] Harry A Mavromatis. The dalgarno–lewis summation technique: Some comments and examples. *American Journal of Physics*, 59(8):738–744, 1991. doi:10.1119/1.16753.

[107] TK Nandi, PK Bera, MM Panja, and B Talukdar. The dalgarno-lewis method as a perturbation theory. *Journal of Physics A: Mathematical and General*, 29(5):1101, 1996. doi:10.1088/0305-4470/29/5/022.

[108] Levere C Hostler. Coulomb green's function in f-dimensional space. *Journal of Mathematical Physics*, 11(10):2966–2970, 1970. doi:10.1063/1.1665081.

[109] Gabor Szegö. *Orthogonal Polynomials*. American Mathematical Society, 1st ed. edition, 1939.

[110] Sören Dörscher, Roman Schwarz, Ali Al-Masoudi, Stephan Falke, Uwe Sterr, and Christian Lisdat. Lattice-induced photon scattering in an optical lattice clock. *Physical Review A*, 97(6):063419, 2018. doi:10.1103/PhysRevA.97.063419.

[111] Chandra M Adhikari, A Kawasaki, and Ulrich D Jentschura. Magic wavelength for the hydrogen 1s–2s transition: Contribution of the continuum and the reduced-mass correction. *Physical Review A*, 94(3):032510, 2016. doi:10.1103/PhysRevA.94.032510.

[112] Ifan Hughes and Thomas P. A. Hase. *Measurements and their uncertainties a practical guide to modern error analysis*. OUP, 2010.

[113] J. Alnis, A. Matveev, N. Kolachevsky, Th. Udem, and T. W. Hänsch. Sub-hz line width diode lasers by stabilization to vibrationally and thermally compensated ule fabry-perot cavities. *Physical Review A*, 77:053809, May 2008. doi:10.1103/PhysRevA.77.053809.

[114] VJ Martínez-Lahuerta, S Eilers, TE Mehlstäubler, PO Schmidt, and K Hammerer. Ab initio quantum theory of mass defect and time dilation in trapped-ion optical clocks. *Physical Review A*, 106(3):032803, 2022. doi:10.1103/PhysRevA.106.032803.

[115] JP Santos, F Parente, and P Indelicato. Application of b-splines finite basis sets to relativistic two-photon decay rates of level in hydrogenic ions. *The European Physical Journal D-Atomic, Molecular, Optical and Plasma Physics*, 3(1):43–52, 1998. doi:10.1007/s100530050147.

[116] Helen K Holt and IA Sellin. Time-dependent theory of stark quenching of states in hydrogen and helium. *Physical Review A*, 6(1):508, 1972. doi:10.1103/PhysRevA.6.508.

[117] Wolfgang Zernik. Optical quenching of metastable hydrogen. *Physical Review*, 132(1):320, 1963. doi:10.1103/PhysRev.132.320.

[118] Wolfgang Zernik. Two-photon ionization of atomic hydrogen. *Physical Review*, 135(1A):A51, 1964. doi:10.1103/PhysRev.135.A51.

[119] LP Rapoport, BA Zon, and LP Manakov. Two-photon ionization of the hydrogen atom. *Soviet Physics JETP*, 29:220, 1969.

[120] SV Khristenko and SI Vetchinkin. Multiphoton ionization of a hydrogen atom. *Optics and Spectroscopy(USSR)(Engl. Transl.);(United States)*, 40(3), 1976.

[121] E Karule and B Moine. The general expression for the transition amplitude of two-photon ionization of atomic hydrogen. *Journal of Physics B: Atomic, Molecular and Optical Physics*, 36(10):1963, 2003.

[122] G Gabrielse, B Glowacz, D Grzonka, CD Hamley, EA Hessels, N Jones, G Khatri, SA Lee, C Meisenhelder, T Morrison, et al. Lyman-α source for laser cooling antihydrogen. *Optics Letters*, 43(12):2905–2908, 2018. doi:10.1364/OL.43.002905.

[123] WF McGrew, X Zhang, RJ Fasano, SA Schäffer, K Beloy, D Nicolodi, RC Brown, N Hinkley, G Milani, M Schioppo, et al. Atomic clock performance enabling geodesy below the centimetre level. *Nature*, 564(7734):87–90, 2018. doi:10.1038/s41586-018-0738-2.

[124] Samuel M Brewer, J-S Chen, Aaron M Hankin, Ethan R Clements, Chin-wen Chou, David J Wineland, David B Hume, and David R Leibrandt. Al+ 27 quantum-logic clock with a systematic uncertainty below 10- 18. *Physical Review Letters*, 123(3):033201, 2019. doi:10.1103/PhysRevLett.123.033201.

[125] H. Saßmannshausen, F. Merkt, and J. Deiglmayr. High-resolution spectroscopy of rydberg states in an ultracold cesium gas. *Physical Review A*, 87:032519, Mar 2013. doi:10.1103/PhysRevA.87.032519.

[126] E. Vliegen, S. D. Hogan, H. Schmutz, and F. Merkt. Stark deceleration and trapping of hydrogen rydberg atoms. *Physical Review A*, 76:023405, Aug 2007. doi:10.1103/PhysRevA.76.023405.

[127] Ch Seiler, Josef A Agner, Pierre Pillet, and Frédéric Merkt. Radiative and collisional processes in translationally cold samples of hydrogen rydberg atoms studied in an electrostatic trap. *Journal of Physics B: Atomic, Molecular and Optical Physics*, 49(9):094006, 2016. doi:10.1088/0953-4075/49/9/094006.

[128] Harold J Metcalf and Peter Van der Straten. *Laser cooling and trapping*. Springer Science & Business Media, 1999.

[129] J. Walz et al. Cold antihydrogen atoms. *Applied Physics B*, 77:713–717, 2003. doi:10.1007/s00340-003-1344-y.

[130] J Mario Michan, Gene Polovy, Kirk W Madison, Makoto C Fujiwara, and Takamasa Momose. Narrowband solid state vuv coherent source for laser cooling of antihydrogen. *Hyperfine Interactions*, 235:29–36, 2015. doi:10.1007/s10751-015-1186-0.

[131] I. D. Setija, H. G. C. Werij, O. J. Luiten, M. W. Reynolds, T. W. Hijmans, and J. T. M. Walraven. Optical cooling of atomic hydrogen in a magnetic trap. *Physical Review Letters*, 70:2257–2260, 1993. doi:10.1103/PhysRevLett.70.2257.

[132] A. Aspect, E. Arimondo, R. Kaiser, N. Vansteenkiste, and C. Cohen-Tannoudji. Laser cooling below the one-photon recoil energy by velocity-selective coherent population trapping. *Physical Review Letters*, 61:826–829, 1988. doi:10.1103/PhysRevLett.61.826.

[133] Wim Vassen, Claude Cohen-Tannoudji, Michele Leduc, Denis Boiron, Christoph I Westbrook, Andrew Truscott, Ken Baldwin, Gerhard Birkl, Pablo Cancio, and Marek Trippenbach. Cold and trapped metastable noble gases. *Reviews of Modern Physics*, 84(1):175, 2012. doi:10.1103/RevModPhys.84.175.

[134] S. F. Cooper et al. Cavity-enhanced deep ultraviolet laser for two-photon cooling of atomic hydrogen. *Optical Letters*, 43:1375–1378, 2018. doi:10.1364/OL.43.001375.

[135] SF Vázquez-Carson, Q Sun, J Dai, D Mitra, and T Zelevinsky. Direct laser cooling of calcium monohydride molecules. *New Journal of Physics*, 24(8):083006, 2022. doi:10.1088/1367-2630/ac806c.

[136] Jinyu Dai, Qi Sun, Benjamin C Riley, Debayan Mitra, and Tanya Zelevinsky. Laser cooling of a fermionic molecule. *arXiv preprint arXiv:2401.12145*, 2024. doi:10.48550/arXiv.2401.12145.

[137] Mike H Anderson, Jason R Ensher, Michael R Matthews, Carl E Wieman, and Eric A Cornell. Observation of bose-einstein condensation in a dilute atomic vapor. *Science*, 269(5221):198–201, 1995. doi:10.1126/science.269.5221.198.

[138] Cl C Bradley, CA Sackett, JJ Tollett, and Randall G Hulet. Evidence of bose-einstein condensation in an atomic gas with attractive interactions. *Physical Review Letters*, 75(9):1687, 1995. doi:10.1103/PhysRevLett.75.1687.

[139] Kendall B Davis, M-O Mewes, Michael R Andrews, Nicolaas J van Druten, Dallin S Durfee, DM Kurn, and Wolfgang Ketterle. Bose-einstein condensation in a gas of sodium atoms. *Physical Review Letters*, 75(22):3969, 1995. doi:https://doi.org/10.1103/PhysRevLett.75.3969.

[140] Dale G Fried. *Bose-Einstein condensation of atomic hydrogen.* Phd thesis, Massachusetts Institute of Technology, 1999.

[141] A Sen, S Chakraborty, and AS Ghosh. Scattering of hydrogen atoms at low temperature. *Europhysics Letters*, 76(4):582, 2006. doi:10.1209/epl/i2006-10325-0.

[142] BR Joudeh. Scattering properties of ground-state spin-polarized atomic hydrogen. *Physica B: Condensed Matter*, 421:41–45, 2013. doi:10.1016/j.physb.2013.04.014.

[143] Carl J Williams and Paul S Julienne. Mass effects in the theoretical determination of nuclear-spin relaxation rates for atomic hydrogen and deuterium. *Physical Review A*, 47(2):1524, 1993. doi:10.1103/PhysRevA.47.1524.

[144] D Blume, BD Esry, Chris H Greene, NN Klausen, and GJ Hanna. Formation of atomic tritium clusters and bose-einstein condensates. *Physical Review Letters*, 89(16):163402, 2002. doi:10.1103/PhysRevLett.89.163402.

[145] DG Friend and RD Etters. A dilute hard-sphere bose-gas model calculation of low-density atomic hydrogen gas properties. *Journal of Low Temperature Physics*, 39:409–415, 1980. doi:10.1007/BF00115630.

[146] MD Barrett, JA Sauer, and MS Chapman. All-optical formation of an atomic bose-einstein condensate. *Physical Review Letters*, 87(1):010404, 2001. doi:10.1103/PhysRevLett.87.010404.

[147] Michael C Garrett, Adrian Ratnapala, Eikbert D Van Ooijen, Christopher J Vale, Kristian Weegink, Sebastian K Schnelle, Otto Vainio, Norman R Heckenberg, Halina Rubinsztein-Dunlop, and Matthew J Davis. Growth dynamics of a bose-einstein condensate in a dimple trap without cooling. *Physical Review A*, 83(1):013630, 2011. doi:10.1103/PhysRevA.83.013630.

[148] David Jacob, Emmanuel Mimoun, Luigi De Sarlo, Martin Weitz, Jean Dalibard, and Fabrice Gerbier. Production of sodium bose–einstein condensates in an optical dimple trap. *New Journal of Physics*, 13(6):065022, 2011. doi:10.1088/1367-2630/13/6/065022.

[149] Otto Vainio, Janne Ahokas, Jarno Järvinen, Lauri Lehtonen, Steffen Novotny, Sergei Sheludiakov, K-A Suominen, Sergey Vasiliev, Denis Zvezdov, Vladimir V Khmelenko, et al. Bose-einstein condensation of magnons in atomic hydrogen gas. *Physical Review Letters*, 114(12):125304, 2015. doi:10.1103/PhysRevLett.114.125304.

[150] Janne Ahokas, Aleksei Semakin, Jarno Järvinen, Otto Hanski, A Laptiyenko, V Dvornichenko, Kauko Salonen, Zakary Burkley, Paolo Crivelli, Artem Golovizin, et al. A large octupole magnetic trap for research with atomic hydrogen. *Review of Scientific Instruments*, 93(2), 2022. doi:10.1063/5.0070037.

[151] Immanuel Bloch and Markus Greiner. The superfluid-to-mott insulator transition and the birth of experimental quantum simulation. *Nature Reviews Physics*, 4(12):739–740, 2022. doi:10.1038/s42254-022-00520-9.

[152] Markus Greiner, Olaf Mandel, Tilman Esslinger, Theodor W Hänsch, and Immanuel Bloch. Quantum phase transition from a superfluid to a mott insulator in a gas of ultracold atoms. *Nature*, 415(6867):39–44, 2002. doi:10.1038/415039a.

[153] Nicola Marzari, Arash A Mostofi, Jonathan R Yates, Ivo Souza, and David Vanderbilt. Maximally localized wannier functions: Theory and applications. *Reviews of Modern Physics*, 84(4):1419, 2012. doi:10.1103/RevModPhys.84.1419.

[154] Dieter Jaksch, Christoph Bruder, Juan Ignacio Cirac, Crispin W Gardiner, and Peter Zoller. Cold bosonic atoms in optical lattices. *Physical Review Letters*, 81(15):3108, 1998. doi:10.1103/PhysRevLett.81.3108.

[155] B DeMarco, Courtney Lannert, S Vishveshwara, and T-C Wei. Structure and stability of mott-insulator shells of bosons trapped in an optical lattice. *Physical Review A*, 71(6):063601, 2005. doi:10.1103/PhysRevA.71.063601.

[156] Kaushik Mitra, CJ Williams, and CAR Sa De Melo. Superfluid and mott-insulating shells of bosons in harmonically confined optical lattices. *Physical Review A*, 77(3):033607, 2008. doi:10.1103/PhysRevA.77.033607.

[157] Wilhelm Zwerger. Mott–hubbard transition of cold atoms in optical lattices. *Journal of Optics B: quantum and semiclassical optics*, 5(2):S9, 2003. doi:10.1088/1464-4266/5/2/352.

[158] Gretchen K Campbell, Jongchul Mun, Micah Boyd, Patrick Medley, Aaron E Leanhardt, Luis G Marcassa, David E Pritchard, and Wolfgang Ketterle. Imaging the mott insulator shells by using atomic clock shifts. *Science*, 313(5787):649–652, 2006. doi:10.1126/science.1130365.

[159] Waseem S Bakr, Amy Peng, M Eric Tai, Ruichao Ma, Jonathan Simon, Jonathon I Gillen, Simon Foelling, Lode Pollet, and Markus Greiner. Probing the superfluid–to–mott insulator transition at the single-atom level. *Science*, 329(5991):547–550, 2010. doi:10.1126/science.119236.

[160] Tatjana Gericke, Fabrice Gerbier, Artur Widera, Simon Fölling, Olaf Mandel, and Immanuel Bloch. Adiabatic loading of a bose–einstein condensate in a 3d optical lattice. *Journal of Modern Optics*, 54(5):735–743, 2007. doi:10.1080/09500340600777730.

[161] Dariusz Kajtoch, Emilia Witkowska, and Alice Sinatra. Adiabaticity when raising a uniform three-dimensional optical lattice in a bimodal bose-einstein condensate. *Physical Review A*, 98(2):023621, 2018. doi:10.1103/PhysRevA.98.023621.

[162] Charles S Adams and Ifan G Hughes. *Optics f2f: from Fourier to Fresnel*. Oxford University Press, 2018.

[163] Akio Kawasaki. Magic wavelength for the hydrogen 1s–2s transition. *Physical Review A*, 92:042507, Oct 2015. doi:10.1103/PhysRevA.92.042507.

[164] EK Anderson, CJ Baker, W Bertsche, NM Bhatt, G Bonomi, A Capra, I Carli, CL Cesar, Michael Charlton, A Christensen, et al. Observation of the effect of gravity on the motion of antimatter. *Nature*, 621(7980):716–722, 2023. doi:10.1038/s41586-023-06527-1.

[165] Joseph P. Scott. Josephpscott/wannier_functions. https://github.com/JosephPScott/Wannier_functions. Accessed: 2024-04-10.

Colophon

This thesis is based on a template developed by Matthew Townson and Andrew Reeves. It was typeset with LaTeX 2_ε. It was created using the *memoir* package, maintained by Lars Madsen, with the *madsen* chapter style. The font used is Latin Modern, derived from fonts designed by Donald E. Kunith.